Exploring single-cell metabolism and its control on cell growth signals using fluorescent biosensors

by

NONT KOSAISAWE
DISSERTATION

Submitted in partial satisfaction of the requirements for the degree of

DOCTOR OF PHILOSOPHY

in

Biochemistry, molecular, cellular, and developmental biology

in the

OFFICE OF GRADUATE STUDIES

of the

UNIVERSITY OF CALIFORNIA

DAVIS

Approved:

_____
Mark O. Huising, Chair

_____
Ted Powers

_____
Oliver Fiehn

Committee in charge

2021

Table of Contents

Abstract

In current cellular biology, we often assume that cells operate at a near steady state. This assumption implies that each individual cell performs the same processes at any particular moment. However, this assumption proves to be difficult to reconcile with cellular processes that are dynamic and asynchronous, such as the cell cycle, in which each cell has its own clock, or ey signaling processes such as the MAPK and AKT pathways, which are heterogeneous and dynamic from cell to cell. These heterogeneities play an essential role in cell fate decisions, including proliferation and differentiation. Cell signaling information also 'spreads' to other pathways and thus creates complex changes in cellular states, including in metabolic flux and gene expression. The connection between cell signaling and cell metabolism raises the question of whether cell metabolism is heterogeneous too. Furthermore, metabolic states could influence how cells respond to growth signaling cues.

In the first part of this dissertation, I explore the question of whether cellular metabolism is heterogeneous in cell populations. I utilize a fluorescence-based FRET biosensor to probe AMPK activity when cellular oxidative phosphorylation (OXPHOS) is inhibited. I show that, in fact, at a single-cell level, cells do not utilize OXPHOS equally, and cellular adaptation after OXPHOS inhibition never reaches a steady state.

In the second part, I expand the idea of single-cell metabolism and ask how cell metabolism regulates growth signals at the single-cell level. I developed transposase-based transfection systems that would allow expression of up to three fluorescence biosensors in one transfection to achieve this goal. I also developed an unsupervised clustering technique for multi-dimensional time-series data to analyze more than 300,000 single cell traces. I showed that the signaling activity under metabolic conditions is heterogeneous even in the same type of metabolic stress. However, the signaling landscape is not infinite since there are only about 30 modes of

responses. This study characterizes the complex interaction between cell metabolism and cellular growth signals.

Acknowledgment

I would like to thank my advisor, Dr. John Albeck, for his mentorship during my PhD. Thank you for your support, advice, and encouragement, which made this work possible. Working with you has been the best years of my life. My thanks to Dr. Mark Huising, Dr. Oliver Fiehn, and Dr. Ted Powers for their feedback and support as my committee members. I would like to extend my gratitude to Dr.Eric Deeds, Dr.Breanne Sparta, and Dr. Michael Pargett, who always provide useful comments and engaging conversation. I extend my thanks to my dear friend, Shaoming Wang, who helps crystalize my ideas. I thank all of my labmates for their inputs on my work. Lastly, I cannot achieve all of this work without constant support from my family.

Chapter 1

Introduction

1.1. Abstract

This introductory chapter provides an overview of the importance of cell signaling heterogeneity at a single-cell level. Growth signals such as ERK and AKT are known to be heterogeneous and dynamic across cell populations. Secondly, a comprehensive review of the complex interplay between key growth signals and cell metabolism state through the ERK-AKT-AMPK axis is provided. Lastly, single-cell metabolism is discussed to provide context for my subsequent studies. This chapter has five sections :

1. Overview of single-cell signaling dynamics.
2. The need for multiplexed studies of single-cell dynamics.
3. Single-cell metabolic heterogeneity.
4. Review of crosstalk between growth signaling and metabolism through the ERK-AKT-AMPK network.
5. Kinase activity measurements at the single-cell level with fluorescence biosensors.

1.2. Overview of single-cell signaling dynamics studies

Cellular homeostasis depends on the ability to process intracellular information, such as metabolic states, and extracellular cues, such as growth factors, simultaneously. Network responses to a stimulus or drug treatment are heterogeneous across cell populations, due to both genetic and non-genetic variance (Lun and Bodenmiller, 2020). Many biological processes, including proliferation, differentiation, and energy metabolism, are regulated by dynamic signaling networks (Clapham, 2007; Groves and Kuriyan, 2010; Hetz and Saxena, 2017; Yu et al., 2015). These networks consist of signaling proteins, with the best known being kinases and phosphatases that regulate protein phosphorylation. Thus, studying the phosphorylation status of signaling pathways can often be used to interrogate signaling pathway activation. Classically, cell

signaling research has focused on identifying the cascade of individual signaling pathways or identifying essential kinase-substate activity from these pathways that regulate important cell function and provide methods for cell signaling manipulation. Predominantly, the field has relied on biochemical measurements, such as western blots, that require bulk cell populations and do not account for cell-to-cell variability and have a very low temporal resolution.

More recent work has revealed that cell signaling is a dynamic process that cannot be fully understood with snapshot measurements. The ERK pathway is a prime example of the importance of single-cell signaling dynamics. ERK is a member of the mitogen-activated protein kinase (MAPK) family and phosphorylates hundreds of downstream target proteins, including transcription factors that control genes involved in cell proliferation and cell survival (Yoon and Seger, 2006a). In the MCF10A cell line, epidermal growth factor (EGF) at high concentration (10 ng/ml) induces sustained ERK activation, while low EGF concentration (0.001 – 0.1 mg/ml) results in pulsatile activation of ERK (Albeck et al., 2013a; Aoki et al., 2013; Regot et al., 2014). The dynamics of ERK activity can determine cell fate decisions. The PC12 cell line provides a well-studied example of this concept, where nerve growth factor (NGF) induces sustained ERK activation and cell differentiation, while EGF stimulation induces transient ERK pulses that result in cell proliferation (Marshall, 1995; Santos et al., 2007). More recently, single-cell analysis of PC12 revealed that ERK responses to NGF and EGF are heterogeneous. NGF drives ERK toward sustained activation, and EGF drives ERK toward transient activation (Ryu et al., 2015). Further study showed that repeated EGF stimulation in PC12 could induce sustained ERK activation similar to the NGF effect, and it results in PC12 differentiation just like NGF stimulation. The decision to proliferate or differentiate thus depends on the level of ERK activity and not stimulus specificity (Chen et al., 2012). These studies exemplify the importance of the temporal pattern of signaling cascade on cell fate decisions.

1.3. The need for multiplexed studies of single-cell dynamics.

Cellular information is not only carried over time but also 'spreads' to other pathways. Signaling pathways are, in fact, highly interconnected. There are two modes of how cell signaling information can be directly or indirectly carried across pathways. For direct crosstalk, an enzyme in one pathway directly regulates another component of the second pathway through direct binding or changing phosphorylation status, which produces an output that is different from each individual pathway activation. But more generally, indirect signaling crosstalk can involve kinase-independent modes of action. For example, the transcriptional output of one pathway may control the expression of components in the second pathway. Indirect signaling crosstalks thus can create widespread modifications of pathway activities, resulting in complex signaling behavior and composite cellular output (Fey et al., 2012; Vert and Chory, 2011).

One of the significant sources for indirect cross talk comes from cell metabolism. It is known that cell signaling can directly alter cell metabolism, with one of the best-known examples being the insulin signaling pathway, in which insulin upregulates surface expression of glucose transporter (GLUT) proteins, resulting in increased glycolysis (Watson and Pessin, 2001). The impact of such changes in metabolic flux on signaling is still an emerging area, but a few examples suggest that cell metabolism plays a significant role in signaling cascades. First, multiple receptor tyrosine kinases, such as IL-3 receptor, TGF-b receptor, and EGFR, require glycosylation for surface expression. Glucose withdrawal or glucose uptake inhibition results in significant growth retardation through downregulation of receptor tyrosine kinase surface expression (Fang et al., 2010; Wellen et al., 2010; Wu and Derynck, 2009). Histone modification is another metabolically regulated process. In mammalian cells, histone acetylation is required to open chromatin structure and control gene expression (Li et al., 2007). Evidence in yeast suggests that the altered availability of acetyl-CoA, the key acetyl donor, directly changes histone acetylation status at many sites in the genome (Cai et al., 2011). Another mechanism by which cells sense metabolic

state to alter signaling cascades is through mTORC1 activity. The presence of amino acids and glucose recruits mTORC1 to the lysosomal surface, its primary site of activation (Saxton and Sabatini, 2017). These studies provide evidence that multiplexed-high-temporal-resolution signaling behavior measurement is required to establish signaling network kinetics and causality.

1.4. Single-cell metabolic heterogeneity

Metabolism is the core cellular process. It is known that metabolism varies across cell types and tissues (Hensley et al., 2016; Konagaya et al., 2017; Tasdogan et al., 2020). However, very little is known about metabolic heterogeneity within the same cell population. As mentioned earlier, the majority of cell-to-cell heterogeneity can arise from non-genetic factors. Metabolism might be a key source of cell-to-cell heterogeneity. However, the current approach to metabolic studies, such as mass spectrometry and flux analysis, relies on bulk input to increase metabolite signals and does not have any single-cell resolution measurement (Vasdekis and Stephanopoulos, 2015). Furthermore, to have a comprehensive understanding of metabolism, both metabolite concentrations and their fluxes are needed, which are difficult to obtain even at bulk. Most single-cell metabolic studies measure metabolic state by gene expression profiles (Artyomov and Van den Bossche, 2020). However, this approach is an indirect measurement of metabolism and captures only a ‘snapshot’ metabolic activity.

The best source of direct single-cell metabolism measurements thus far comes from studies in yeast. In a nutrient-limited condition, yeast exhibits synchronous and periodic metabolic cycles composed of a reductive phase, where glycolytic activity is elevated and biochemical molecule uptake increases. This is followed by a distinct oxidative phase, where oxygen consumption is increased, and yeast shows higher anabolic activity (Tu et al., 2005). An intriguing question raised by this work is whether mammalian cells might also exhibit such cyclic metabolic behavior. However, there is no known method to synchronize mammalian cell metabolism to allow bulk measurement of metabolites.

In chapter 2, we approach the problem of single-cell metabolism by measuring AMP-activated kinase (AMPK) function through the AMPKAR2 FRET biosensor. AMPK is a heterotrimeric complex of serine/threonine kinase that is activated upon binding to AMP/ADP, thus acting like an intra-cellular fuel gauge. AMPK activation requires two factors: direct binding of AMP/ADP on AMPK subunit and AMPK threonine 172 phosphorylation by its upstream kinase, LKB1 (Herzig and Shaw, 2018). Activated AMPK redirects cell metabolism towards higher catabolism and lower anabolism through direct phosphorylation on multiple targets, including mTOR complex 1 (mTORC1) (Gwinn et al., 2008; Inoki et al., 2003) and glycolytic enzymes (Bando et al., 2005; Wu et al., 2013). In a long-term effect, AMPK also redirects cellular metabolism through transcriptional regulation by increasing the expression of genes in mitochondrial biogenesis and autosomal degradation (Mihaylova and Shaw, 2011).

We are particularly interested in oxidative phosphorylation (OXPHOS), which theoretically provides more than 90% of cellular ATP production. OXPHOS is a potential source of metabolic heterogeneity since evidence in yeast suggests that OXPHOS activity can vary cyclically. Furthermore, in the past few years, OXPHOS inhibitors, such as IACS-010759 (Molina et al., 2018) and Gboxin (Shi et al., 2019), have been investigated as potential cancer therapy targets. Cell-to-cell OXPHOS heterogeneity, therefore potentially leads to therapeutic resistance for this class of drugs.

1.5. Review of growth signaling and metabolic crosstalk through ERK-AKT-AMPK axis

Cell signaling and cellular metabolism are inter-dependent in controlling cell fate decisions. (Mccubrey et al., 2007; Yoon and Seger, 2006). ERK signaling has been shown to be highly dynamic, and the kinetics of its activation and deactivation play a critical role in cell fate determination (Jones and Kazlauskas, 2001; OShaughnessy et al., 2011; Traverse et al., 1992). Recently, several studies have identified mechanisms by which cellular metabolic status is

modulated by ERK pathway activity (Abildgaard and Guldberg, 2015; Grassian et al., 2011; Haq et al., 2013; Nagarajan et al., 2016), but very little is known about how these metabolic changes control ERK dynamics, or their ultimate effect on cell fate (Verlande et al., 2017).

The ERK signaling cascade is essential for proper cell function. Mutations in the ERK signaling pathway result in developmental failure, and overactivation of ERK signal results in cancer development (Kim and Choi, 2010; Wortzel and Seger, 2011). Under physiological conditions, ERK activity has been shown to be highly dynamic (Albeck et al., 2013b; Hiratsuka et al., 2015), and ERK activation duration and amplitude may play a significant role in cell fate decisions, including proliferation, survival, and apoptosis (Mccubrey et al., 2007; Yoon and Seger, 2006b). The amplitude and duration of ERK dynamics are partially determined by canonical ERK signaling cascades, starting with dimerization of receptor tyrosine kinase (RTK), which then recruits SOS and activates RAS on the surface membrane. Activated RAS then activates the three-tier kinase cascade of RAF, MEK, and ERK. Phosphorylated ERK is an effector of the pathway that can phosphorylate multiple downstream target proteins involved in cell proliferation and survival (Sun et al., 2015).

Interestingly, the ERK signaling pathway can crosstalk with multiple metabolic input signals. Two of the essential metabolic signals are AKT (Moelling et al., 2002) and AMPK (Shen et al., 2013). AKT is an effector of the Insulin-PI3K-AKT axis that plays a significant role in glycolytic upregulation. For example, AKT upregulates the surface expression of glucose transporters and phosphorylates multiple glycolytic enzymes such as PFK2 and can indirectly increase PFK1 activity (Manning and Toker, 2017). Apart from metabolic upregulation, AKT can cross inhibit ERK signaling through direct phosphorylation on S364 RAF (Manning and Toker, 2017), which results in sequestration of RAF by 14-3-3 from its target MEK. Another essential metabolic signal capable of modulating ERK signaling is AMPK. The primary role of AMPK is to sense metabolic stress through intracellular ATP to AMP ratio (Gowans et al., 2013; Hardie et al.,

2016). Under metabolic stress, where the concentration of AMP rises, AMP binds directly to AMPK to promote an activating phosphorylation event by LKB1 on AMPK. Activated AMPK regulates several downstream targets, which ultimately result in increased cellular catabolism and reduced anabolism (Garcia and Shaw, 2017). AMPK can cross inhibit ERK signaling by direct phosphorylation on B-RAF at S729 (Shen et al., 2013), which results in 14-3-3 binding and sequestration of B-RAF in an inactive form. Thus, AMPK also plays a role in ERK signaling modulation.

Because AKT and AMPK promote different metabolic functions, it is surprising that both signals result in inhibition of the ERK cascade. This contradiction suggests that ERK regulation by AKT and AMPK might be subtle and may occur at specific conditions, locations, and times. This observation calls for temporal-sensitive measurement of ERK under the influence of AKT and AMPK activity. Furthermore, both AKT and AMPK activity are dependent on each other. AKT can directly phosphorylate and inhibit LKB1 activation of AMPK. AKT can also indirectly decrease AMPK activity by an increase in glycolysis and thus increase cellular energy charge. Thus it is necessary to monitor AMPK, AKT, and ERK activity simultaneously in order to delineate the influence of AKT and AMPK on the RAS/MAPK signaling pathway.

Apart from controlling cell proliferation and cell survival, ERK signaling also regulates many aspects of cellular metabolism. For example, ERK overactivation drives pancreatic tumors by increasing glucose uptake (Ying et al., 2012). More importantly, ERK overactivation accounts for 30% of all cancers (Fernández-Medarde and Santos, 2011), and most over-activating mutations, such as oncogenic RAS mutations, remain undruggable. Using metabolic perturbations is a possible tool available to control RAS overactivation. However, studies of metabolic control in oncogenic RAS are difficult, mainly because cancer cell lines contain multiple mutations that might confound the finding. Unsurprisingly, there are only a few studies on how metabolic perturbation might affect ERK signaling (Verlande et al., 2017). As a result, the effect of metabolic stress on

ERK signal alteration is not well characterized. However, single-cell measurements of ERK signaling can now provide a higher sensitivity, which should enable a more accurate characterization ofmetabolic effects on the ERK cascade. The recent development of fluorescent kinase reporters allows for direct measurements of protein kinase activity by time-lapse fluorescent imaging. By expressing AKT, AMPK, and ERK kinase reporters in the same cell, it is now possible to measure the activity of these kinases in real-time at a single-cell level and allow a detailed measurement of crosstalk in the AMPK-AKT-ERK axis.

1.6. Kinase activity measurement at the single-cell level with fluorescence biosensors.

Co-measurement of cellular metabolic state and growth signaling activity is the key to understanding cell growth decisions. Genetically-encoded fluorescent kinase biosensors allow measurement of kinase activity at a single-cell level, with high time resolution, and can be scaled up to four simultaneous signal measurements. This technology has overcome the limitations of fixed single-cell measurement, such as immunofluorescence microscopy or droplet-based sequencing. This type of single-cell measurement is minimally invasive to the cell state. Thus the measurement has higher fidelity to an underlying cell state. Furthermore, these sensors are synthetic substrates of kinase of interest, and therefore they are subject to the same type of regulation as endogenous substrate. This section details biosensors that will be used throughout this dissertation.

1.6.1. AMPKAR2 – FRET biosensor

AMPKAR2 sensor is an AMP-activated kinase (AMPK) reporter (Hung et al., 2017; Tsou et al., 2011). It utilizes Förster resonance energy transfer (FRET) to read out changes in AMPK activity. The reporter protein is composed of mTurquoise (cyan) and Ypet (yellow) fluorescent proteins, connected by a flexible linker to a synthetic AMPK phosphorylation site and a WW phospho-binding domain. When AMPK is active, it will phosphorylate the AMPK phosphorylation site on the sensor. The phosphorylated reporter then folds through binding of phosphorylated

AMPK site and WW phospho-binding domain, bringing the mTurquoise and Ypet fluorophores closer to each other and allowing FRET energy transfer to occur. Briefly, photons emitted from the FRET donor, mTurquoise, are transferred to the FRET acceptor, Ypet. This energy transfer can be measured as diminished mTurquoise intensity using fluorescent microscopy. The significant advantage of this type of sensor is that, since FRET is an intramolecular event, it is independent of cellular machinery apart from the kinase of interest itself. However, there are two major drawbacks. First, it requires two fluorescent channels to function, limiting multiplexing possibilities. Secondly, FRET fluorophore pairs such as CFP-YFP occupy a large part of the visual spectrum available for fluorescence, which reduces the opportunity for multiplexed measurementswith other probes.

1.6.2. Kinase Translocation Reporters

Unlike FRET reporter, kinase translocation reporter (KTR) utilizes protein translocation between nuclear and cytosolic compartments as a read-out of kinase activity. KTR can be classified into two categories.

1.6.2.1. Engineered KTRs

This class of KTR was first proposed by Regot et al. (Regot et al., 2014). It comprises three components: a fluorescent protein of choice that is fused with a kinase docking site and an engineered phosphorylation site optimized to allow maximal nuclear-cytosolic translocation. Briefly, this phosphorylation site is composed of a negatively phospho-regulated nuclear localization sequence (NLS) and a positively phospho-regulated nuclear export sequence (NES). The ERK-KTR (ERKTR) sensor is an example of this type of sensor that will be used in this dissertation. Mechanistically, when ERK is active, it will bind to an ERK docking domain on the ERKTR sensor and then phosphorylate both the NLS and NES sites. This results in a shift from the nuclear compartment (unphosphorylated) to the cytosolic compartment (phosphorylated) of

the KTR sensor. ERK activity is measured by the ratio of fluorescent intensity in the cytosol to the nucleus. There are two critical benefits of this type of sensor. First, it requires only one fluorophore and thus minimizes fluorescent spectral overlap to allow multiplexed kinase measurements in a single cell. Secondly, since the docking and phosphorylation site are engineered, may be less susceptible to phosphorylation by non-specific kinases.

1.6.2.2. Native KTRs

This class of KTR utilizes native protein substrates that translocate between nuclear and cytosolic compartments when phosphorylated. The key sensor that uses this technique in this study is AKT-KTR sensor (Hung et al., 2017). The AKT-KTR sensor comprises two components: N-terminus (aa 1 – 400) of FOXO3a transcription factor fused with fluorophore of interest (Maryu et al., 2016). FOXO3a is a transcription factor regulated by AKT phosphorylation. Phosphorylated FOXO3a binds to 14-3-3 proteins, which sequester FOXO3a in the cytosol. On the other hand, when AKT is inhibited, FOXO3a translocates into the nucleus and binds to DNA. Since this type of KTR can cause overexpression effects due to its transcription factor function, we delete the C-terminus of FOXO3a, which contains its DNA binding motif, to minimize the effect of FOXO3a transcription function.

Similar to the ERKTR sensor, AKT kinase activity is measured by the ratio of fluorescent intensity in the cytosol to the nucleus. A major benefit of this sensor is that it is simple to design since it requires only known kinase substrates that translocate. However, it has a few drawbacks. First, as mentioned earlier, this type of sensor requires overexpression of a signaling protein, and thus cell state might be perturbed by the sensor expression itself. Secondly. since one protein might contain multiple phosphorylation sites for multiple kinases, the read-out might be subject to non-specificity.

The main benefit of KTR sensors is that they allow multi-kinase measurement in the same cell. However, in both engineered KTR and native KTR, the common drawback is that the

dynamics are subject to changes in nuclear import and export rates, adding additional noise to the measurement.

1.7. References

Abildgaard, C., and Guldberg, P. (2015). Molecular drivers of cellular metabolic reprogramming in melanoma. Trends Mol. Med. *21*, 164–171.

Albeck, J.G., Mills, G.B., and Brugge, J.S. (2013a). Frequency-modulated pulses of ERK activity transmit quantitative proliferation signals. Mol Cell *49*, 249–261.

Albeck, J.G., Mills, G.B., and Brugge, J.S. (2013b). Frequency-Modulated Pulses of ERK Activity Transmit Quantitative Proliferation Signals. Mol. Cell *49*, 249–261.

Aoki, K., Kumagai, Y., Sakurai, A., Komatsu, N., Fujita, Y., Shionyu, C., and Matsuda, M. (2013). Stochastic ERK activation induced by noise and cell-to-cell propagation regulates cell density-dependent proliferation. Mol. Cell *52*, 529–540.

Artyomov, M.N., and Van den Bossche, J. (2020). Immunometabolism in the Single-Cell Era. Cell Metab. *32*, 710–725.

Bando, H., Atsumi, T., Nishio, T., Niwa, H., Mishima, S., Shimizu, C., Yoshioka, N., Bucala, R., and Koike, T. (2005). Phosphorylation of the 6-phosphofructo-2-kinase/fructose 2,6-bisphosphatase/PFKFB3 family of glycolytic regulators in human cancer. Clin. Cancer Res. an Off. J. Am. Assoc. Cancer Res. *11*, 5784–5792.

Cai, L., Sutter, B.M., Li, B., and Tu, B.P. (2011). Acetyl-CoA Induces Cell Growth and Proliferation by Promoting the Acetylation of Histones at Growth Genes. Mol. Cell *42*, 426–437.

Chen, J.-Y., Lin, J.-R., Cimprich, K.A., and Meyer, T. (2012). A two-dimensional ERK-AKT signaling code for an NGF-triggered cell-fate decision. Mol. Cell *45*, 196–209.

Clapham, D.E. (2007). Calcium signaling. Cell *131*, 1047–1058.

Fang, M., Shen, Z., Huang, S., Zhao, L., Chen, S., Mak, T.W., and Wang, X. (2010). The ER UDPase ENTPD5 promotes protein N-glycosylation, the Warburg effect, and proliferation in the PTEN pathway. Cell *143*, 711–724.

Fernández-Medarde, A., and Santos, E. (2011). Ras in Cancer and Developmental Diseases. Genes Cancer *2*, 344–358.

Fey, D., Croucher, D.R., Kolch, W., and Kholodenko, B.N. (2012). Crosstalk and signaling switches in mitogen-activated proteinkinase cascades. Front. Physiol. *3*, 355.

Garcia, D., and Shaw, R.J. (2017). AMPK: Mechanisms of Cellular Energy Sensing and Restoration of Metabolic Balance. Mol. Cell *66*, 789–800.

Gowans, G.J., Hawley, S.A., Ross, F.A., and Hardie, D.G. (2013). AMP is a true physiological regulator of amp-activated protein kinase by both allosteric activation and enhancing net phosphorylation. Cell Metab. *18*, 556–566.

Grassian, A.R., Metallo, C.M., Coloff, J.L., Stephanopoulos, G., and Brugge, J.S. (2011). Erk regulation of pyruvate dehydrogenase flux through PDK4 modulates cell proliferation. Genes Dev. *25*, 1716–1733.

Groves, J.T., and Kuriyan, J. (2010). Molecular mechanisms in signal transduction at the membrane. Nat. Struct. Mol. Biol. *17*, 659–665.

Gwinn, D.M., Shackelford, D.B., Egan, D.F., Mihaylova, M.M., Mery, A., Vasquez, D.S., Turk, B.E., and Shaw, R.J. (2008). AMPK phosphorylation of raptor mediates a metabolic checkpoint. Mol. Cell *30*, 214–226.

Haq, R., Shoag, J., Andreu-Perez, P., Yokoyama, S., Edelman, H., Rowe, G.C., Frederick, D.T., Hurley, A.D., Nellore, A., Kung, A.L., et al. (2013). Oncogenic BRAF regulates oxidative metabolism via PGC1α and MITF. Cancer Cell *23*, 302–315.

Hardie, D.G., Schaffer, B.E., and Brunet, A. (2016). AMPK: An Energy-Sensing Pathway with Multiple Inputs and Outputs. Trends Cell Biol. *26*, 190–201.

Hensley, C.T., Faubert, B., Yuan, Q., Lev-Cohain, N., Jin, E., Kim, J., Jiang, L., Ko, B., Skelton, R., Loudat, L., et al. (2016). Metabolic Heterogeneity in Human Lung Tumors. Cell *164*, 681–694.

Herzig, S., and Shaw, R.J. (2018). AMPK: guardian of metabolism and mitochondrial homeostasis. Nat. Rev. Mol. Cell Biol. *19*, 121–135.

Hetz, C., and Saxena, S. (2017). ER stress and the unfolded protein response in neurodegeneration. Nat. Rev. Neurol. *13*, 477–491.

Hiratsuka, T., Fujita, Y., Naoki, H., Aoki, K., Kamioka, Y., and Matsuda, M. (2015). Intercellular propagation of extracellular signal-regulated kinase activation revealed by in vivo imaging of mouse skin. Elife *4*, e05178.

Hung, Y.P., Teragawa, C., Kosaisawe, N., Gillies, T.E., Pargett, M., Minguet, M., Distor, K., Rocha-Gregg, B.L., Coloff, J.L., Keibler, M.A., et al. (2017). Akt regulation of glycolysis mediates bioenergetic stability in epithelial cells. Elife *6*.

Inoki, K., Zhu, T., and Guan, K.-L. (2003). TSC2 mediates cellular energy response to control cell growth and survival. Cell *115*, 577–590.

Jones, S.M., and Kazlauskas, A. (2001). Growth-factor-dependent mitogenesis requires two distinct phases of signalling. Nat. Cell Biol. *3*, 165–172.

Kim, E.K., and Choi, E.J. (2010). Pathological roles of MAPK signaling pathways in human diseases. Biochim. Biophys. Acta - Mol. Basis Dis. *1802*, 396–405.

Konagaya, Y., Terai, K., Hirao, Y., Takakura, K., Imajo, M., Kamioka, Y., Sasaoka Norioand Kakizuka, A., Sumiyama, K., Asano, T., and Matsuda, M. (2017). A Highly Sensitive FRET Biosensor for AMPK ExhibitsHeterogeneous AMPK Responses among Cells and Organs. Cell

Rep. *21*, 2628–2638.

Li, B., Carey, M., and Workman, J.L. (2007). The role of chromatin during transcription. Cell *128*, 707–719.

Lun, X.-K., and Bodenmiller, B. (2020). Profiling Cell Signaling Networks at Single-cell Resolution. Mol. Cell. Proteomics *19*, 744–756.

Manning, B.D., and Toker, A. (2017). AKT/PKB Signaling: Navigating the Network. Cell *169*, 381–405.

Marshall, C.J. (1995). Specificity of receptor tyrosine kinase signaling: transient versus sustained extracellular signal-regulated kinase activation. Cell *80*, 179–185.

Maryu, G., Matsuda, M., and Aoki, K. (2016). Multiplexed Fluorescence Imaging of ERK and Akt Activities and Cell-cycle Progression. Cell Struct. Funct. *41*, 81–92.

Mccubrey, J.A., Steelman, L.S., Chappell, W.H., Abrams, S.L., Wong, W.T., Chang, F., Lehmann, B., Terrian, D.M., Milella, M., Stivala, F., et al. (2007). Roles Of The RAS/MEK/ERK pathway in Cell Growth, Malignant Transformation and Drug Resistance. Biochim. Biophys. Acta - Mol. Cell Res. *1773*, 1263–1284.

Mihaylova, M.M., and Shaw, R.J. (2011). The AMPK signalling pathway coordinates cell growth, autophagyand metabolism. Nat. Cell Biol. *13*, 1016–1023.

Moelling, K., Schad, K., Bosse, M., Zimmermann, S., and Schweneker, M. (2002). Regulation of Raf-Akt Cross-talk. J. Biol. Chem. *277*, 31099–31106.

Molina, J.R., Sun, Y., Protopopova, M., Gera, S., Bandi, M., Bristow, C., McAfoos, T., Morlacchi, P., Ackroyd, J., Agip, A.-N.A., et al. (2018). An inhibitor of oxidative phosphorylation exploits cancer vulnerability. Nat. Med. *24*, 1036–1046.

Nagarajan, A., Malvi, P., and Wajapeyee, N. (2016). Oncogene-Directed Alterations in Cancer Cell Metabolism. Trends in Cancer *2*, 365–377.

OShaughnessy, E.C., Palani, S., Collins, J.J., and Sarkar, C.A. (2011). Tunable signal processing in synthetic MAP kinase cascades. Cell *144*, 119–131.

Regot, S., Hughey, J.J., Bajar, B.T., Carrasco, S., and Covert, M.W. (2014). High-sensitivity measurements of multiple kinase activities in live single cells. Cell *157*, 1724–1734.

Ryu, H., Chung, M., Dobrzyński, M., Fey, D., Blum, Y., Lee, S.S., Peter, M., Kholodenko, B.N., Jeon, N.L., and Pertz, O. (2015). Frequency modulation of ERK activation dynamics rewires cell fate. Mol. Syst. Biol. *11*, 838.

Santos, S.D.M., Verveer, P.J., and Bastiaens, P.I.H. (2007). Growth factor-induced MAPK network topology shapes Erk response determining PC-12 cell fate. Nat. Cell Biol. *9*, 324–330.

Saxton, R.A., and Sabatini, D.M. (2017). mTOR Signaling in Growth, Metabolism, and Disease. Cell *168*, 960–976.

Shen, C.-H., Yuan, P., Perez-Lorenzo, R., Zhang, Y., Lee, S.X., Ou, Y., Asara, J.M., Cantley, L.C., and Zheng, B. (2013). Phosphorylation of BRAF by AMPK Impairs BRAF-KSR1 Association and Cell Proliferation. Mol. Cell *52*, 161–172.

Shi, Y., Lim, S.K., Liang, Q., Iyer, S. V, Wang, H.-Y., Wang, Z., Xie, X., Sun, D., Chen, Y.-J., Tabar, V., et al. (2019). Gboxin is an oxidative phosphorylation inhibitor that targets glioblastoma. Nature *567*, 341–346.

Sun, Y., Liu, W.-Z., Liu, T., Feng, X., Yang, N., and Zhou, H.-F. (2015). Signaling pathway of MAPK/ERK in cell proliferation, differentiation, migration, senescence and apoptosis. J. Recept. Signal Transduct. *35*, 600–604.

Tasdogan, A., Faubert, B., Ramesh, V., Ubellacker, J.M., Shen, B., Solmonson, A., Murphy, M.M.,

Gu, Z., Gu, W., Martin, M., et al. (2020). Metabolic heterogeneity confers differences in melanoma metastatic potential. Nature *577*, 115–120.

Traverse, S., Gomez, N., Paterson, H., Marshall, C., and Cohen, P. (1992). Sustained activation of the mitogen-activated protein (MAP) kinase cascade may be required for differentiation of PC12 cells. Comparison of the effects of nerve growth factor and epidermal growth factor. Biochem. J. *288 (Pt 2*, 351–355.

Tsou, P., Zheng, B., Hsu, C.H., Sasaki, A.T., and Cantley, L.C. (2011). A fluorescent reporter of AMPK activity and cellular energy stress. Cell Metab. *13*, 476–486.

Tu, B.P., Kudlicki, A., Rowicka, M., and McKnight, S.L. (2005). Logic of the yeast metabolic cycle: temporal compartmentalization of cellular processes. Science *310*, 1152–1158.

Vasdekis, A.E., and Stephanopoulos, G. (2015). Review of methods to probe single cell metabolism and bioenergetics. Metab. Eng. *27*, 115–135.

Verlande, A., Krafčíková, M., Potěšil, D., Trantírek, L., Zdráhal, Z., Elkalaf, M., Trnka, J., Souček, K., Rauch, N., Rauch, J., et al. (2017). Metabolic stress regulates ERK activity by controlling KSR-RAF heterodimerization. EMBO Rep. *19*, e201744524.

Vert, G., and Chory, J. (2011). Crosstalk in cellular signaling: background noise or the real thing? Dev. Cell *21*, 985–991.

Watson, R.T., and Pessin, J.E. (2001). Subcellular compartmentalization and trafficking of the insulin-responsive glucose transporter, GLUT4. Exp. Cell Res. *271*, 75–83.

Wellen, K.E., Lu, C., Mancuso, A., Lemons, J.M.S., Ryczko, M., Dennis, J.W., Rabinowitz, J.D., Coller, H.A., and Thompson, C.B. (2010). The hexosamine biosynthetic pathway couples growth factor-inducedglutamine uptake to glucose metabolism. Genes Dev. *24*, 2784–2799.

Wortzel, I., and Seger, R. (2011). The ERK cascade: Distinct functions within various subcellular

organelles. Genes and Cancer *2*, 195–209.

Wu, L., and Derynck, R. (2009). Essential role of TGF-beta signaling in glucose-induced cell hypertrophy. Dev. Cell *17*, 35–48.

Wu, N., Zheng, B., Shaywitz, A., Dagon, Y., Tower, C., Bellinger, G., Shen, C.-H., Wen, J., Asara, J., McGraw, T.E., et al. (2013). AMPK-dependent degradation of TXNIP upon energy stress leads to enhanced glucose uptake via GLUT1. Mol. Cell *49*, 1167–1175.

Ying, H., Kimmelman, A.C., Lyssiotis, C.A., Hua, S., Chu, G.C., Fletcher-Sananikone, E., Locasale, J.W., Son, J., Zhang, H., Coloff, J.L., et al. (2012). Oncogenic Kras Maintains Pancreatic Tumors through Regulation of Anabolic Glucose Metabolism. Cell *149*, 656–670.

Yoon, S., and Seger, R. (2006a). The extracellular signal-regulated kinase: multiple substrates regulate diverse cellular functions. Growth Factors *24*, 21–44.

Yoon, S., and Seger, R. (2006b). The extracellular signal-regulated kinase: Multiple substrates regulate diverse cellular functions. Growth Factors *24*, 21–44.

Yu, F.-X., Zhao, B., and Guan, K.-L. (2015). Hippo Pathway in Organ Size Control, Tissue Homeostasis, and Cancer. Cell *163*, 811–828.

Chapter 2

Linear single-cell AMPK measurement by AMPKAR2 FRET sensor

2.1. Abstract

This chapter summarizes how single-cell measurements of AMPK are performed at a single-cell level. Additional details on statistical analysis of AMPKAR2 sensor data are also provided. As mentioned in chapter 1, single-cell measurement is a key to understanding cell signaling. Unlike bulk measurements, single-cell measurement techniques present multiple challenges, including experimental design, a large volume of time-lapse image data, object tracking, and non-linearity of kinase sensor of interest.

2.2. Cell preparation of a live-cell experiment

Throughout this dissertation, most of the experiments are done in the MCF10A cell line MCF10A clone 5E (Janes et al., 2010). Routine cell culture for MCF10A cells was performed as previously described (Debnath et al., 2003). MCF10A was grown in 'DMEM/F12 growth medium' (see Media table). Primary stocks from the original clonal derivation (MCF10A-5E) or the ATCC (184A1) were used in all experiments. All cells were routinely split when they are ~80% confluent.

In live microscopy experiments, we used a custom formulation, termed 'imaging base-DMEM/F12', which consists of DMEM/F12 lacking glucose, glutamine, riboflavin, folic acid, and phenol red (Life Technologies or UC Davis Veterinary Medicine Biological Media Service) which allows adjustment of available nutrients and avoids fluorescence background. All experiments involving MCF10A cell line were performed in 'Imaging medium 1' (see Media composition). For experiments with other cell lines that are not either MCF10A or 184A1, 'Imaging medium 2' was used. For all experiments, 'Imaging medium 1' and 'Imaging medium 2' were supplied with glucose 17 mM and 25 mM, respectively, to imitate the full growth media of each cell line.

Before imaging, cells were washed twice with their respective media and then cultured in imaging experiment media at least 2 hours before imaging, unless indicated otherwise. The main reason for this incubation period is for AMPK activity to reset to normal baseline after growth media removal. The cell to media ratio was maintained at 150-200 cells/µl for all experiments. For experiments involving titration of insulin or EGF concentrations, cells were placed in EGF- or insulin-deficient media for 4 – 6 hours prior to imaging.

2.3. Live-cell fluorescent microscopy and image analysis

Time-lapse wide-field microscopy was performed as described previously (Hung et al., 2017; Pargett et al., 2017). Briefly, 25,000 cells were plated one day prior to imaging in glass-bottom 96-well plates (Cellvis P96-1.5H-N, Mountain View, CA) pretreated with type I collagen (Gibco A10483-01) to promote cell adherence. It is best to use glass-bottom plates since they are thin and have less optical interference than plastic bottom plates. The number of cells to plate has to be determined for each cell line. The critical consideration for cell numbers is to avoid cell overlapping since it will interfere with nuclei segmentation during image analysis.

Once image data is acquired from time-lapse microscopy. Images are subjected to the following analysis. (1) Background and flatfield correction: Since FRET sensor measurement requires an accurate ratio for FRET donor and FRET acceptor, background image intensity must be substracted from raw images. Furthermore, since the optics of the microscope are circular, but the sensor of the camera is rectangular, the illumination in each image is not equal, resulting in inaccurate measurement of fluorophore intensity. To correct the illumination anomaly, it is always best to image empty well in each experiment and perform spatial filter estimation of the illumination pattern. Afterward, we can use this estimated illumination pattern to normalize the original image to get the ‘flatfield’ images. (2) Nuclei identification: Because our AMPKAR2 sensor has an NES tag, which compartmentalizes the sensor in the cytosol, we could use un-illuminated nuclei as a nuclei marker. We automatically identify nuclei by applying intensity threshold and

shape threshold (e.g., nuclei size between 25 – 100 pixels and circularity) to create nuclear 'masks.' (3) Nuclear tracking: The position of nuclear masks were then used for object tracking over the whole time-lapse movie. The critical consideration is that the object should not move more than 5 pixels from the previous frame, and it should not disappear for more than three consecutive frames. (4) Intensity measurement: Once nuclear objects were tracked, the watershed method created cytoplasmic masks (Vincent and Soille, 1991) using cytosolic YFP to identify the cytosolic boundary. The cytosolic area is further restricted to the area within 5 pixels of the nuclear border. Intensities of fluorophore in cytosol and nuclei were in the defined region were collect and linked to the physical position of the object. (5) Cell trace analysis: The resulting single-cell time series traces were filtered for quality by a minimum length of the trace, typically at least 12 hours, and a maximum number of contiguous missing or corrupt data points, typically no more than three frames.

2.4. AMPKAR2 FRET reporter measurement

Even though we can measure AMPK kinase activity by measuring the ratio of YFP to CFP from AMPKAR2 FRET sensor, the change in fluorophore ratio does not precisely indicate how much of the sensor is phosphorylated. To quantify the phosphorylated fraction of the sensor, we first calculated FRET efficiency exactly as shown previously (Gillies et al., 2020), using a spectral model of light propagated through the microscopy system, including the live cell specimen. And since AMPKAR2 reporter is a substrate for AMPK kinase activity, it is possible to estimate the fraction of phosphorylated sensor using Phos-Tag™ electrophoresis, followed by immunoblot against GFP. Briefly, Phos-tag electrophoresis separates proteins based on their charge. Since AMPKAR2 sensor has only one phosphorylation site, phosphorylated AMPKAR2 will separate from the unphosphorylated sensor and appear in just one clear band above the unphosphorylated band (Figure 2.1.A). This measurement allows us to convert FRET ratio to the fraction of AMPKAR2 sensor that is phosphorylated, $AMPKAR2^{PHOS}$, which is more biologically relevant.

Lysates from the MCF-10A cell lines treated with condition indicated in Figure 2.1.A. were used. These conditions were selected because they exhibit sustained and homogeneous AMPKAR2 activity. After Phos-Tag western blotting, membranes were stained with an anti-GFP antibody (CST #2955) to visualize the AMPKAR2 reporter, and the average fraction of reporter phosphorylated was quantified. These values were then compared with the average fraction associated as calculated from live-cell experiments at corresponding treatments and time points. Linear fitting was performed and providing a calibrated measurement of the fraction of AMPKAR2 phosphorylated, based on live-cell measurements – eq 1 (Figure 2.1.B). This method of biosensor calibration is applicable to all FRET sensors that have low numbers, i.e., one to two, of phosphorylation sites

$$AMPKAR2^{PHOS} = 2.74[AMPKAR2_{FRET\ ratio}\ ] - 0.59 \qquad (1)$$

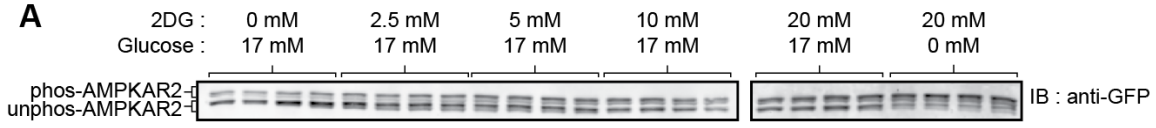

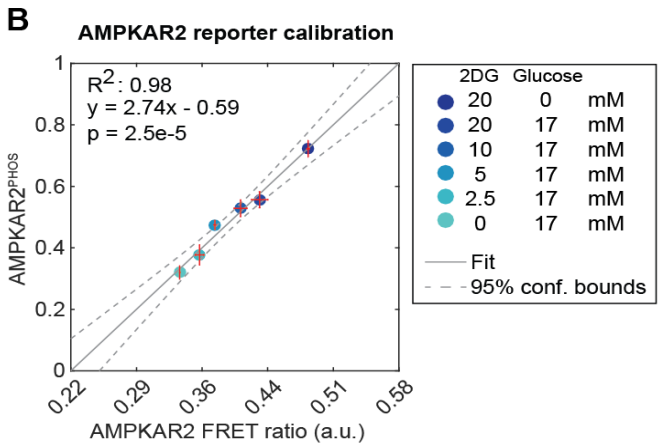

Figure 2.1. : AMPKAR2 FRET biosensor calibration

(A) Measurement of AMPKAR2 phosphorylation status by immunoblot. Image shows a representative immunoblot used to obtain the AMPKAR2^{PHOS} measurements in (C). Phos-tag gel electrophoresis was used to separate phosphorylated and unphosphorylated forms of the reporter (upper and lower bands, respectively), with anti-GFP used to detect both forms. N=4. (B) Scatter plot of the correlation between FRET ratio of AMPKAR2 reporter, as measured by live-cell microscopy, and its phosphorylation status, as measured by phos-tag gel electrophoresis under the same conditions. A range of AMPK activities were induced by varying glucose and 2-deoxyglucose (2DG). Error bars represent standard errors of the mean (SEM) from at least two different experiments. The solid line represents a fitted linear model, and the dashed lines show 95% confidence bounds. This fitted equation is used throughout the study to report all AMPKAR2 FRET measurements as the fraction of AMPKAR2 phosphorylated, AMPKAR2^{PHOS}. N=4.

2.5. Media Composition

DMEM/F12 growth media

Component	Vendor	Catalog number	Final Concentration
DMEM/F2	Gibco	11320-033	-
Horse Serum	Invitrogen	16050-122	5%
EGF	Peprotech	AF-100-15	20 ng/ml
Hydrocortisone	Sigma	H0888	0.5 mg/ml
Cholera toxin	Sigma	C8052	100 ng/ml
Insulin	Sigma	I9278	10 ug/ml

Imaging medium 1

Component	Vendor	Catalog number	Final Concentration
Imaging base-DMEM/F12	Gibco	Custom; equivalent to Gibco 11320-033 lacking glucose, glutamine, pyruvate, riboflavin, folic acid, and phenol red	-
D-glucose	Fisher	D16	17 mM
BSA	Invitrogen	16050-122	0.1% w/v
Hydrocortisone	Sigma	H0888	0.5 mg/ml
Cholera toxin	Sigma	C8052	100 ng/ml
Penicillin-Streptomycin	Gibco	15140122	100 U/ml
EGF	Peprotech	AF-100-15	20 ng/ml
Insulin	Sigma	I9278	10 ug/ml

Imaging medium 2

Component	Vendor	Catalog number	Final Concentration
Imaging base-DMEM/F12	Gibco	Custom; equivalent to Gibco 11320-033 lacking glucose, glutamine, pyruvate, riboflavin, folic acid, and phenol red	-
D-glucose	Fisher	D16	25 mM
BSA	Invitrogen	16050-122	0.1% w/v
Penicillin-Streptomycin	Gibco	15140122	100 U/ml

2.6. Reference

Debnath, J., Muthuswamy, S.K., and Brugge, J.S. (2003). Morphogenesis and oncogenesis of MCF-10A mammary epithelial acini grown in three-dimensional basement membrane cultures. Methods *30*, 256-268.

Gillies, T.E., Pargett, M., Silva, J.M., Teragawa, C.K., McCormick, F., and Albeck, J.G. (2020). Oncogenic mutant RAS signaling activity is rescaled by the ERK/MAPK pathway. Mol Syst Biol *16*, e9518.

Hung, Y.P., Teragawa, C., Kosaisawe, N., Gillies, T.E., Pargett, M., Minguet, M., Distor, K., Rocha-Gregg, B.L., Coloff, J.L., Keibler, M.A.*, et al.* (2017). Akt regulation of glycolysis mediates bioenergetic stability in epithelial cells. eLife *6*, 1-25.

Janes, K.A., Wang, C.-C., Holmberg, K.J., Cabral, K., and Brugge, J.S. (2010). Identifying single-cell molecular programs by stochastic

profiling. Nat Methods *7*, 311-317.

Pargett, M., Gillies, T.E., Teragawa, C.K., Sparta, B., and Albeck, J.G. (2017). Single-Cell Imaging of ERK Signaling Using Fluorescent Biosensors (Humana Press, New York, NY), pp. 35-59.

Vincent, L., and Soille, P. (1991). Watersheds in digital spaces: an efficient algorithm based on immersion simulations. IEEE Transactions on Pattern Analysis and Machine Intelligence *13*, 583-598.

Chapter 3

Transient phases of OXPHOS inhibitor resistance reveal underlying metabolic heterogeneity in single cells

Preface

This chapter was originally published in Cell Metabolism:

Kosaisawe N, Sparta B, Pargett M, Teragawa CK, Albeck JG. Transient phases of OXPHOS inhibitor resistance reveal underlying metabolic heterogeneity in single cells. Cell Metab. 2021 Mar 2;33(3):649-665.e8. doi: 10.1016/j.cmet.2021.01.014. Epub 2021 Feb 8. PMID: 33561427; PMCID: PMC8005262.

The article has been modified to satisfy the formatting requirements of this thesis

3.1. Abstract

Cell-to-cell heterogeneity in metabolism plays an unknown role in physiology and pharmacology. To functionally characterize cellular variability in metabolism, we treated cells with inhibitors of oxidative phosphorylation (OXPHOS) and monitored their responses with live-cell reporters for ATP, ADP/ATP, or activity of the energy-sensing kinase AMPK. Across multiple OXPHOS inhibitors and cell types, we identified a subpopulation of cells resistant to activation of AMPK and reduction of ADP/ATP ratio. This resistant state persists transiently for at least several hours and can be inherited during cell divisions. OXPHOS inhibition suppresses the mTORC1 and ERK growth signaling pathways in sensitive cells, but not in resistant cells. Resistance is linked to a multi-factorial combination of increased glucose uptake, reduced protein biosynthesis, and G0/G1 cell cycle status. Our results reveal dynamic fluctuations in cellular energetic balance and provide a basis for measuring and predicting the distribution of cellular responses to OXPHOS inhibition.

3.2. Introduction

Metabolic functions vary across different cell types and tissues (Hensley et al., 2016; Konagaya et al., 2017; Tasdogan et al., 2020), but much less is known about cell-to-cell metabolic heterogeneity. Single-cell resolution is important because cellular heterogeneity limits drug efficacy (Altschuler and Wu, 2010), and targeting of metabolic functions for therapeutic purposes will require identification of resistant subpopulations of cells. Current approaches measure the expression profiles of metabolic enzymes (Hartmann et al., 2020; Xiao et al., 2019), rather than directly assessing metabolites or their flux. Other work has used biosensors to reveal variability in clonal cell lines responding to inhibitors of metabolism (Hung et al., 2017) and in cellular metabolic disposition based on responses to glucose withdrawal (Depaoli et al., 2018). However, while it is typical for single-cell approaches to reveal heterogeneity, it is not clear how the observed variation originates within an isogenic population of cells, and what impact it has on pathways downstream of the immediate response.

To approach these questions, we focused on inhibitors of oxidative phosphorylation (OXPHOS), which are important both as tools to probe cellular metabolism and as treatments for diabetes and cancer. Naturally occurring OXPHOS inhibitors, including oligomycin, antimycin, and rotenone are produced defensively in microorganisms and plants. Biguanides derived from the plant compound galegine, including metformin and phenformin, are weaker inhibitors of OXPHOS. Metformin is used widely to treat type II diabetes and also has anti-tumorigenic, anti-fibrotic, and pro-longevity effects (Anisimov, 2010; Dos Santos et al., 2018). These effects have spurred the search for additional OXPHOS inhibitors, leading to the development of compounds including IACS-010759 and Gboxin, which are being evaluated as cancer therapies (Molina et al., 2018; Shi et al., 2019). Many cancers upregulate OXPHOS and the tricarboxylic acid (TCA) cycle and rely on them for ATP production, biosynthesis (Vander Heiden and DeBerardinis, 2017) or resistance to chemotherapy (Vashisht Gopal et al., 2019).

By inhibiting ATP generation, OXPHOS inhibitors induce metabolic stress, which can range in severity from mild activation of stress pathways to a lethal energetic crisis. Understanding the cellular response to OXPHOS inhibition will improve on existing treatments for diabetes, cancer, and other conditions (Ashton et al., 2018; Stoker et al., 2019) and illuminate the fundamental cell biology of metabolic stress responses (Wu et al., 2016). Potent OXPHOS inhibitors (e.g. oligomycin) block oxygen consumption within seconds (Ruas et al., 2018), preventing TCA cycle turning and increasing flux through glycolysis to compensate for ATP loss (Fan et al., 2013); this adaptation can occur quickly enough that ATP levels remain nearly constant (Hao et al., 2010). Cellular responses to OXPHOS inhibition involve signaling between the mitochondria and stress response proteins in the cytoplasm and nucleus (Quirós et al., 2017). Extracellular nutrients modulate the response to OXPHOS inhibition by determining the metabolic pathways available to compensate for the loss of oxidative ATP production and NADH oxidation (Gui et al., 2016). However, essentially all the known elements of the OXPHOS inhibitor response have been established as bulk properties of cell populations, potentially overlooking distinct subpopulations of individual cells that vary widely, as tissues do, in their usage of OXPHOS.

OXPHOS usage can be evaluated by the acute change in oxygen consumption upon treatment with oligomycin (Buttgereit and Brand, 1995). This perturbation-based approach is useful because measuring metabolic fluxes through tracing of labeled metabolites (Jang et al., 2018) or model-based reconstruction (Orth et al., 2010) require comprehensive measurements (Fendt et al., 2013; Hackett et al., 2016) that are infeasible in single cells. In contrast, the response to OXPHOS perturbation can provide a simple, functional measurement of a cell's usage of OXPHOS and glycolysis (Mookerjee et al., 2017) that can be compared across different cell types and tumors (Simões et al., 2015). At the single-cell level, measurements of oxygen consumption are possible (Dussmann et al., 2017), but other live-cell reporters may provide a more accessible quantification of OXPHOS activity. One such possibility is AMP-activated protein kinase (AMPK),

a primary contributor to the OXPHOS inhibition response. AMPK directly binds ATP, ADP, and AMP, and in response to decreased cellular energy charge (AMP and ADP relative to ATP)(Hardie and Hawley, 2001; Oakhill et al., 2011), it phosphorylates an array of substrates to enhance catabolism and suppress anabolism (Gowans et al., 2013; Hardie, 2014; Xiao et al., 2011). While AMPK is not required for all the effects of OXPHOS inhibition (Griss et al., 2015), its activity and phosphorylation status, or phosphorylation of its effectors such as acetyl-CoA carboxylase (ACC), are useful indicators of cellular energetic status. Recently, fluorescent protein-based FRET reporters have enabled tracking of AMPK activity in living cells, revealing the localization and kinetics of its activity in response to different forms of metabolic perturbation, including OXPHOS inhibition (Hung et al., 2017; Konagaya et al., 2017; Tsou et al., 2011).

Here, we used live-cell measurements of AMPK activity in response to OXPHOS inhibition to quantify differences in OXPHOS usage between single cells. We found that prominent cell-to-cell differences in AMPK response are common across OXPHOS inhibitors, and we confirmed that these changes correspond to perturbation of energy charge, using reporters for intracellular ATP concentration (Imamura et al., 2009) or ADP/ATP ratio (Tantama et al., 2013) and various supporting assays to make unambiguous measurements of metabolic changes. We find that individual cells interconvert between sensitive and resistant states on the scale of hours, and we demonstrate that each cell's response to OXPHOS inhibition is a function of the rate of insulin-stimulated glucose uptake relative to protein synthesis rate and cell cycle status. These findings establish that OXPHOS usage varies in a functionally important way between cells, and over time within the same cell.

3.3. Results

3.3.1. Variable AMPK responses to OXPHOS inhibition are common

In principle, strong activation of AMPK by OXPHOS inhibition indicates dependence on OXPHOS for ATP production (Gowans et al., 2013; Hao et al., 2010). Conversely, cells with

adequate capacity to generate ATP through other routes such as glycolysis would not experience a loss in energy charge and activation of AMPK upon OXPHOS inhibitor treatment. In MCF10A non-tumor epithelial cells, OXPHOS inhibitors targeting complexes I, III, and V of the electron transport chain induced a similar pattern: a sharp but variable initial increase in AMPK activity, followed by alternating cycles of inactivity and activity with an approximate period of 3 hours (Fig. 3.1.A). Metformin induced only a small initial peak, consistent with its weak inhibitory activity, but it induced subsequent oscillations similar to the other inhibitors (Fig. S3.1.A). In contrast to OXPHOS inhibitors, the direct AMPK activator AICAR produced a gradual rise to a new steady state of AMPK activity, without oscillations (Fig. S3.1.B).

To quantify OXPHOS inhibitor responses, we developed metrics for single-cell AMPK activity. We first confirmed that the average AMPKAR2 FRET ratio correlates linearly with its phosphorylation status across the full range of metabolic conditions tested (Fig. S3.1.C,D). AMPKAR2 phosphorylation ranged from ~30% in cells cultured with full growth medium to ~75% in cells deprived of glucose or treated with 2-deoxyglucose, ruling out saturation of the reporter and confirming that AMPK retains some activity even under full nutrient conditions (Gowans et al., 2013). We show all subsequent AMPKAR measurements as AMPKAR2^{PHOS}, the calibrated fraction of AMPKAR2 phosphorylated. On a cell-by-cell basis, AMPKAR2^{PHOS} correlated linearly with immunofluorescence (IF) for ACC phosphorylated at Ser-79 (pACC; R^2=0.63; Fig. 3.1.B and S1E). Both pACC and AMPKAR2^{PHOS} were bimodal, and >80% of cells were either double-positive or double-negative. Because we expect the initial change in AMPK activity to correlate with reliance on OXPHOS for ATP production at the time of treatment, we evaluated the baseline-to-peak amplitude of AMPKAR2^{PHOS} for each cell within 2 hours following oligomycin treatment (Fig. 3.1.C), which we term AMPKAR2Δ. AMPKAR2Δ was not correlated with basal AMPKAR2^{PHOS} (Fig. S3.1.F) and was distributed bimodally (Fig. 3.1.D). Similar distributions were found with rotenone, antimycin, and IACS-010759 (Fig. S3.1.G). We termed cells with a low

AMPKAR2Δ “OXPHOS-independent” (OP-ind) because they were able to withstand OXPHOS inhibition with little evidence of energy stress. Cells with a strong AMPK response were termed “OXPHOS-dependent” (OP-dep). In contrast to OXPHOS inhibitors, maximal doses of AICAR stimulated a uniform increase in AMPK activity across the entire population (Fig. S3.1.H), showing that heterogeneous responses are a property of OXPHOS inhibition, rather than AMPK activation.

To establish whether heterogeneous AMPK responses are shared by other cell types, we stably expressed AMPKAR2 and measured distributions of AMPKAR2Δ in other cell lines, including 184A1 (mammary epithelial), MCF7 (breast cancer), U87 (glioblastoma), and A549 (non-small cell lung cancer, LKB1-deficient)(Fig. 3.1.E). To compare equivalent conditions for all cells, oligomycin challenge was performed in the absence of insulin, which resulted in a lower fraction of OP-ind MCF10A cells (12%). Under the same conditions, AMPKAR2Δ in 184A1 cells was bimodally distributed, with a higher percentage of OP-ind cells (72%), suggesting that they have on average a higher capacity to maintain their ATP production independently of OXPHOS. In contrast, nearly 100% of MCF7 cells showed a strong AMPKAR2Δ, indicating a greater dependence on OXPHOS to maintain ATP homeostasis. U87 cells showed a broad distribution of responses, with both OP-ind and OP-dep populations. A549 cells, which are deficient for the AMPK activator LKB1, showed only weak AMPKAR2Δ, as expected. These data indicate that heterogeneity in the initial OXPHOS inhibitor response is common among human cell lines.

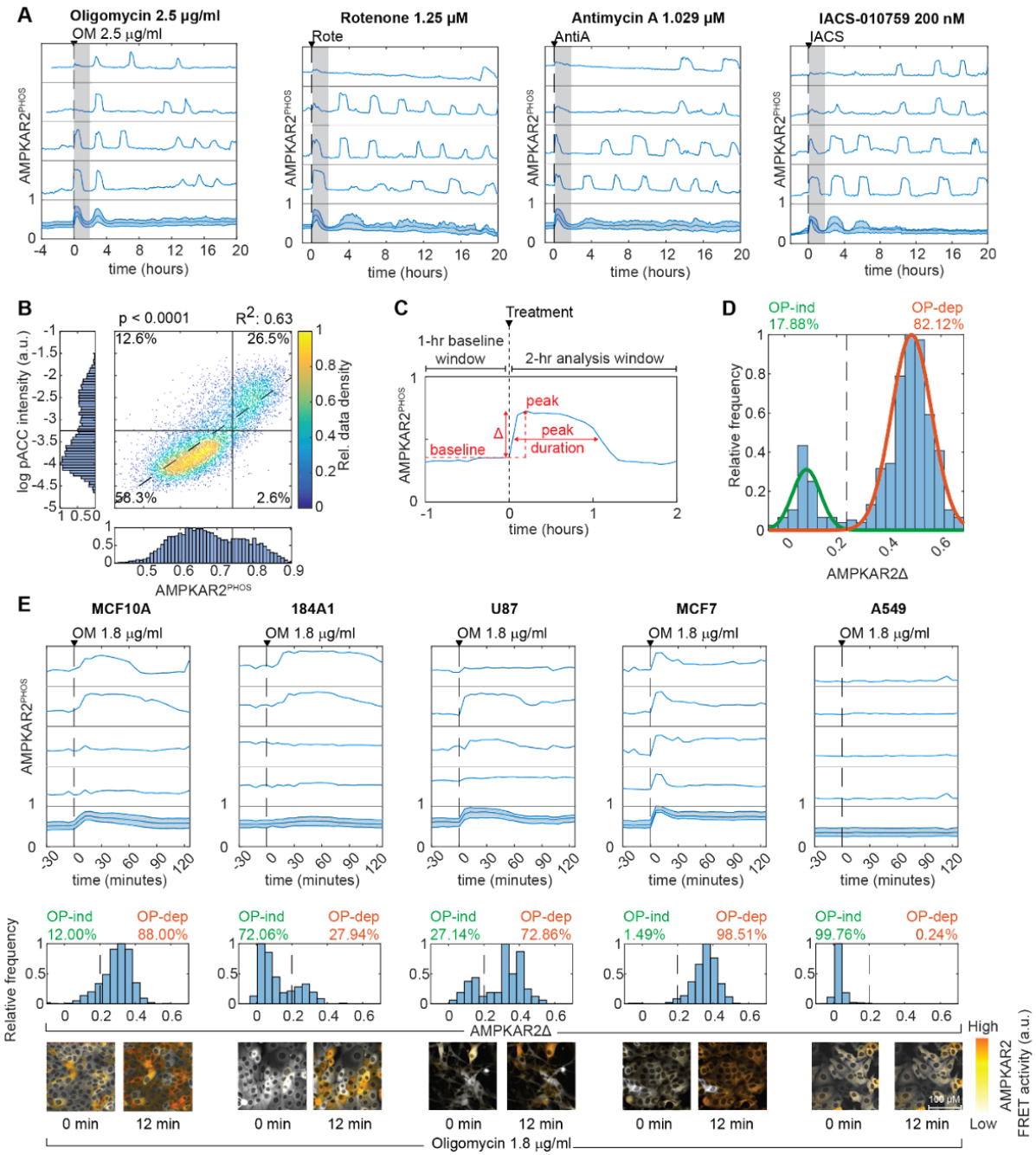

Figure 3.1 : **Variable AMPK responses to OXPHOS inhibition are common**

A: AMPKAR2^{PHOS} responses for cells grown in 17 mM glucose (see STAR Methods, imaging media table, for all formulations). Subplots represent single cells selected to depict the full range of responses, with population average and interquartile range in the bottom subplot. Gray shaded area shows the 2-hour time window used for analysis of peak height. N=2; see STAR Methods for definitions of replicates and cell numbers analyzed. B: Single-cell measurements of AMPKAR2^{PHOS} and pACC IF in MCF10A cells treated with 2.5 µg/ml oligomycin. AMPKAR2^{PHOS} was measured in live cells 15-18 minutes after treatment; pACC was measured following fixation and linked to AMPKAR2^{PHOS} for the same cell. R^2 and p-value are shown for a fitted linear function

(dashed line). N=2. C: Schematic of AMPKAR2 pulse parameterization. Peak activity was defined as the local maximum value within 2 hours after perturbation;

baseline was defined as the average of AMPKAR2 activity for one hour before treatment. Amplitude (AMPKARΔ) was calculated by subtraction of baseline from peak. D: Histogram of AMPKAR2Δ values after treatment with 2.5 µg/ml oligomycin. Green and orange lines are fitted Gaussian distributions. The dashed line is defined by the intersection between distributions and used as the cutoff for determining the percentage of OP-ind or OP-dep cells. N=2. E: Comparison of AMPK responses across cell lines. Top panels – representative AMPKAR2^{PHOS} measurements for cells grown in 17 mM glucose without insulin and EGF, treated with 1.8 µg/ml oligomycin. Each subplot represents a single cell measurement, with population average and interquartile range in the bottom subplot. Middle panels - histograms of AMPKAR2Δ in response to oligomycin (OM) 1.8 µg/ml treatment. Dashed lines are defined by the intersection of fitted bimodal distributions using pooled data for treated and untreated cells within each cell line. Bottom panels - sample images of AMPKAR2 responses. N=3.

3.3.2. Heterogeneous AMPK responses propagate to downstream signaling activity

AMPK inhibits the activities of the RAS/ERK pathway (Shen et al., 2013) and mTORC1 (Gwinn et al., 2008; Inoki et al., 2003) (Fig. 3.2.A). In MCF10A cells, we investigated whether heterogeneous activation of AMPK induces corresponding changes in these connected pathways. ERK activity was monitored simultaneously with AMPK using a translocation-based reporter, ERKTR (Regot et al., 2014). Upon oligomycin treatment, ERKTR detected an average decrease in ERK activity (Fig. 3.2.B), consistent with inhibition of this pathway by active AMPK. On a cell-by-cell basis, the reduction of ERK activity correlated with the magnitude of AMPK activation for each cell (Fig. 3.2.C,i), whereas no correlation was found in the absence of oligomycin. By IF, OP-dep cells showed a lower intensity of phospho-ERK staining (Fig. 3.2.C,ii). Furthermore, when time courses of AMPKAR2 and ERKTR signals were tracked over time in individual cells, a significant anti-correlation was observed where pulses of AMPK activity were matched by depressions in ERK activity (Fig. 3.2.D,i), with a lag time of 6 minutes or less (Fig. 3.2.E,i,ii).

To detect mTORC1 activity in live cells, we used the nuclear-to-cytosolic translocation of a fluorescent protein fusion to transcription factor EB (TFEB-TR), which is stimulated by

mTORC1-mediated phosphorylation (Fig. 3.2.A) (Li et al., 2018; Settembre et al., 2012). As in the case of ERKTR, TFEB-TR cytosolic-to-nuclear ratio was decreased following oligomycin treatment (Fig. 3.2.B) and correlated to AMPKAR2^{PHOS} at the single cell level (Fig. 3.2.C,iii). IF for phospho-4E-BP1, an mTORC1 substrate, was also reduced in OP-dep cells (Fig. 3.2.C,iv). Cycles of TFEB-TR translocation coincided with AMPK pulses, following a ~12 minute lag (Figs. 3.2.D,ii and 3.2.E,iii-iv). These results are consistent with dynamic regulation of mTORC1 by AMPK, although they do not rule out the possibility that OXPHOS inhibition suppresses mTORC1 independently of AMPK (Kalender et al., 2010). Together these data establish that heterogeneity in OXPHOS inhibitor responses has a functional impact on the AMPK signaling network.

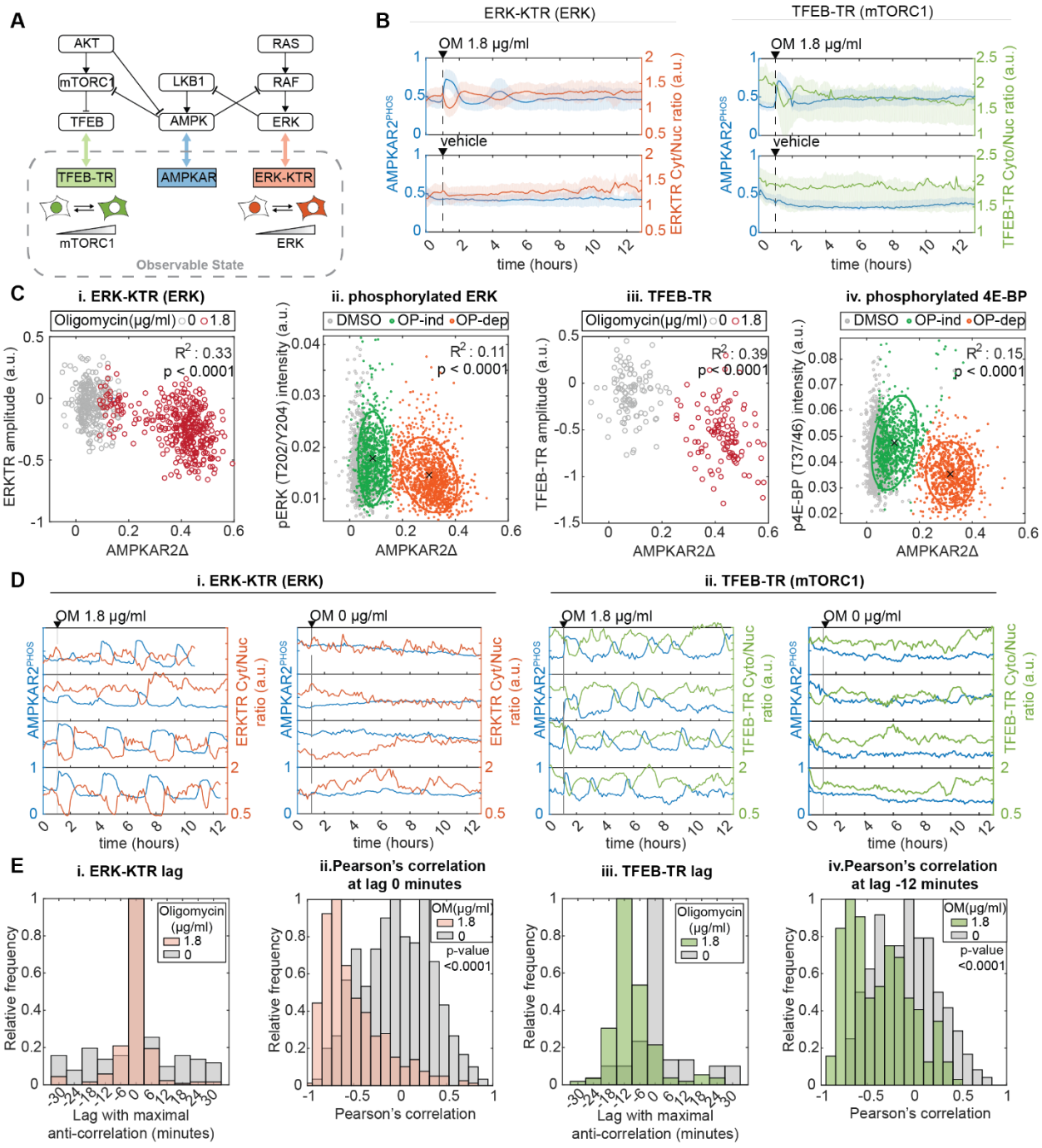

Figure 3.2 : Heterogeneous AMPK responses propagate to downstream signaling activity

A: Known connections between AMPK, mTORC1 and ERK, and corresponding reporters for live-cell analysis. ERKTR and TFEB-TR indicate the activities of ERK and mTORC1, respectively, by their cytoplasmic to nuclear ratio. B: Population average responses of AMPKAR2^{PHOS} (blue) compared to ERKTR (orange) and TFEB-TR (green) after oligomycin (OM, upper panels) or vehicle (lower panels) treatment. Shaded areas indicate interquartile ranges. N=2. C: Correlation of AMPKAR2Δ with signaling markers in single cells. Each dot indicates a single cell in which

AMPKAR2Δ was measured in tandem with (i) ERKTR (live-cell), (ii) phosphorylated ERK (IF), (iii) TFEB-TR (live-cell), or (iv) phosphorylated 4E-BP1. For live-cell measurements, values represent amplitude of response. For IF measurements, values represent integrated staining intensity for cells fixed immediately following measurement of AMPKAR2Δ. R^2 and p values are shown for linear regression against pooled data for both untreated and oligomycin-treated cells. N=2. D: Dynamic relationship of AMPK activity with (i) ERK and (ii) mTORC1 reporters. Representative single-cell profiles of AMKPAR2^{PHOS} were measured in the same cell as ERKTR (orange) or TFEB-TR (green). E: Cross-correlation analysis for AMPK activity with ERK and mTORC1 reporters. (i) and (iii) show distributions of the lag time at which maximum anti-correlation is found between AMPKAR2 and ERKTR or between AMPKAR2 and TFEB-TR, respectively. (ii) and (iv) show the distribution of Pearson's cross-correlation coefficients at the lag time with maximum correlation (0 minutes for ERKTR, -12 minutes for TFEB-TR). N=2.

3.3.3. AMPK responses to OXPHOS inhibition report the dynamics of ATP metabolism

Cell-to-cell variation in AMPKAR2Δ may reflect differences in cellular energy charge (Hardie, 2014), but this variation could also arise from variable drug uptake or other forms of AMPK regulation (Lin and Hardie, 2017; Zhang et al., 2017). To independently measure changes in energy charge, we used the ADP/ATP reporter PercevalHR (Berg et al., 2009; Tantama et al., 2013), which reports intracellular ADP/ATP ratio as a spectral shift in mVenus excitation, a ratio we refer to as Perceval^{EX} (Fig. 3.3.A). Similar to AMPKAR2^{PHOS}, the immediate response of Perceval^{EX} following OXPHOS inhibition was heterogeneous (Fig. 3.3.B,i). However, unlike AMPK activity, Perceval^{EX} lacked two distinct modes. Under continuous exposure to oligomycin, we observed pulses of Perceval^{EX} 1-2 hours in duration, interspaced by 2-4 hours, similar to AMPKAR2^{PHOS} in timing but more variable in amplitude. Staining of pACC was correlated with Perceval^{EX}, with agreement of pACC staining and Perceval^{EX} responses in ~80% of cells (Fig. 3.3.B,ii and S3.2.A). However, the distinction between high- and low-Perceval^{EX} cells was not sharp, and cells at intermediate Perceval^{EX} values were distributed between high- and low-pACC subpopulations, consistent with findings that factors other than energy charge can influence AMPK activity (Hawley et al., 2005; Zhang et al., 2017). Based on these data, differences in energy charge are a plausible cause for AMPK variation but are not strictly identical to AMPK activity within individual cells.

We next used the FRET-based ATP sensor ATeam 1.03 (Imamura et al., 2009) to track intracellular ATP concentrations under the same conditions. Following oligomycin treatment, we were unable to detect any change in ATP level, nor any pulsatile characteristics as observed for AMPKAR2^{PHOS} or Perceval^{EX} (Fig. 3.3.B,iii). To confirm that the lack of ATeam response is not a result of out-of-range ATP concentration, we treated these cells with oligomycin in the absence of glucose, which resulted in an immediate and sharp decline in ATeam signal (Fig. S3.2.C), followed within 4 hours by visible cell death. We confirmed this result using bulk ATP assays, which detected no OXPHOS inhibitor-induced change in ATP at 17 mM glucose but a >90% decrease upon inhibitor treatment in the absence of glucose (Fig. S3.2.D). When ATeam cells were co-stained with pACC, we observed that the rare low-ATeam cells (~10%) were predominantly pACC-positive, as expected for cells with low ATP (Fig. 3.3.B,iv and S3.2.B). These results indicate that ATeam accurately reports ATP levels within MCF10A, and that cytoplasmic ATP remains stable during OXPHOS inhibition, as previously observed (Gowans et al., 2013; Hao et al., 2010).

The differences between AMPK activity, ADP/ATP ratio, and ATP concentration prompted us to investigate their relationship. To approach this question, we quantified AMPKAR2^{PHOS}, Perceval^{EX}, or ATeam responses following oligomycin treatment under varying concentrations of glucose (Fig. 3.3.C-E). AMPKAR2^{PHOS} responses remained bimodal across all conditions, with the frequency of OP-ind cells decreasing from >20% of cells at 17 mM glucose (standard MCF10A culture conditions) to 8-9% at 4.25 mM glucose (an intermediate physiological concentration) and falling to <1% at lower glucose concentrations (Fig. 3.3.C). In contrast, Perceval^{EX} was distributed unimodally in each condition, with a mean that increased gradually as glucose concentration was lowered (Fig. 3.3.D). ATeam showed no response until glucose was reduced below 1 mM, at which point it showed a rapid decrease in all cells (Fig. 3.3.E). Together, these data suggest a model consistent with previous observations, in which the absolute cytosolic concentration of ATP is maintained at a nearly constant level, provided that glycolysis can operate at a sufficiently high

rate. Rapid equilibration of ATP with ADP and AMP prevents a large drop in absolute ATP levels but allows a significant shift in ADP/ATP and AMP/ATP ratios, which are detected by AMPK (Hardie et al., 2012). The gradually shifting broad distribution of Perceval^{EX} indicates that these ratios vary from cell to cell and are sufficient to induce AMPK activity in some cells (OP-dep) but not others (OP-ind). The bimodality observed in AMPK activity but not ADP/ATP ratio is consistent with ultrasensitive activation of AMPK (Hardie et al., 1999). Thus, the differing relationships between pACC, AMPKAR2, Perceval^{EX}, and ATeam can be understood as the outcome of the ATP/AMPK system as it operates in single cells that vary in their capacity to maintain ATP production when OXPHOS is inhibited.

The results above suggest that energy charge is the primary factor determining AMPK activity under OXPHOS inhibition. Bulk measurements of metabolites are consistent with this interpretation: oligomycin treatment induced strong and persistent suppression of TCA cycle intermediates (Fig. S3.2.E,F), while inference of ATP production (Mookerjee et al., 2017) confirmed a nearly complete switch from OXPHOS to glycolysis during oligomycin treatment (Fig. S3.2.G). Finally, comparison of OXPHOS inhibitor responses under different conditions argued that the lack of AMPK activity in OP-ind cells is not an artifact of incomplete OXPHOS inhibition (Fig. S3.3.A-G). We conclude that OP-ind cells represent a subpopulation with metabolic characteristics inherently distinct from OP-dep cells.

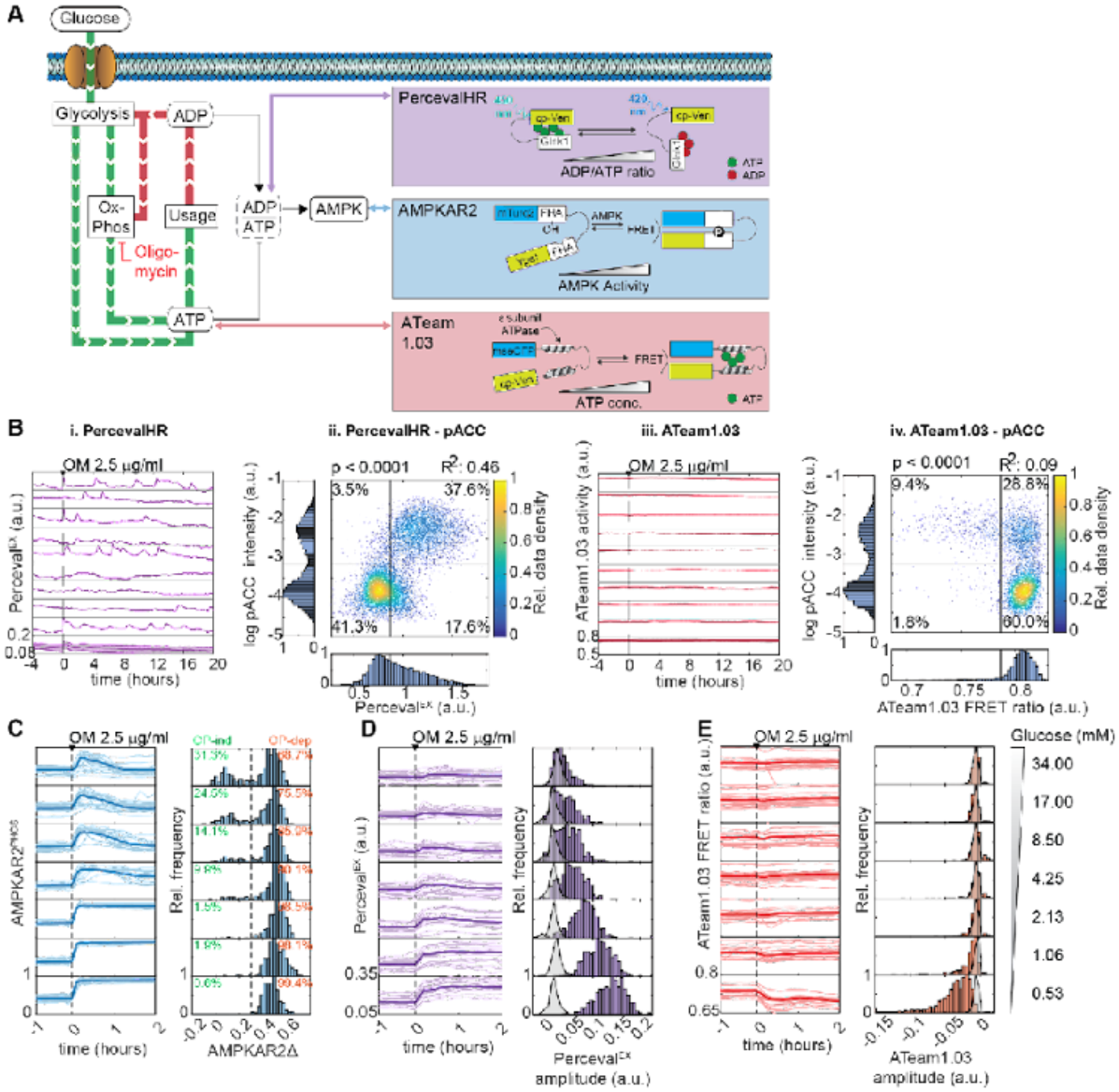

Figure 3.3 : AMPK responses to OXPHOS inhibition report the dynamics of ATP metabolism

A: Schematic of ATP metabolism and reporters used. AMPKAR2 indicates AMPK kinase activity, PercevalHR reports intracellular ADP/ATP ratio, and ATeam1.03 reports intracellular ATP concentration. B: Responses of ADP/ATP and ATP reporters to OXPHOS inhibition. (i) and (iii) show representative single-cell recordings of PercevalHR (i) or ATeam1.03 FRET activity (iii) after treatment with 2.5 µg/ml oligomycin. Each subplot represents a single cell measurement, with the population average and interquartile range shown at bottom. (ii) and (iv) show scatter plots of single-cell measurements of Perceval^{EX} (ii) or ATeam1.03 FRET activity (iv) with phospho-ACC staining intensity in MCF10A cells treated with oligomycin (OM) 2.5 µg/ml. Numbers indicate the percentage of cells in each quadrant. R^2 values are shown for linear fits to the data. N=2. C, D, and E: AMPK, ADP/ATP, and ATP responses to OXPHOS inhibition when glucose is varied. Line plots (left) show the responses for each reporter after cells were cultured in media containing the indicated glucose concentration and then treated with 2.5 µg/ml oligomycin (OM). Light lines

indicate individual cells, and heavy lines the population mean. Histograms (right) show the distribution of response amplitudes in each condition, calculated as in Figure 1. In (D) and (E), the light gray histograms indicate the distributions of reporter measurements for cells treated with vehicle at the same glucose concentration. N=2.

3.3.4. Resistance to OXPHOS inhibition is a heritable but transient state

Our results raise the question of whether OXPHOS inhibitor resistance is a fixed or transient cellular property, which we approached using sister cell analysis (Spencer et al., 2009; Strasen et al., 2018). We tracked the history of cells prior to OXPHOS inhibitor treatment and compared AMPKAR2Δ for sister cell pairs as a function of time since their last mitosis (Fig. 3.4.A). If resistance is a permanent characteristic, sister cells would remain similar in their response indefinitely (Fig. 3.4.A,i), whereas if resistance is transient, they will be similar initially but diverge over time (Fig. 3.4.A,ii). Both OP-ind and OP-dep cells were well represented at all times after the last division (Fig. 3.4.B,C), and sister cell pairs within 2 hours of their shared mitosis were significantly more likely to have a similar AMPKAR2Δ response than random pairs of cells (Fig. 3.4.D,E). However, this similarity in AMPKAR2Δ between daughters decayed gradually and approached the level of unrelated cells with a half-life of ~29 hours (Fig. 3.4.E). These results indicate that OP-ind or OP-dep states are a heritable property that can persist for at least several hours, and that transitions between these states occur intermittently within the cell population.

To observe transitions between sensitive and resistant states more directly, we performed long-term imaging of cells under continuous oligomycin treatment. Cells classified as OP-dep entered immediately into a regular oscillatory pattern of AMPK activity (as seen in Fig. 1A), with a period of approximately 3 hours (Fig. 3.4.F, top). However, we noted that cells occasionally exited this oscillatory state and entered a phase with weaker, irregular AMPK activity (Fig. 3.4.F, bottom and S4A). For cells that showed such a transition, the median time to transition ranged from 0 to 60 hours, with a median of 34 hours. Phases of weak AMPK activity persisted for 1-20 hours, with a median of 5.6 hours (Fig. 3.4.H), before cells returned to the oscillatory phase. Similarly, cells that initially showed an OP-ind response typically underwent a transition into

oscillatory activity within 6 hours after oligomycin treatment (Fig. 3.4.I). These results are consistent with the sister-cell analysis and indicate that cells transition intermittently between an OP-dep-like phase with oscillatory AMPK activity, and an OP-ind-like phase with weak AMPK activity. Furthermore, comparison of the duration and frequencies of these phases to the overall frequency of OP-ind cells suggests that the primary source of initial OP-ind cells are the intermittent phases of weak AMPK activity, rather than the 3-hour oscillatory nature of the AMPK response (Fig. S3.4.B).

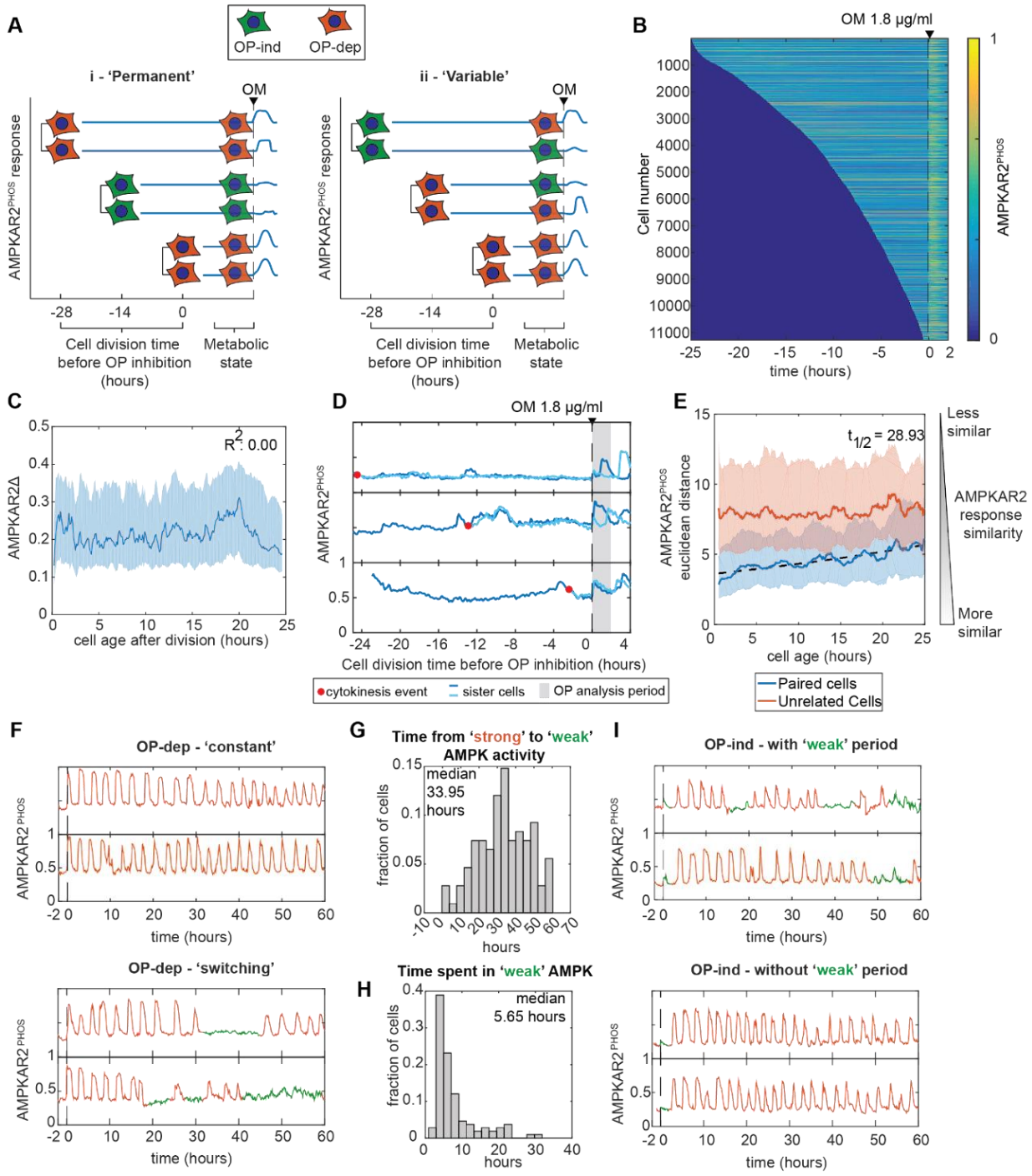

Figure 3.4 : OXPHOS inhibitor resistance is a heritable but transient cellular state

A: Schematic of sister cell analysis to distinguish between permanent and time-varying cell states determining the response to OXPHOS inhibition. B: Heatmaps of AMPKAR2^{PHOS} in individual cells. MCF10A-AMPKAR2 cells were imaged for 24 hours before treatment with 1.8 µg/ml oligomycin. Each horizontal line represents a single cell's AMPKAR2^{PHOS} profile, beginning with its most recent cell division and ending 2 hours after oligomycin (OM) treatment. Cells were sorted by the time of their last division. Analysis contains >11,000 individual cells. N=3. C: Line plot of

the relationship between a cell's age at the time of oligomycin treatment and its recorded AMPKAR2Δ response. D: Sample traces of AMPK activity from sister cell pairs. E: Comparison of AMPKAR2^{PHOS} responses in sister cells. Dissimilarity between the sisters of each division, or between randomly chosen pairs of cells was calculated (see Methods). Solid lines represent effect size, and the shaded areas represent interquartile range after bootstrapping. Dashed line represents a fitted exponential function for the decay of sister cell similarity over time. F: Transitions in OXPHOS dependence within single cells. Top panels show two example cells in which strong AMPK activity (continued pulsing) persists for the remainder of the experiment. Bottom panels show two example cells that transition from strong activity (orange) to a state with weak AMPK activity (green). N=2. G: Distribution of transition times from strong to weak AMPK activity. For all cells showing a transition as shown in the bottom panels of (F), the time between oligomycin treatment and the first transition is shown as a histogram. H: Distribution of durations of weak AMPK activity states. For all cells showing both entry into and exit from an OP-ind state during the experiment (green phases in (F)), the interval between entry and exit is shown as a histogram. I. Examples of cells transitioning from a weak to a strong AMPK state. Top panels show example cells that transition to strong and then return to weak activity. Bottom panels show instances of cells that transition to strong activity for the remainder of the experiment.

3.3.5. Glucose uptake and protein synthesis modulate OXPHOS inhibitor resistance

We next addressed the molecular differences that underlie OP-dep and OP-ind responses, beginning with the capacity to produce ATP by glycolysis. Treatment with insulin, which stimulates glucose uptake and glycolysis through PI3K/AKT signaling, increased the frequency of OP-ind responses in MCF10A, MCF7, 184A1, and U87MG cells (Fig. 3.5.A). Furthermore, inhibition of AKT, hexokinase, or mTORC1/2 shifted cells toward OP-dep responses (Fig. 3.5.B). In contrast, inhibition of fatty acid oxidation or lipolysis failed to significantly alter OP-ind responses (Fig. S3.5.A). While these results implicate regulation of glucose uptake through insulin/PI3K/AKT signaling, this pathway can potentially affect AMPK activation through multiple routes (Suzuki et al., 2013). To test whether OP-ind cells can result solely from increased glucose uptake capacity, we overexpressed the glucose transporter GLUT1 along with a co-translated red fluorescent protein (RFP) to quantify GLUT1 overexpression on a cell-by-cell basis. We removed insulin to eliminate the AKT-induced component of glucose uptake. Higher expression GLUT1-RFP correlated with weaker AMPK responses to OXPHOS inhibitor (Fig. 3.5.C), with 60% of GLUT1-RFP-expressing cells showing OP-ind behavior, while almost 100% of cells not expressing GLUT1-RFP were OP-dep. When insulin was added, OP-ind responses shifted to

include cells at lower GLUT1-RFP expression levels, consistent with the induction of endogenous (unlabeled) glucose transporters (Fig. 3.5.D,E). Accordingly, the predictability of OXPHOS inhibitor response as a function of exogenous GLUT1 expression decayed (Fig. 3.5.C-E, bottom panels). These data demonstrate that a cell's OXPHOS inhibitor resistance status can be determined by its capacity to take up glucose, and that this status can be predicted based on glucose transporter expression when other factors are minimized.

Most cell lines are cultured in media containing high levels of glucose, and therefore OP-ind responses might result from glucose-induced changes in glycolytic gene expression or from increased storage metabolites (such as glycogen). To test these possibilities, we cultured cells in the absence of glucose for 24 hours, and then added glucose for a short time window (30 minutes or 1 minute) prior to treating with oligomycin (Fig. 3.5.F). Because short exposure to glucose is unlikely to increase storage pools or expression of glycolytic enzymes, we expected that OP-ind cells relying on these mechanisms would become OP-dep during the starvation period. However, OP-ind cells were instead detected at a much *higher* frequency following glucose withdrawal (>90% at 17 mM glucose, Fig. 3.5.G) than when cultured in glucose continuously (~25% at 17 mM glucose, see Fig. 3C). This result indicates that OP-ind cells are not simply the result of prolonged high glucose conditions. Rather, it may be that during the starvation period, ATP consumption rates decline more than glycolytic capacity, resulting in anabolically inactive cells that have relatively low demand but remain poised to utilize glucose when it is resupplied (Fig. S3.5.B). Consistent with this interpretation, protein synthesis rate as measured by O-propargyl puromycin (OPP) incorporation was significantly lower following 24 hour glucose starvation (Fig. S3.5.C). At the same time, the frequency of OP-ind cells remained dependent on the concentration of glucose that was resupplied for 1 minute (Fig. 3.5.G). Thus, these results support that glycolytic capacity is needed for OP-ind responses and implicate ATP turnover as a potential additional factor that influences the OXPHOS inhibitor response. We also found that glutamine,

which is provided in excess in some cell culture media, is not required for OP-ind responses but can increase their frequency (Fig. S3.5.D).

Because our results and previous studies (Buttgereit and Brand, 1995) suggest that ATP usage (i.e., turnover) by protein synthesis may impact energy charge upon OXPHOS inhibition, we tested the effect of translation inhibition by cycloheximide (CHX) using both OPP incorporation and a live-cell translation reporter, TOP-H2B-YFP-DD (Han et al., 2014)(Fig. 3.6.A-C). Pre-treatment with CHX decreased the fraction of OP-dep cells from 60% to <10% (Fig. 3.6.D). Furthermore, even 15 minutes after an AMPK response was initiated, protein synthesis inhibitors immediately reduced AMPK activity, shortening the pulse length from 60 minutes to 20 minutes (Figure 6E, F). This observation suggests that reducing ATP consumption by translation lowers the impact of OXPHOS inhibitors on energy charge and AMPK activation.

Several observations supported the interpretation that inhibitors of translation limit AMPK activity due to a decrease in catabolic activity, rather than activation of feedback or stress responses. First, while extended incubation with CHX increased phosphorylation of S6 and 4E-BP1 as previously reported (Santos et al., 2019), this increase was moderate relative to the pre-existing mTORC1 activity level (Fig. S6D,E). Furthermore, culture of cells in varying concentrations of essential amino acids (EAA) or non-essential amino acids (NEAA) modulated the rate of protein synthesis as measured by TOP-H2B-YFP-DD (Fig. 3.6.G,H). Under these conditions, the fraction of OP-dep cells measured following oligomycin treatment correlated with the protein synthesis rate (R^2 =0.53, Fig. 3.6.I). These results support that OP-ind cells depend on a low rate of protein synthesis, which makes it possible for glycolysis to maintain cellular energy charge above the threshold to trigger AMPK.

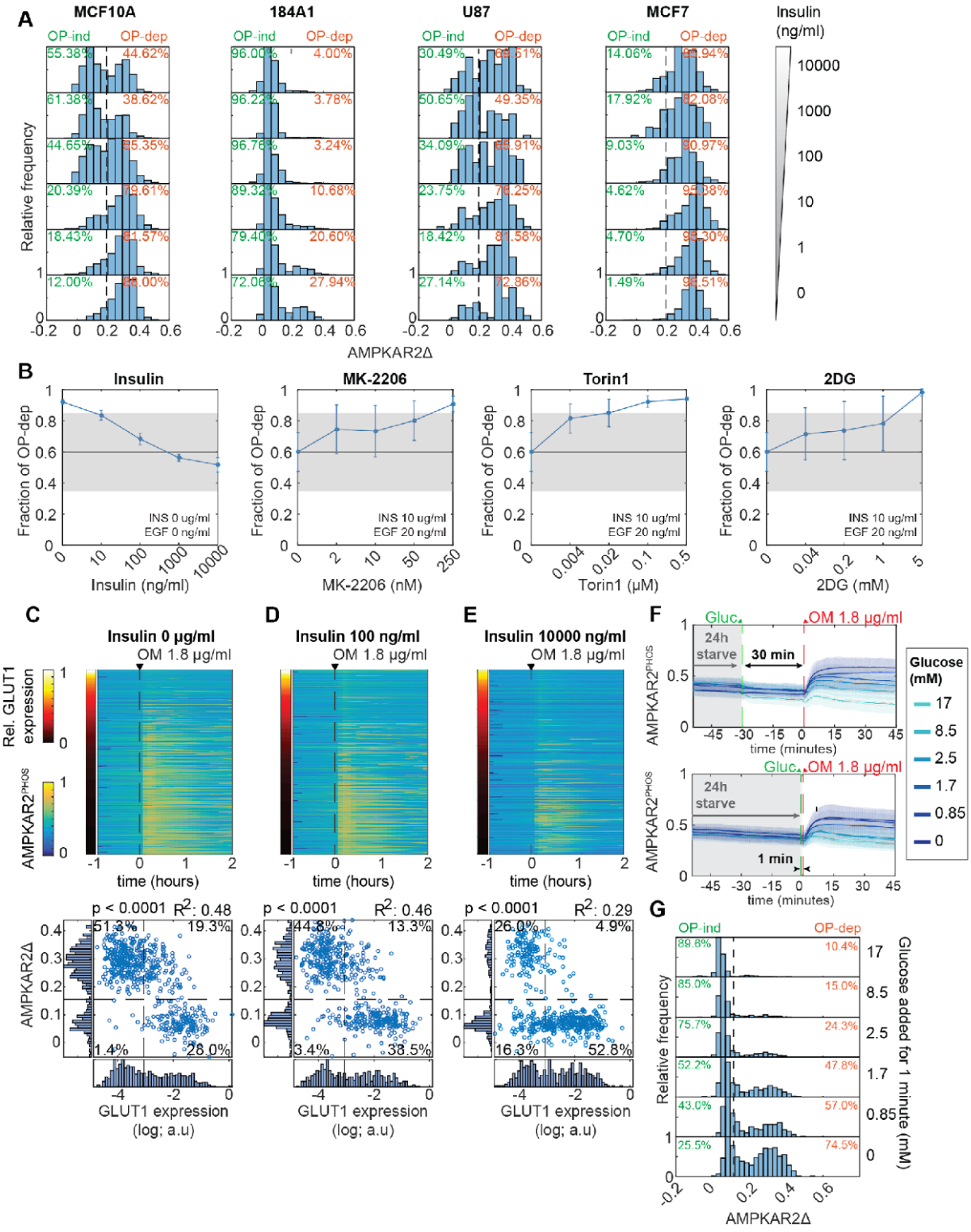
A
MCF10A
184A1
U87
MCF7
OP-ind
OP-dep
Relative frequency
AMPKAR2Δ
Insulin (ng/ml)
10000
1000
100
10
1
0
B
Insulin
MK-2206
Torin1
2DG
Fraction of OP-dep
INS 0 ug/ml
EGF 0 ng/ml
INS 10 ug/ml
EGF 20 ng/ml
Insulin (ng/ml)
MK-2206 (nM)
Torin1 (μM)
2DG (mM)
C
Insulin 0 μg/ml
D
Insulin 100 ng/ml
E
Insulin 10000 ng/ml
OM 1.8 μg/ml
Rel. GLUT1 expression
AMPKAR2PHOS
time (hours)
p < 0.0001 R2: 0.48
p < 0.0001 R2: 0.46
p < 0.0001 R2: 0.29
AMPKAR2Δ
GLUT1 expression (log; a.u)
F
Gluc
OM 1.8 μg/ml
24h starve
30 min
1 min
time (minutes)
Glucose (mM)
17
8.5
2.5
1.7
0.85
0
G
OP-ind
OP-dep
Relative frequency
AMPKAR2Δ
Glucose added for 1 minute (mM)

Figure 3.5 : Glucose uptake and protein synthesis modulate OXPHOS inhibitor resistance

A: Increase in OP-ind responses stimulated by insulin. Histograms show AMPKAR2Δ responses to 1.8 µg/ml oligomycin. N=2. B: Change in OP-dep responses in response to inhibitor treatment for MCF10A cells under 17 mM glucose. Inhibitors were added 30 minutes prior to oligomycin. Horizontal black lines indicate the fraction of OP-dep cells under control treatment (DMSO); points falling outside the gray region are considered significant by t-test. Points represent the mean, and error bars standard error of the mean; N=2. C, D and E: Effect of increased glucose uptake on OXPHOS inhibitor responses. MCF10A-AMPKAR2 cells stably overexpressing GLUT1-IRES-NLS-mCherry were cultured with 0 (C), 100 (D), or 10000 ng/ml (E) insulin and exposed to oligomycin (OM). Each row in the heatmaps (upper panels) represents an individual cell; rows are sorted by relative mCherry intensity (corresponding to the level of GLUT1 overexpression), which is indicated by the color bar to the left. GLUT1 expression levels are normalized to the minimum and maximum expression levels in the population. Lower panels show scatter plots of mCherry intensity and AMPKAR2Δ following oligomycin treatment. N=2. F, G: Increase in OP-ind responses following glucose starvation. (F) shows average AMPKAR2^{PHOS} recordings for MCF10A cells grown in the absence of glucose for 24 hours and then treated with glucose at the specified concentrations, followed by 1.8 µg/ml oligomycin at 30 minutes or 1 minute after glucose addition. (G) shows histograms of AMPKAR2Δ values after oligomycin treatment for the conditions shown in (F). N=2.

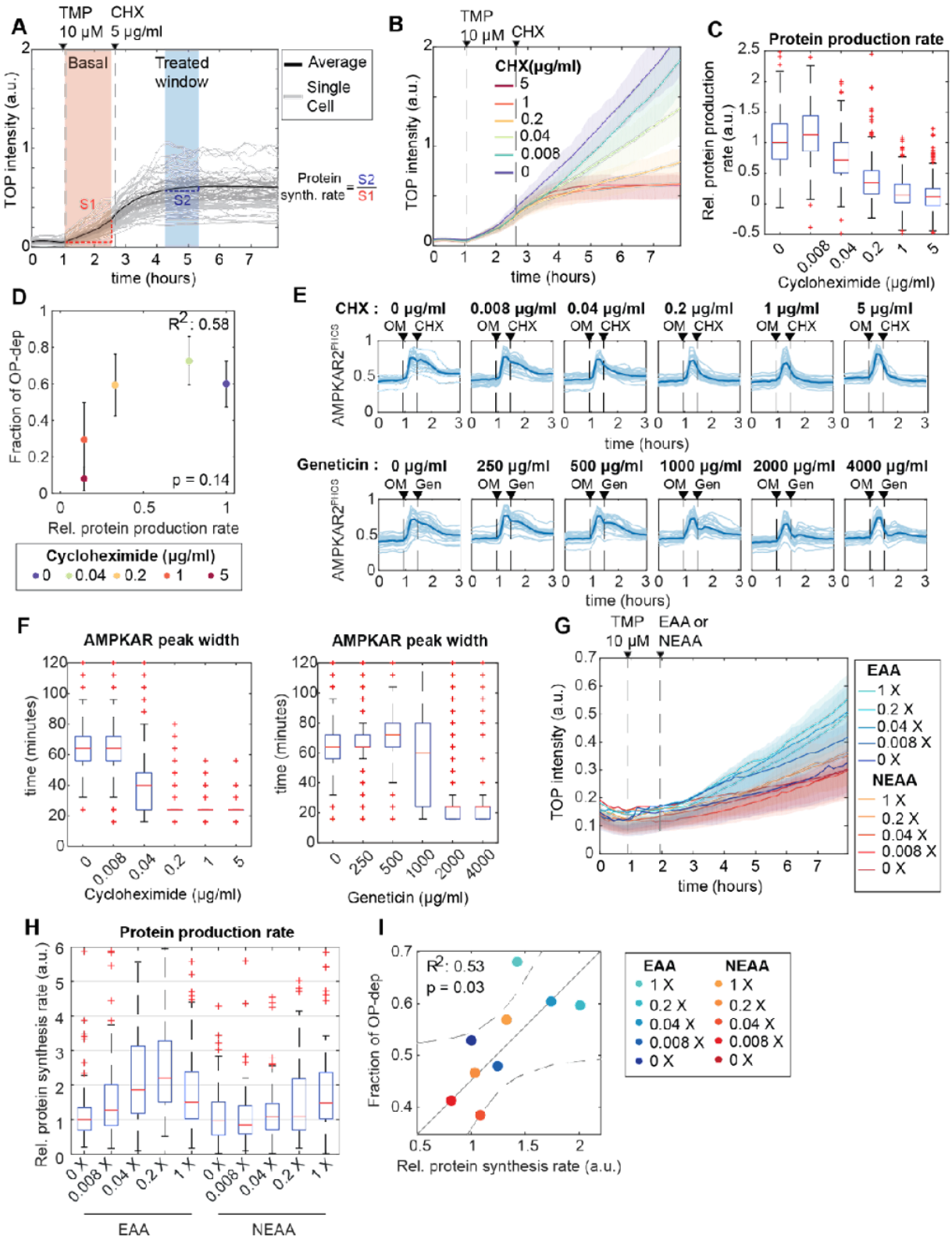
A
TMP 10 µM
CHX 5 µg/ml
Basal
Treated window
Average
Single Cell
TOP intensity (a.u.)
time (hours)
S1
S2
Protein synth. rate = S2/S1
B
TMP 10 µM
CHX
CHX(µg/ml)
5
1
0.2
0.04
0.008
0
TOP intensity (a.u.)
time (hours)
C
Protein production rate
Rel. protein production rate (a.u.)
Cycloheximide (µg/ml)
D
R2: 0.58
p = 0.14
Fraction of OP-dep
Rel. protein production rate
Cycloheximide (µg/ml)
0 0.04 0.2 1 5
E
CHX : 0 µg/ml 0.008 µg/ml 0.04 µg/ml 0.2 µg/ml 1 µg/ml 5 µg/ml
OM CHX
AMPKAR2PHOS
time (hours)
Geneticin : 0 µg/ml 250 µg/ml 500 µg/ml 1000 µg/ml 2000 µg/ml 4000 µg/ml
OM Gen
AMPKAR2PHOS
time (hours)
F
AMPKAR peak width
time (minutes)
Cycloheximide (µg/ml)
AMPKAR peak width
time (minutes)
Geneticin (µg/ml)
G
TMP 10 µM
EAA or NEAA
TOP intensity (a.u.)
time (hours)
EAA
1 X
0.2 X
0.04 X
0.008 X
0 X
NEAA
1 X
0.2 X
0.04 X
0.008 X
0 X
H
Protein production rate
Rel. protein synthesis rate (a.u.)
EAA
NEAA
I
R2: 0.53
p = 0.03
Fraction of OP-dep
Rel. protein synthesis rate (a.u.)
EAA
1 X
0.2 X
0.04 X
0.008 X
0 X
NEAA
1 X
0.2 X
0.04 X
0.008 X
0 X

Figure 3.6 : Reducing protein synthesis rate promotes OXPHOS inhibitor resistance

A: Measurement of protein synthesis rates in live cells. MCF10A cells stably expressing TOP-H2B-YFP-DD (TOP) were treated with the degron inhibitor trimethoprim (TMP). Protein production rate was calculated as the slope of YFP intensity change during the 60 minutes after TMP treatment (orange shaded area). The effect of CHX inhibition on protein production was quantified from the slope for a 60 minute period beginning 90 minutes after treatment (blue shaded area); relative protein production rate is calculated as the ratio of slopes in the blue and orange regions (S1 and S2 respectively). B, C: Quantification of reduced protein synthesis rates. (B) shows mean TOP-H2B-YFP-DD intensity for a concentration series of CHX treatments. Shaded areas show interquartile ranges. (C) shows calculated single-cell relative protein production rates for each concentration of cycloheximide. Each box represents the distribution of >400 cells. N=2. D: Relationship of average protein production rate to the fraction of OP-dep cells. Protein rate was measured as in (A-C). The corresponding fraction of OP-dep responses was determined by culturing cells in the same CHX concentrations, followed by oligomycin treatment. Points represent the mean, and error bars standard error of the mean; N=2. E, F: Termination of AMPK activity pulses by protein synthesis inhibition. (E) shows single-cell traces (light lines) and means (dark lines) for cells treated with oligomycin (OM), followed by the protein synthesis inhibitors CHX or geneticin (Gen) at the concentrations indicated. (F) shows quantification of single cell AMPKAR2^{PHOS} pulse widths after CHX (left panel) or geneticin (right panel) treatment. Pulse widths were calculated as the time at which AMPKAR^{PHOS} decreased to 50% of the maximum value for each cell following treatment with CHX or geneticin. N=2. G-I: Modulation of protein synthesis and AMPK responses by amino acid availability. (G) shows representative mean TOP-H2B-YFP-DD intensity for MCF10A cells cultured in essential or non-essential amino acid at the indicated concentrations (X represents fold-change relative to the concentration in MEM). Shaded areas show interquartile ranges. (H) shows quantification of relative protein synthesis rates from the experiment shown in (G). Each box represents the distribution of >200 cells. (I) shows the mean protein synthesis rates from (G) plotted against the corresponding fraction of OP-dep cells, measured after oligomycin treatment in the same amino acid concentrations. Solid line represents a fitted linear model, and dashed lines the 95% confidence bounds. N=2.

3.3.6. OXPHOS inhibitor response states are inherently multivariate

We investigated the cell division cycle as a potential source of variability, combining AMPKAR2 measurements with DNA content, a live-cell S/G2 reporter (mCherry-Geminin$^{1-330}$), and staining for phosphorylated Rb protein (pRb). Plotting these measurements enabled cell cycle phases to be clearly distinguished (Fig. 3.7.A). We then overlaid the oligomycin-induced AMPKAR2Δ measurement for each cell, recorded immediately prior to fixation (Fig. 3.7.B). We noted that both high and low AMPKAR2Δ measurements were found in all stages of the cell cycle (Fig. 3.7.C,D). However, comparisons of the cell cycle phase distributions of OP-dep and OP-ind

cells revealed enrichment for different phases – OP-ind cells were 2-fold more likely to be in G1 phase relative to OP-dep cells, whereas OP-dep cells were more often found in S and G2 phases (Fig. 3.7.E). We noted that OPP incorporation increased with progression of the cell cycle (Fig. S3.7.A), providing a potential explanation for the higher number of OP-dep cells in S and G2. Live-cell recordings in cells expressing both AMPKAR2 and mCherry-Geminin$^{1-330}$ and treated with oligomycin identified OP-ind phases immediately following cell division (Fig. 3.7.F, top panel), consistent with their statistical enrichment in G0/G1. However, other cells showed continuous OP-dep responses in G0/G1 (Fig. 3.7.F, bottom panel), indicating that OP-ind responses are probabilistically related to cell cycle position, but not strictly determined by it.

To understand how multiple factors interact to determine OXPHOS inhibitor responses within individual cells, we performed a multivariate analysis using partial least squares regression (PLSR). We collected a multiplexed dataset for AMPKAR2Δ, OPP incorporation, cell cycle markers (Hoechst-33342 and pRb) and our GLUT1-RFP expression system as a surrogate measurement for glycolytic rate. We used Wanderlust (Bendall et al., 2014) to represent cell cycle position as a single continuous variable cycle based on DNA content and pRb measurements (Fig. S3.7.D). PLSR models were generated to predict each cell's AMPK response based on its individual combination of the other factors. Initially, we excluded cells with the highest GLUT1-RFP expression (Fig. S3.7.E) to prevent them from dominating the model predictions. In the best fitting models, the first principal component (PC) captured approximately 8% of variability in AMPK response between single cells, which was increased to 10% by the second PC; additional PCs did not further improve predictivity (Fig. 3.7.G and S7F). This relatively low predictive power is not unusual for single-cell models of signaling responses (Gillies et al., 2017) and indicates that unmeasured factors or stochastic variation contribute substantially to the variable AMPK response. Nonetheless, the variability captured by the model represents a strong signal relative to control models (Fig. 3.7.G, gray line) that can be used to understand the interactions between

measured variables. In the first PC, GLUT1-RFP was the highest weighted input and contributed negatively to AMPK response, while pRB and OPP incorporation had smaller positive contributions (Fig. 3.7.I). Individually, GLUT1, OPP, and pRB predicted 6.9%, 2.4%, and 1.8% of AMPK variability, while the inferred cell cycle position was less predictive than pRb (Fig. 3.7.H). As expected, when all levels of GLUT1-RFP expression were considered, overall predictivity rose to 35% (Fig. S3.7.E,F) but was dominated by the contribution of GLUT1-RFP (Fig. S3.7.G). Overall, this analysis demonstrates that each cell's OXPHOS inhibitor response is a multivariate process determined by a combination of glycolytic rate, protein synthesis, and RB phosphorylation, as well as other unmeasured parameters.

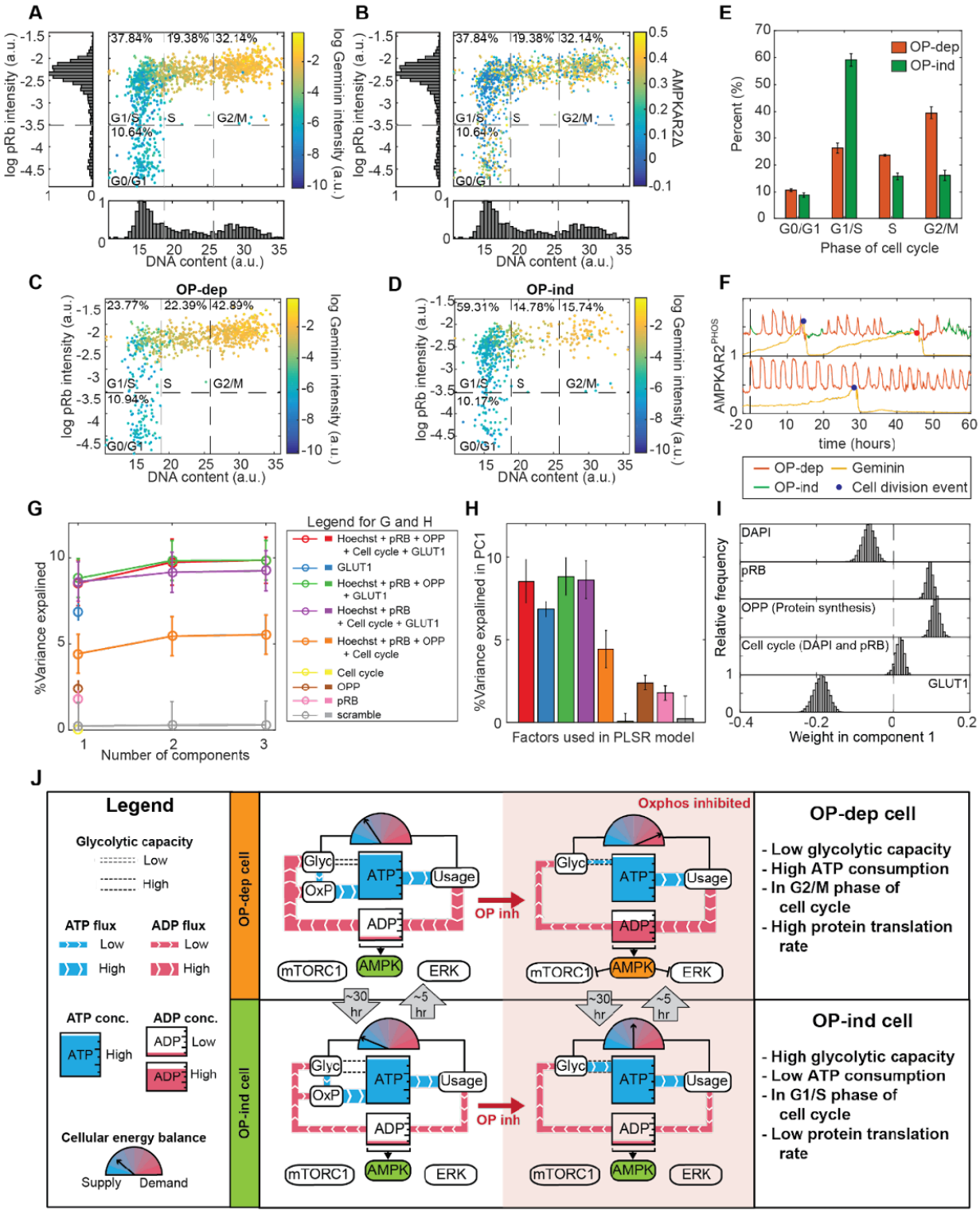
A
B
C
D
E
F
G
H
I
J
log pRb intensity (a.u.)
log Geminin intensity (a.u.)
AMPKAR2Δ
DNA content (a.u.)
37.84%
19.38%
32.14%
10.64%
G1/S
S
G2/M
G0/G1
OP-dep
OP-ind
23.77%
22.39%
42.89%
10.94%
59.31%
14.78%
15.74%
10.17%
Percent (%)
Phase of cell cycle
AMPKAR2PHOS
time (hours)
OP-dep
OP-ind
Geminin
Cell division event
%Variance expalined
Number of components
Legend for G and H
Hoechst + pRB + OPP + Cell cycle + GLUT1
GLUT1
Hoechst + pRB + OPP + GLUT1
Hoechst + pRB + Cell cycle + GLUT1
Hoechst + pRB + OPP + Cell cycle
Cell cycle
OPP
pRB
scramble
%Variance expalined in PC1
Factors used in PLSR model
Relative frequency
DAPI
pRB
OPP (Protein synthesis)
Cell cycle (DAPI and pRB)
GLUT1
Weight in component 1
Legend
Glycolytic capacity
Low
High
ATP flux
ADP flux
ATP conc.
ADP conc.
Cellular energy balance
Supply
Demand
OP-dep cell
OP-ind cell
Oxphos inhibited
OP inh
Glyc
OxP
ATP
ADP
Usage
mTORC1
AMPK
ERK
~30 hr
~5 hr
OP-dep cell
- Low glycolytic capacity
- High ATP consumption
- In G2/M phase of cell cycle
- High protein translation rate
OP-ind cell
- High glycolytic capacity
- Low ATP consumption
- In G1/S phase of cell cycle
- Low protein translation rate

Figure 3.7 : OXPHOS inhibitor response states are inherently multivariate

A: Scatter plot of single cell measurements of DNA content (Hoechst 33342 intensity) and phospho-Rb IF, colored by mCherry-Geminin$^{1-330}$ intensity. Dotted lines divide the phases of the cell division cycle, with the percentage of cells in each phase indicated. N=3. B: Scatter plot of cell cycle parameters as in (A), colored by AMPKAR2Δ values recorded during the 30 minutes immediately prior to fixation and staining. N=3. C and D: Scatter plots of cell cycle parameters as in (A), divided between OP-dep cells (C) and OP-ind cells (D). N=3. E: Bar graph comparing the distribution of cell cycle phases for OP-ind and OP-dep cells. Error bars represent standard errors of means; N=3. F: Single cell traces of AMPK activity and mCherry-Geminin$^{1-330}$ intensity for (top) a cell in which OP-ind occurs early in G0/G1, and (bottom) a cell in which no OP-ind phase occurs during G0/G1. Markers indicate the time of mitosis. G: Predictivity of PLSR models of AMPKAR2Δ (percentage of total variance explained) including the indicated combinations of measurements. For the ‘‘scrambled’’ model, pairings between input and output measurements for each cell were randomly reassigned. Cell cycle position was estimated by using the Wanderlust algorithm for non-linear mapping. See STAR Methods and Figure S7D for details. H: Bar chart showing percent of total variance explained by the first PLSR component for models using combinations of cellular processes measurement as indicated. I: Contribution of measured processes to PLSR models for AMPKAR2^{PHOS} response to oligomycin treatment. Distributions of parameter coefficients were generated by bootstrapping with replacement 10,000 times. J: Simplified diagrams indicate the state of ATP metabolism in OP-ind and OP-dep cells. Blue “pipes” indicate flux of ATP, and red pipes the flux of ADP. Meter icons indicate the balance of ATP production capacity relative to ATP consumption. The dotted ‘pipe’ indicates reserve glycolytic capacity to supply ATP. OP-dep cells (top panel) have low glycolytic capacity with high ATP demand; upon OXPHOS inhibition, these cells maintain constant ATP concentration at the expense of an increase in ADP that triggers activation of AMPK and inhibition mTORC1 and ERK pathways. OP-ind cells (bottom panel) have high reserve glycolytic capacity and relatively low ATP demand. Upon OXPHOS inhibition, these cells can maintain constant ATP and a low concentration of ADP via glycolysis, and AMPK consequently remains inactive.

3.4. Discussion

Cellular heterogeneity can influence the therapeutic efficacy of drugs (Altschuler and Wu, 2010). We identify a distinct form of heterogeneity that results from transient differences in each cell's balance between the capacity to generate ATP through glycolysis and its ATP consumption or turnover rate. While protein synthesis, glucose uptake, and the cell cycle are well-known to affect cellular energy balance, our analysis reveals that these processes interact at the cellular level to create transient states of resistance to an acute metabolic challenge like OXPHOS inhibitor treatment. This variation impacts metabolic stress signaling through AMPK, mTOR, and ERK, which are among the intended targets for OXPHOS inhibition in both cancer and diabetes (Howell et al., 2017; Kim et al., 2012).

Our data indicate that the response to OXPHOS inhibition depends on multiple factors and is difficult to predict for any individual cell. Each cell carries on its own mixture of ATP-consuming processes, and at the same time has a certain maximal capacity for ATP production through glycolysis. The net balance of these processes determines the extent to which ATP production can continue when OXPHOS is inhibited (Fig. 7J). Therefore, while protein synthesis and AKT signaling are significant drivers of the OXPHOS response, for a specific cell they may not be the most consequential, depending on which other ATP-consuming or generating processes are active. Furthermore, our data suggest that as the prevalence of these processes changes over time in a given cell, so does its OXPHOS inhibition response. Only when components such as GLUT1 are overexpressed can a cell's response be predicted reliably based on a single factor. This complexity makes the OXPHOS inhibitor response useful, as it can interrogate the net ATP production/turnover balance in a single measurement.

How does cellular variation in ATP turnover and production arise? While OP-dep and OP-ind responses correlate to some extent with cell cycle phases, this bias cannot explain most variation, as both types of response can be found at any point in the cell cycle. We suggest that,

because protein synthesis increases throughout the cell cycle (Elliott and McLaughlin, 1978), ATP turnover increases and OP-dep states become increasingly likely during S and G2, explaining their observed enrichment in these phases. Can the remaining variability then be attributed to different rates of glucose uptake? This is possible, as we have observed that AMPK and AKT activity can fluctuate during normal growth conditions (Hung et al., 2017), which would be expected to result in different glucose uptake rates over time. Still another possibility is that, as in yeast (Cai and Tu, 2012; Tu et al., 2007) mammalian cells have an intrinsic cycle that controls flux through glycolysis and protein synthesis. Our results reveal the existence of at least two different but interrelated cellular rhythms: a regular oscillation between AMPK activity and inactivity with a period of ~3 hours during OXPHOS inhibition, and a longer-term shift between a state in which cells are competent for AMPK oscillations and a state in which AMPK activity remains dormant. The longer cycle, on the order of 20-30 hours, could be linked to the mammalian cell division cycle (Ahn et al., 2017) or circadian rhythms (Bass and Takahashi, 2010). However, it is less clear whether the shorter cycles have any relationship to the yeast metabolic cycle, which has a period of 2-3 hours but is closely linked to the cell cycle.

Our data reiterate the remarkable adaptability of ATP homeostasis that has previously been reported (Gowans et al., 2013; Hao et al., 2010). The stability of ATP concentration under severe perturbation of ATP production by OXPHOS inhibitor implies that a large fraction of ATP production can be shifted to glycolysis within seconds, despite its low yield of 2 ATP per glucose molecule relative to the ~30 produced by OXPHOS. Because ATP homeostasis is maintained even in cells without a detectable AMPK response (OP-ind), AMPK is likely not required for this initial adaptation. Rather, our data imply that during OXPHOS inhibitor treatment, flux through glycolysis is redirected from the production of biosynthetic intermediates, which are uncoupled from ATP production (Lunt and Vander Heiden, 2011), to prioritize the production of ATP. In OP-ind cells, the ATP consumption load is low enough that this shift can occur without a large

perturbation of ADP/ATP ratio, precluding activation of AMPK. In OP-dep cells, this shift is sufficiently rapid to preserve ATP levels, but generates a large enough rise in ADP/ATP ratio to cross the ultrasensitive threshold for AMPK activation (Hardie et al., 1999). AMPK likely plays a longer-term role in metabolic adaptation, consistent with the finding that it is required for mammalian development (Viollet and Foretz, 2016) but not for cellular viability (O'Neill et al., 2011).

Recently developed pharmacological AMPK activators (Cokorinos et al., 2017; Myers et al., 2017) and OXPHOS inhibitors (Molina et al., 2018; Shi et al., 2019) are expected to be useful in the treatment of cancer, diabetes, and inflammatory conditions. Understanding the factors that underlie the heterogeneous OXPHOS inhibitor response will be important in optimizing this growing class of pharmacological compounds. The ability to predict and control the fraction of cells that respond to OXPHOS inhibitors may allow these drugs to be tailored toward different goals. Potent induction of energy stress in the largest number of cells possible may be desirable in the case of anti-cancer therapy, but heterogeneous activation may be preferable when trying to restore physiological energy balance in diabetes or metabolic syndrome. Measuring metabolic heterogeneity may also be important for predicting responses to other drugs, such as cytotoxic chemotherapies. Our study opens a new window into how cellular heterogeneity in drug responses can arise from underlying metabolic differences between cells.

3.5. Limitations of Study

This study relies on immortalized cell lines, which carry genetic abnormalities, and which are cultured in medium that does not correspond to physiological conditions. Thus, this study does not bear on whether the heterogeneity we observe occurs within the human body. While we identify factors that alter or predict heterogeneous metabolic behavior, our study does not identify the underlying process that creates alternating periods of OXPHOS inhibitor sensitivity or specify the nature of this process. Changes in gene expression profile could underlie shifts in sensitivity,

but it is equally possible that post-translational modifications of proteins, or changes in metabolic pathway flux generate the observed variation; further work will be needed to distinguish these possibilities. Finally, our conclusions rely heavily on live-cell reporters of cellular metabolites or kinase activity, and though we provide validation of reporter data using alternate methods, we cannot exclude the possibility that the reporters show some cross-reactivity to additional factors in the cell.

3.6. Acknowledgements

Funding for this work was provided by the American Cancer Society (IRG-95-125-13), the National Institute of General Medical Sciences (1R01GM115650), and the American Association for Cancer Research/Stand Up To Cancer (SU2C-AACR-IRG-01-16). Stand Up To Cancer is a program of the Entertainment Industry Foundation. Research grants are administered by the American Association for Cancer Research, the scientific partner of SU2C. Flow-cytometry services were supported by the UC Davis Comprehensive Cancer Center Support Grant (CCSG) awarded by the National Cancer Institute (NCI P30CA093373). Metabolomics were performed in collaboration with West Coast Metabolomics Center at UC Davis. TOP-H2B-YFP-DD was kindly provided by Tobias Meyer. Seahorse assays were performed with the assistance of Gino Cortopassi, UC Davis School of Veterinary Medicine. We thank Marek Kochanczyk, Ben Tu, Ralph DeBerardinis, Joshua Rabinowitz, Sabrina Spencer, Isaac Harris, and Jon Coloff for helpful discussions.

3.7. Methods

3.7.1. Cell culture and media

Routine cell culture for human mammary epithelial cells, MCF10A clone 5E (Janes et al., 2010) and 184A cells were performed as previously described (Debnath et al., 2003). MCF10A and 184A1 were grown in ‘DMEM/F12 growth medium’ (see Media table). Primary stocks from the original clonal derivation (MCF10A-5E) or the ATCC (184A1) were used in all experiments.

MCF7, U87, and A549 cell lines were obtained from ATCC and cultured in ‘DMEM growth medium’ (see Media composition). All cells were routinely split when they are ~80% confluent.

In live microscopy experiments, we used a custom formulation, termed ‘imaging base-DMEM/F12’, which consists of DMEM/F12 lacking glucose, glutamine, riboflavin, folic acid, and phenol red (Life Technologies or UC Davis Veterinary Medicine Biological Media Service) which allows adjustment of available nutrients and avoids fluorescence background. All experiments involving MCF10A or 184A1 cell line were performed in ‘Imaging medium 1’ (see Media composition). ‘Imaging medium 1 – noAA’ was used in experiments that involved amino acid perturbation. For experiments with MCF7, U87 or A549 cell lines, ‘Imaging medium 2’ was used. For all experiments, ‘Imaging medium 1’, ‘Imaging medium 1 – noAA’ and ‘Imaging medium 2’ were supplied with glucose 17 mM and 25 mM, respectively, unless indicated otherwise.

Before imaging, cells were washed twice with their respective media and then cultured in imaging experiment media at least 2 hours prior to imaging, unless indicated otherwise. The cell to media ratio was maintained at 150-200 cells/µl for all experiments. For experiments involving titration of insulin or EGF concentrations, cells were placed in EGF- or insulin-deficient media for 4 – 6 hours prior to imaging.

3.7.2. Media composition

DMEM/F12 growth media

Component	Vendor	Catalog number	Final Concentration
DMEM/F2	Gibco	11320-033	-
Horse Serum	Invitrogen	16050-122	5%
EGF	Peprotech	AF-100-15	20 ng/ml
Hydrocortisone	Sigma	H0888	0.5 mg/ml
Cholera toxin	Sigma	C8052	100 ng/ml
Insulin	Sigma	I9278	10 ug/ml

DMEM growth medium

Component	Vendor	Catalog number	Final Concentration
DMEM	Gibco	11965-092	-
Fetal bovine serum	Gemini bio products	100-106	10%

Imaging medium 1

Component	Vendor	Catalog number	Final Concentration
Imaging base-DMEM/F12	Gibco	Custom; equivalent to Gibco 11320-033 lacking glucose, glutamine, pyruvate, riboflavin, folic acid, and phenol red	-
D-glucose	Fisher	D16	17 mM
BSA	Invitrogen	16050-122	0.1% w/v
Hydrocortisone	Sigma	H0888	0.5 mg/ml
Cholera toxin	Sigma	C8052	100 ng/ml
Penicillin-Streptomycin	Gibco	15140122	100 U/ml
EGF	Peprotech	AF-100-15	20 ng/ml
Insulin	Sigma	I9278	10 ug/ml

Imaging medium 2

Component	Vendor	Catalog number	Final Concentration
Imaging base-DMEM/F12	Gibco	Custom; equivalent to Gibco 11320-033 lacking glucose, glutamine, pyruvate, riboflavin, folic acid, and phenol red	-
D-glucose	Fisher	D16	25 mM
BSA	Invitrogen	16050-122	0.1% w/v
Penicillin-Streptomycin	Gibco	15140122	100 U/ml

Imaging medium 1 - noAA

Component	Vendor	Catalog number	Final Concentration
Imaging base-DMEM/F12-noAA	Gibco	Custom; equivalent to Gibco 11320-033 lacking glucose, glutamine, amino acids, pyruvate, riboflavin, folic acid, and phenol red	-
D-glucose	Fisher	D16	17 mM
BSA	Invitrogen	16050-122	0.1% w/v
Hydrocortisone	Sigma	H0888	0.5 mg/ml
Cholera toxin	Sigma	C8052	100 ng/ml
Penicillin-Streptomycin	Gibco	15140122	100 U/ml
EGF	Peprotech	AF-100-15	20 ng/ml
Insulin	Sigma	I9278	10 ug/ml

Seahorse Assay Medium

Component	Vendor	Catalog number	Final Concentration
Seahorse XF base medium	Agilent	103334-100	-
Sodium pyruvate	Gibco	11360070	1 mM
L-Glutamine	Gibco	35050079	2 mM

3.7.3. Reporter construction

The reporters AMPKAR2 (Hung et al., 2017) and ERKTR-mCherry (Sparta et al., 2015) were previously described. PercevalHR (Tantama et al., 2013), ATeam1.03 (Imamura et al., 2009), and GLUT1 were obtained from Addgene. TOP-H2B-YFP-DD (Han et al., 2014) was generously provided by Tobias Meyer. PercevalHR was modified with a nuclear export sequence at the C-terminus to compartmentalize the sensor in the cytosol. AMPKAR2, PercevalHR, and Ateam1.03 sensors were cloned into a vector compatible with piggyBAC transposase-mediated delivery (Yusa et al., 2011) to minimize recombination between CFP and YFP. GLUT1-IRES-NLS-mCherry was constructed by cloning the GLUT1 coding sequence (Takanaga et al., 2008) into the retroviral vector pBabe-neo (BamHI/XhoI); a nuclear localization signal (NLS) was added to mCherry by PCR and was cloned into retroviral vector pBabe-neo (BamHI/EcoRI). IRES-NLS-mCherry was then inserted at the 3' end of GLUT1 (XhoI/SalI). pLJM1-TFEB-TR. TFEBTR-mCardinal was constructed by inserting the coding sequence for TFEB residues 1-237 into pLJM1 upstream of and in-frame with the coding sequence of mCardinal. Correct insertions for all plasmids were confirmed by sequencing.

3.7.4. Reporter Delivery

Cell lines stably expressing biosensors were generated by retroviral transduction or transfection with the PiggyBac transposase system (Yusa et al., 2011). PiggyBac plasmids were delivered by electroporation (Amaxa II system, Lonza). After transfection or transduction, cells were selected with puromycin (1–2 μg/ml) or geneticin (300 μg/ml); single-cell clones were made

by limiting dilution or flow cytometry sorting. For each reporter, we isolated multiple stable clones with homogenous expression; data reported in this study reflect representative behaviors that were consistent across clones for each reporter line. Main reporter cell lines were confirmed to be mycoplasma-negative by PCR; results were validated by third-party testing of selected lines (ATCC).

3.7.5. Live-cell fluorescence microscopy

Time-lapse wide-field microscopy was performed as described previously (Hung et al., 2017; Pargett et al., 2017). Briefly, 25,000 cells were plated one day prior to imaging in glass-bottom 96-well plates (Cellvis P96-1.5H-N, Mountain View, CA) pretreated with type I collagen (Gibco A10483-01) to promote cell adherence. For experiments with drug addition, cells were placed in imaging medium until the addition of the drug. For drugs dissolved in DMSO, the final DMSO concentration was <0.1%. Cells were maintained in 95% air and 5% CO_2 at 37℃ in an environmental chamber. Images were collected with a Nikon (Tokyo, Japan) 20/0.75 NA Plan Apo objective on a Nikon Eclipse Ti inverted microscope, equipped with a Lumencor SOLA or Lumencor SPECTRA X light engine. Fluorescence filters used in the experiment are: DAPI (custom ET395/25x - ET460/50m - T425lpxr, Chroma), CFP (49001, Chroma), Sapphire (custom ET420/10x - ET525/50m - T425lpxr, Chroma), GFP (49002, Chroma), YFP (49003, Chroma), Cherry (41043, Chroma) and Cy5 (49006, Chroma). For AMPKAR2 and Ateam1.03 biosensors, CFP and YFP filters were used to acquire images, while for the PercevalHR biosensor Sapphire and GFP filters were used. Images were acquired using Andor Zyla 5.5 scMOS camera every 6 – 7 minutes with 2x2 binning. Exposure times for each channel were 25-50 ms for DAPI; 150 – 250 ms for CFP; 150 – 250 ms for YFP; 500 – 750 ms for Sapphire; 500 – 750 ms for GFP; 300 – 500 ms for Cherry and 300 – 500 ms for Cy5.

3.7.6. Immunofluorescence microscopy

At indicated times during live-cell imaging experiment, 8% paraformaldehyde was added directly into imaging media to make 2% paraformaldehyde final concentration. Paraformaldehyde fixation was performed for 15 minutes, followed by permeabilization with 100% methanol. Cells were then washed in PBS-T (0.1% Tween-20 in PBS) twice and blocked with Odyssey Blocking Buffer (Li-Cor, Lincoln, NE) for 1 hour at room temperature. Reporter fluorophores were bleached as described in the CyCIF protocol (Lin et al., 2015). Samples were then incubated with primary antibody at the indicated concentrations (see Antibody Table), diluted in blocking buffer, overnight at 4℃. Secondary staining was performed with Alexa 647-conjugated anti-rabbit (Life Technologies, A-21245, diluted at 1:1000 in blocking buffer), followed by DNA staining with Hoechst-33342 (Life Technologies, H3570, diluted at 1:1000 in PBS). Plates were imaged as described for live-cell microscopy, using DAPI and Cy5 filter sets. After imaging, the Afterwards, intensity of fixed-cell images in each condition were matched back to the corresponding time-lapse movies.

3.7.6. Single cell protein synthesis estimation by O-propargyl-puromycin (OPP)

To estimate global nascent protein synthesis rate, we pulse-labeled cells with the puromycin analog O-propargyl-puromycin (OPP; Click Chemistry Tools #1407) at 10 μM final concentration for 30 minutes before the end of live-cell imaging. After fixation, permeabilization, and fluorophore bleaching as described earlier, cells were then incubated with click chemistry reaction buffer (10 μM Azide dye + 4mM $CuSO_4$ + 50 mM Ascorbic acid in 100 mM Tris Buffer pH 8.5) containing Alexa 647 Azide dye (Click Chemistry Tools #1299) for 1 hour. Then, samples were washed with PBS three times and imaged as described earlier.

3.7.7. Phos-Tag electrophoresis and western blot

All samples for western blot experiments were collected from cells cultured in 6 well-plates at 80% confluency. Samples were lysed with ice-cold RIPA buffer. For Phos-Tag™ gel

electrophoresis, we used SuperSep™ Phos-tag™ Precast Gels (Wako; 195-17991). Samples were loaded at 3 ug/lane, as measured by BCA protein assay (Thermo Scientific 23225).

The electrophoresis running buffer was Tris-Glycine-SDS solution (25 mM Tris, 192 mM Glycine, 0.1% SDS, pH 8.3), supplied with 1.25 mM sodium bisulfite immediately before electrophoresis. Electrophoresis was performed at 100V, constant voltage for 3 hours at 4°C. After electrophoresis was completed, gels were washed in methanol-free transfer buffer (25 mM Tris, 192 mM Glycine, pH 8.3, 10 mM EDTA) 3 times, 10 minutes each in order to remove divalent cations that would immobilize phosphorylated proteins in the gel. Then gel was equilibrated in transfer buffer (25 mM Tris, 192 mM Glycine, pH 8.3, 10 mM EDTA, 20% v/v Methanol) twice, 10 minutes each. Separated proteins were transferred to PVDF membrane using wet blot transfer method at 18V, overnight at 4°C.

Following protein transfer, membranes were stained with 3% w/v Ponceau S to validate transfer efficiency, then thoroughly de-stained with Milli-Q water and 0.1%PBST (10 mM Tris–HCl (pH 7.5), 100 mM NaCl, and 0.1% v/v Tween-20). Non-specific antibody binding was blocked by incubating membranes in Odyssey blocking buffer (Licor; 927-40000) for 1 hour at room temperature. Primary antibodies (Rabbit Anti-GFP, CST 2956) were diluted to 1:1000 in blocking buffer and incubated with the membrane overnight at 4°C to detect the AMPKAR2 reporter, Following extensive washing in 0.1%PBST (3 times, 10 minutes each), membranes were incubated with diluted IRDye 800CW (Licor; 926-32211) secondary antibodies for 1 hour, at room temperature. After washing in 0.1%BST (3 times, 10 minutes each) immunoreactive bands were recorded with an Odyssey CLx imaging system.

3.7.8. Luminescence ATP determination

ATP concentration for bulk cell populations was determined using an ATP determination kit (Thermo Fisher, A22066), using protocol provided by the manufacturer with minor modification

as follows. Cells were plated in 96-well plate at 25000 cell/well 1 day before the experiment and treated as previously described for live-cell microscopy. Samples were collected at indicated time points by incubation with Trichloracetic acid (TCA), final concentration of 2.5% v/v, at 4° C for 30 minutes. After cell lysis, samples were diluted five-fold to minimize TCA concentration (now 0.5% v/v). 10 µl of diluted sample was added to 90 µl reaction solution (see product manual), in 96-well plate assay plate (Corning 3603) followed by incubation for 15 minutes at room temperature. Luminescence was monitored by microplate reader (Molecular Device, SpectraMax M5) at 560 nM, room temperature.

3.7.9. Measurement of mitochondrial stress responses and ATP flux from glycolysis/oxidative phosphorylation

XF24 cell culture plates and sensor cartridges (100867–100) were purchased from Seahorse Bioscience (North Billerica, MA). Cells were plated in XF24 cell culture plates at a density determined by optimization experiments (35000 cells/well) and incubated at 37˚C with 5% CO_2 overnight in growth medium; even distribution of cells was verified visually. For the mitochondrial stress test, the growth medium was completely removed 24 hours after plating, and cells were washed twice with 1,000 ml of pre-warmed imaging medium 1. 500 ml of imaging medium 1 was added to each well and cells were incubated in a 37℃ incubator without CO_2 for 1 hr to allow cell equilibration with Imaging medium 1 (see Media Table). Oxygen consumption rates were measured with the XF24 analyzer under this basal condition followed by sequential addition of different oligomycin concentration, as indicated in Supplementary Figure 4A. For ATP fluxes from glycolysis and oxidative phosphorylation estimation, the data collected in the previous study (Hung et al., 2017) using Seashorse Assay Medium (see Media Table) was applied to formula previously described by Mookerjee et al.(Mookerjee et al., 2017).

3.7.10. GC-TOF analysis of metabolites

For GCMS analysis, cells were plated in 10 cm plates at 10^7 cells per plate. After incubation overnight, the growth medium was replaced with 10 ml of 'Imaging medium 1' supplied with 17 mM glucose. After 4 hours of incubation, cells were treated with oligomycin 1.8 µg/ml. Samples were later prepared for gas chromatography study as described in (Fiehn, 2016). Briefly, samples were quenched by immediately replacing the media with 1 ml of pre-chilled, degassed 3:3:2 v/v acetonitrile:isopropanol:water (Fisher) at 0,30,60,150 and 270 minutes following oligomycin, representing the average first peak, trough, and second peak of the $AMPKAR2^{PHOS}$ response to OXPHOS inhibitors. After quenching, samples were flash-frozen in liquid nitrogen and stored in -80^{o}C freezer.

Prior to GC-TOF analysis, all samples were thawed at room temperature and centrifuged at 14,000 rcf. Supernatants were removed, and samples evaporated to dryness using a CentrVap. To remove membrane lipids and triglycerides, dried samples were resuspended with 1:1 v/v acetonitrile:water, decanted and evaporated to dryness using a CentrVap. Internal standards, C8–C30 fatty acid methyl esters (FAMEs), were added to samples and derivatized with methoxyamine hydrochloride in pyridine followed by MSTFA (Sigma-Aldrich 69479) for trimethylsilylation of acidic protons. Derivatized samples were subsequently submitted for analysis by GC-TOFMS.

Primary metabolite data was collected using a Leco Pegasus IV time of flight (TOF) MS (Leco Corporation) coupled to an Agilent 6890 GC (Agilent Technologies) equipped with a 30 m long 0.25 mm id Rtx5Sil-MS column (30 m × 0.25 mm; 0.25 µm phase) and a Gerstel MPS2 automatic liner exchange system (Gerstel GMBH & Co. KG). The chromatographic gradient used a constant flow of 1 ml/min, and an oven temperature ramping from 50°C for to 330°C over 22 minutes. Mass spectrometry data were collected using 1525 V detector voltage at m/z 85–500 with 17 spectra/sec, electron ionization at −70 eV and an ion source temperature of 250°C. QC injections, blanks, and pooled human plasma were used for quality assurance throughout the run.

Data were processed by BinBase (Fiehn et al., 2005) for deconvolution, peak picking, filtering, and metabolite identifications.

3.8. Quantification and statistical analysis

3.8.1. Image processing

After background subtraction and flat field correction, image data were processed to segment and average pixels within each identified cell's nucleus and cytoplasm, using a custom procedure written for MATLAB (Pargett et al., 2017), with modifications in the cytosolic identification protocol as described below. Image data were stored in ND2 files generated by NIS Elements and accessed using the Bio-Formats MATLAB toolbox. Individual cells were tracked over time using uTrack 2.0 (Jaqaman et al., 2008). Cytoplasmic masks were created by watershed method (Vincent and Soille, 1991) using cytosolic YFP (for cell lines expressing AMPKAR2 or ATeam1.03) or GFP (for cell lines expressing PercevalHR) to identify the cytosolic boundary. The cytosolic area is further restricted to the area within 5 pixels from the nuclear border. The resulting single-cell time series traces were filtered for quality by a minimum length of trace and maximum number of contiguous missing or corrupt data points.

3.8.2. FRET reporter calibration and measurement

To quantify FRET biosensors (AMPKAR2 and ATeam1.03), we calculated FRET efficiency exactly as shown previously (Gillies et al., 2020), using a spectral model of light propagated through the microscopy system, including the live cell specimen. Since AMPKAR2 reporter is a substrate for AMPK kinase activity, it is possible to estimate the fraction of sensor that is phosphorylated using Phos-Tag^{TM} electrophoresis, followed by immunoblot against GFP (see Phos-Tag electrophoresis and western blot). This measurement allows us to convert FRET ratios to the fraction of AMPKAR2 sensor that is phosphorylated, AMPKAR2^{PHOS}. Western blot images were manually segmented to quantify protein bands using ImageJ and quantified as

average band intensity. AMPKAR2 phosphorylation fraction was calculated by computing the ratio of the phosphorylated band over the summation of phosphorylated and unphosphorylated bands. Conditions shown in Supplementary Figure 1C-D (4 replicates per treatment) were selected because they exhibit sustained AMPKAR2 activity over a range of intensities. The average fraction of reporter phosphorylated was quantified in each condition and compared with the average FRET efficiency as calculated from live-cell experiments with corresponding treatments and time points. Linear fitting was performed, providing a calibrated measurement of the fraction of AMPKAR2 phosphorylated, based on live-cell measurements (eq 1).

$$AMPKAR2^{PHOS} = 2.74[AMPKAR2_{FRET\ ratio}] - 0.59 \qquad (1)$$

3.8.3. Perceval reporter measurement

Unlike FRET reporters, PercevalHR has only one fluorophore, cp173 mVenus, that binds to ATP and ADP differentially, resulting in a shift of excitation spectra with peaks at 470 nM (ATP-bound) and 405 nM (ADP-bound)(Tantama et al., 2013). To measure the proportions of these forms, we imaged cells expressing PercevalHR reporter with Sapphire and GFP filters (see Live-cell fluorescence microscopy). To account for variation in microscope light source set up from experiment to experiment, we scaled image measurements by the relative excitation intensity and exposure time delivered in each channel. The ratio of intensity when excited by Sapphire and GFP filters, which we term Perceval^{EX}, reflects the ratio of ADP to ATP.

3.8.4. Cell age and sister cell analysis

For sister cell analysis, we expressed an NLS-mCherry nuclear marker in MCF10A-AMPKAR2 cell line to improve nuclei tracking accuracy across cytokinesis. Cell division events were first automatically identified by uTrack2.0 (Jaqaman et al., 2008) and later manually verified. In total, we were able to record more than 5,500 cell division events (11,000 related cells) within

25 hours. This dataset gave us estimates on both each cell's age and their lineage at the time they were challenged with oligomycin.

The similarity of AMPKAR2^{PHOS} response between cell sister cells was calculated by computing the Euclidean distance of AMPKAR2^{PHOS} responses within the 2-hour window after oligomycin treatment. To determine whether AMPKAR2^{PHOS} response between sister cells was more similar than that of unrelated cells, we generated 1000 random pairs of cells that divided at the same time and computed the average AMPKAR2^{PHOS} Euclidean distance. We were able to estimate the Euclidean distance of AMPKAR2^{PHOS} between unrelated cells with 95% confidence interval. The age-dependent increase in the AMPKAR2^{PHOS} Euclidean distance was fitted by an exponential function to estimate the half-life.

3.8.5. Analysis and statistics of kinetics in reporter signals

A custom MATLAB algorithm was designed to identify peaks (Gillies et al., 2017) in the time-lapse signals of AMPKAR2, PercevalHR, and Ateam1.03 activity. The AMPK, PercevalHR, and Ateam1.03 were first smoothened using Butterworth low pass filter with a 3-timepoint cutoff period to remove spurious noise. Peaks and associated valleys in the index were identified by setting two local cutoff values, based on maximum and minimum values of the data within a sliding time window (typically 120 minutes for AMPKAR2 and PercevalHR, 30 minutes for Ateam1.03). A peak was detected if both cutoff values were crossed by a rise and subsequent fall in the index. Typically, more than 300 individual cell recordings were scored for each condition and plotted as a histogram.

For long-term AMPK activity analysis, we identified the 'strong' phases of low AMPK activity (OP-ind) as follows. First, we applied the moving standard deviation with a 3-hour sliding window to AMPKAR traces from cells treated with oligomycin. We chose a 3-hour sliding window, because the peak-to -peak period of AMPK activity is around 2 hours, making 3 hours the Nyquist

interval. Next, we used the 95th percentile of the calculated moving standard deviation values from all cells treated with vehicle to set a cut-off point for 'strong' AMPK activity (Figure S4A, upper panel). Any sections of AMPK activity trace that had a moving standard deviation period below the cut-off for longer than 3 hours were designated as '' AMPK response phases

3.8.6. GC-TOF data analysis

Peak heights of each metabolite were used for further statistical analysis. First, data were normalized by using the sum of the knowns, or mTIC normalization, to scale each sample. Peak heights were then submitted using R to DeviumWeb (v0.3.2). The data were normalized further by log transformation and Pareto scaling. ANOVA analysis was performed with Tukey post hoc testing with an alpha of 0.05. The reported trends in metabolite abundance following oligomycin treatment were robust to the normalization scheme and could also be observed in raw peak values.

3.8.7. Distributions and statistical tests

Statistical tests, including ANOVA, t-tests, and Pearson's correlations, were performed using standard functions in MATLAB. R^2 values were calculated as the square of the Pearson correlation coefficient. Where indicated in the figure legends, a linear regression model was generated, using the MATLAB command *fitlm*. Box and whisker plots show the median value (red line), interquartile range (box), range (whiskers), and outliers (plus symbols); for all other cases, definition of centers and dispersion measures are listed in the figure legends. Distributions of single-cell measurements were plotted and inspected visually to confirm that they met the assumptions of the statistical tests used. To test for bimodality, data were fitted to a bimodal Gaussian mixture distribution and a panel of unimodal distributions, including (including normal, log-normal, generalized extreme value, and Weibull). The best-fitted distribution was selected using corrected Akaike's Information Criterion, to account for additional parameter terms

(Cavanaugh, 1997). Data were considered bimodally distributed if and only if the bimodal Gaussian mixture distribution was ranked as the best-fitted distribution.

3.8.8. Pearson's cross-correlation of time series

The time series to be compared were normalized by subtracting by their corresponding averages. To quantify lag between reporters for each time series, the maximal cross-correlation value was computed using the MATLAB *xcorr* function. We assumed that each pair of reporters, namely AMPKAR2 and TFEB-TR or AMPKAR2 and ERKTR, had a characteristic lag time, estimated as the mode of calculated lags across all sampled cells. The lag times identified from this process were used to align two time-series data. Pearson's correlation coefficient was computed from these aligned time series for each cell. Significance of the differences between the Pearson's coefficient distributions for different treatments was calculated by t-test.

3.8.9. Partial least squares regression modeling

To evaluate the relative contributions of glycolytic activity, protein synthesis rate and cell cycle stage to AMPK responses to OXPHOS inhibition, we performed live-cell experiments using MCF10A cells expressing AMPKAR2 and GLUT1-NLS mCherry, in which allows glycolytic capacity can be estimated by measuring mCherry intensity. After 4 hours of live imaging, cells were pulse-labeled with OPP for 30 minutes and later treated with oligomycin 1.8 μg/ml for 15 minutes prior to fixation. Samples were bleached and stained with phospho-Rb and Hoechst 33342 as described earlier. Intensity of mCherry, OPP, phospho-Rb and Hoechst were used as proxies of glycolytic activity, protein synthesis rate, G1/S transition, and DNA content, respectively. Since the relationship between DNA content and phospho-Rb is not linear, as shown in Figure 6A, we created a linearized pseudotime variable for cell cycle progression using Wanderlust (Bendall et al., 2014). AMPKAR2Δ in response to oligomycin treatment was used as the output variable for PLSR models, while mCherry, OPP, DAPI, phospho-Rb and cell cycle

pseudotime values were used as input variables. Data were first centered by subtracting the mean from each parameter and input parameters were scaled to unit variance. The MATLAB implementation of the SIMPLS partial least squares regression algorithm was employed to fit paired data sets to a linear model.

3.8.10. Replicates

Numbers of independent replicates are indicated in each figure legend as “N”; we define ‘independent replicate’ as a complete, separate performance of a time-lapse imaging experiment with similar culture and treatment conditions, beginning from the plating of cells from bulk culture on an imaging plate and occurring on different days from other replicates. For all independent replicates, a minimum of 200 cells were imaged and tracked in each condition. Unless noted otherwise, where single-cell recordings are shown, the displayed cells were chosen by random number generation in MATLAB with a threshold for minimum tracking time to eliminate cells in which recording was terminated prematurely due to failure of the tracking algorithm. The chosen tracks were manually verified to be representative of successfully tracked cells and consistent with the overall range of cell behaviors. Cellular measurements determined by manual inspection to have poor tracking or quantification accuracy were discarded.

3.9. Key Resource Table

REAGENT or RESOURCE	SOURCE	IDENTIFIER
Antibodies		
Phospho-Rb (Ser807/811) (D20B12)	Cell Signaling Technology	RRID:AB_1117865 8Cat#8516
Phospho-Acetyl-CoA Carboxylase (Ser79) (D7D11)	Cell Signaling Technology	RRID:AB_2687505 Cat#11818
Phospho-S6 Ribosomal Protein (Ser240/244) (D68F8)	Cell Signaling Technology	RRID:AB_1069423 3 Cat#5364
Phospho-4E-BP1 (Thr37/46) (236B4)	Cell Signaling Technology	RRID:AB_560835 Cat#2855
Phospho-p44/42 MAPK (Erk1/2) (Thr202/Tyr204) (D13.14.4E)	Cell Signaling Technology	RRID:AB_2315112 Cat#4370
GFP (4B10)	Cell Signaling Technology	RRID:AB_1196614 Cat#2955
Goat anti-Rabbit IgG Alexa 647	Life Technologies	RRID:AB_2535813 A-21245
Chemicals, Peptides, and Recombinant Proteins		
Oligomycin A	Sigma	Cat#75351
Insulin	Sigma	Cat#I9278
EGF	Peprotech	Cat#100-15
Hydrocortisone	Sigma	Cat#H0888
Cholera Toxin	Sigma	Cat#C8052
DMEM/F12	Invitrogen	Cat#11330-032
Pen/Strep	Invitrogen	Cat#15070-063
Antimycin A	Sigma	Cat#A8674
Rotenone	Sigma	Cat#45656
FCCP	Sigma	Cat#C2920
Glucose	Fisher	Cat#D16
MK2206	Selleckchem	Cat#S1078
Torin1	Selleckchem	Cat#S2827
2DG	Sigma	Cat#D8375
3PO	Selleckchem	Cat#S7639
BU99006	Santa Cruz Biotechnology	Cat#SC-300307
CAS-648926-15-2	EMD Millipore	Cat#361515
Etomoxir	Sigma	Cat#E1905
6AN	Cayman Chemical	Cat#10009315

Cycloheximide	EMD Millipore	Cat#239763
Collagen I, Rat tail	Gibco	Cat#A10483-01
Bafilomycin A	Cayman Chemical	Cat#11038
SBI0206965	Sigma	Cat#SML1540
PF0175157	Sigma	Cat#PZ0299
Paraformaldehyde 8%	Electron Microscopy Sciences	Cat#157-8-100
Hoechst 33342	Life Technologies	Cat#H3570
Cell Culture Media		
DMEM/F-12 1:1	Life Technologies	Cat#11320
Horse Serum	Invitrogen	16050-122
DMEM	Life Technologies	11965175
FBS	Life Technologies	11965175
Experimental Models: Cell lines		
MCF10A	Janes et al., 2010	RRID:CVCL_0598
184A1	ATCC	RRID:CVCL_3040
MCF7	ATCC	RRID:CVCL_0031
U87	ATCC	RRID:CVCL_0022
A549	ATCC	RRID:CVCL_0023
MCF10A-AMPKAR2	(Hung et al, 2017)	
MCF10A-AMPKAR2-ERKTR	This report	
MCF10A-AMPKAR2-TFEBTR	This report	
MCF10A-PercevalHR	This report	
MCF10A-Ateam	This report	
MCF10A-AMPKAR2-GLUT1_NLSmCherry	This report	
MCF10A-AMPKAR2-Geminin::mCherry	This report	
MCF10A-AMPKAR2-NLS::mCherry	This report	
MCF10A-TOP	This report	
184A1-AMPKAR2	This report	
MCF7-AMPKAR2	This report	
U87-AMPKAR2	This report	
A549-AMPKAR2	This report	
Recombinant DNA		
pPBJ-AMPKAR2-puro	(Hung et al, 2017)	
pLJM-ERKTR::mCherry	(Sparta et al., 2015)	
GW1-PercevalHR	(Tantama et al., 2013)	Addgene#49082
pPBJ-PercevalHR-puro	This report	

ATeam1.03-nD/nA/pcDNA3	(Imamura et al., 2009)	Addgene#51958
pPBJ-Ateam1.03-puro	This report	
TOP-H2B-YFP-DD	(Han et al., 2014)	Addgene#96891
pLJM-geminin::mCherry	(Hung et al., 2017)	
pLJM-TFEBTR::mCardinal	This report	
pBabe-NLS::mCherry	This report	
pBabe-GLUT1-NLS::mCherry	This report	
Software and Algorithms		
NIS-Elements AR ver. 4.20	Nikon	RRID:SCR_014329
Bio-Formats ver. 5.1.1 (May 2015)	OME	RRID:SCR_000450
uTrack 2.0	(Jaqaman et al., 2008)	http://www.utsouthwestern.edu/labs/danuser/software/
MATLAB	Mathworks	SCR_001622
Other		
Glass Bottom Plates, #1.5 cover glass	In Vitro Scientific	Cat#P24-1.5H-N, P96-1.5H-N

3.10. Supplementary Materials

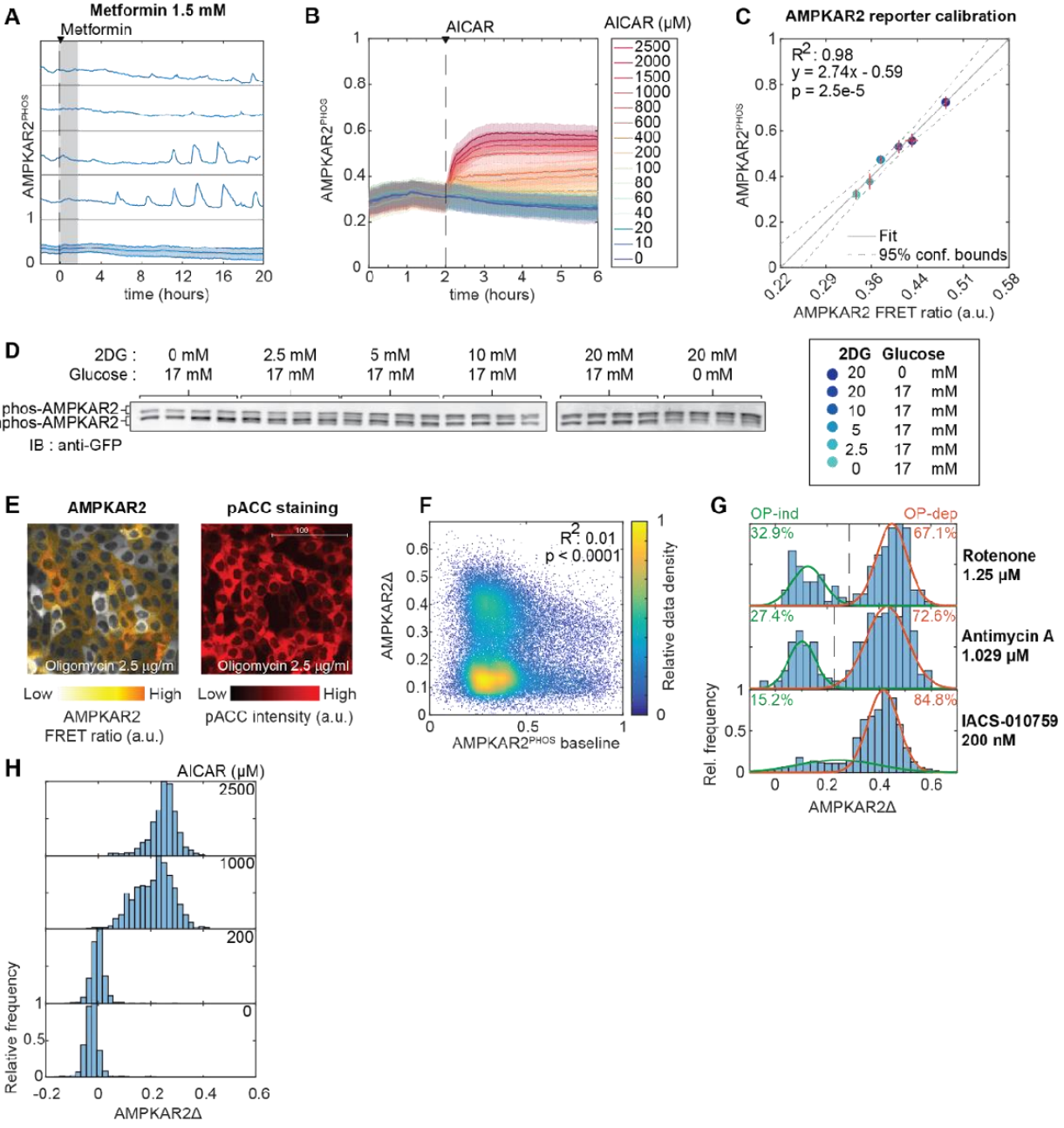

Supplemental Figure S3.1, Related to Figure 3.1

A: Representative AMPKAR2^{PHOS} measurements for cells grown in 17 mM glucose and treated with 1.5 mM metformin. Each subplot represents a single cell measurement, with population average and interquartile range in the bottom subplot. The shaded area shows the 2-hour time window of the data used for analysis. N=2. B: Population average AMPKAR2^{PHOS} measurements for cells grown in 17 mM glucose, treated with AICAR at the indicated doses. The shaded areas represent interquartile ranges. N=2. C: Scatter plot of the correlation between FRET ratio of AMPKAR2 reporter, as measured by live-cell microscopy, and its phosphorylation status, as

measured by phos-tag gel electrophoresis under the same conditions. A range of AMPK activities were induced by varying glucose and 2-deoxyglucose (2DG). Error bars represent standard errors of the mean (SEM) from at least two different experiments. The solid line represents a fitted linear model, and the dashed lines show 95% confidence bounds. This fitted equation is used throughout the study to report all AMPKAR2 FRET measurements as the fraction of AMPKAR2 phosphorylated, AMPKAR2^{PHOS}. N=4. D: Measurement of AMPKAR2 phosphorylation status by immunoblot. Image shows a representative immunoblot used to obtain the AMPKAR2^{PHOS} measurements in (C). Phos-tag gel electrophoresis was used to separate phosphorylated and unphosphorylated forms of the reporter (upper and lower bands, respectively), with anti-GFP used to detect both forms. N=4. E: Representative image of AMPKAR2 FRET activity (shown as a ratiometric image) and the corresponding pACC immunofluorescence pattern after the same cells were fixed and stained. F: Scatter plot of baseline AMPKAR2^{PHOS} (prior to oligomycin treatment) and corresponding AMPKAR2Δ for each cell following oligomycin (1.8 µg/ml). Colormap represents relative data density. N=2. G: Histogram of AMPKAR2Δ values after treatment with the indicated inhibitors. Green and orange lines are fitted Gaussian distributions. The dashed line is defined by the intersection between distributions and used as the cutoff to calculate the fractions of OP-ind and OP-dep cells, which are shown as percentages. N=2. H: Histogram of AMPKAR2^{PHOS} amplitudes after treatment with varied concentrations of AICAR, as shown in (B). Note the lack of clear bimodal distributions, in contrast to the distributions at maximal doses of electron transport chain inhibitors (G). N=2.

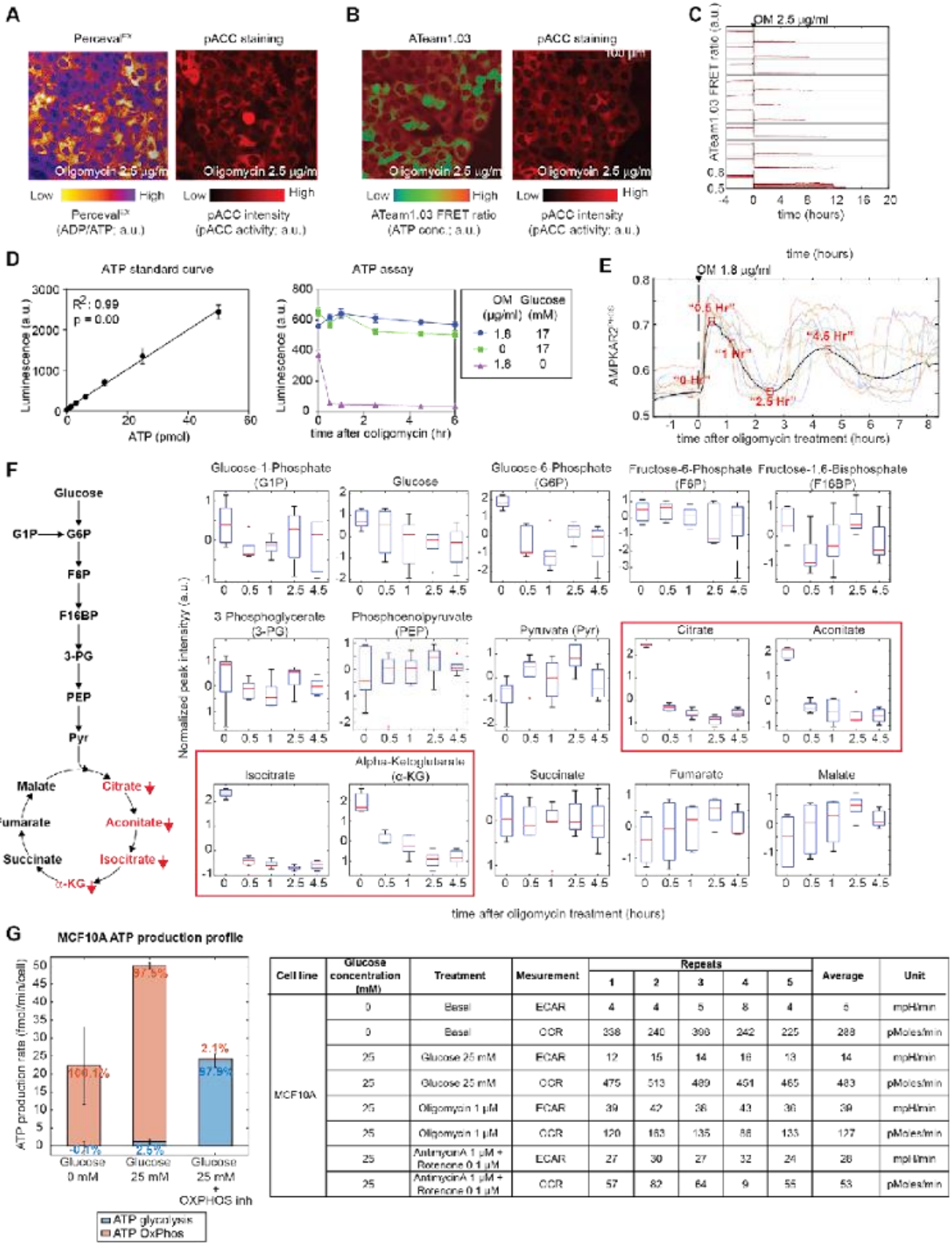

Cell line	Glucose concentration (mM)	Treatment	Mesurement	Repeats					Average	Unit
				1	2	3	4	5		
MCF10A	0	Basal	ECAR	4	4	5	8	4	5	mpH/min
	0	Basal	OCR	338	240	398	242	225	288	pMoles/min
	25	Glucose 25 mM	ECAR	12	15	14	16	13	14	mpH/min
	25	Glucose 25 mM	OCR	475	513	489	451	465	483	pMoles/min
	25	Oligomycin 1 µM	ECAR	39	42	36	43	36	39	mpH/min
	25	Oligomycin 1 µM	OCR	120	163	135	88	133	127	pMoles/min
	25	Antimycin A 1 µM + Rotenone 0.1 µM	ECAR	27	30	27	32	24	28	mpH/min
	25	Antimycin A 1 µM + Rotenone 0.1 µM	OCR	57	82	64	9	56	53	pMoles/min

Supplemental Figure S3.2, Related to Figure 3.3

A and B: Sample images of Perceval^{EX} and ATeam1.03 FRET activity and their corresponding pACC staining pattern in response to 2.5 µg/ml oligomycin. Reporter images were acquired in live cells at 30 minutes after oligomycin treatment. Cells were then immediately fixed and stained for pACC. N=2. C: Rapid drop in ATP as measured by ATeam1.03 after treatment with 2.5 µg/ml oligomycin in the absence of glucose. Each subplot represents a single cell measurement, with population average and interquartile range in the bottom subplot. N=2. D: Bulk population measurements of ATP following oligomycin treatment. Left panel: standard curve for ATP assay, generated with known quantities of ATP. Right panel: Bulk ATP measurements for MCF10A cells cultured in the indicated glucose concentrations and treated with oligomycin at time 0. N=5. E: Data collection scheme for bulk analysis of metabolites. Black line indicates the population mean of AMPKAR2^{PHOS} after oligomycin treatment, and lighter lines individual cells. Note that fluctuations in AMPK activity remain synchronous for the first 6 hours following treatment. Red boxes indicate time points at which samples were collected for mass spectrometry analysis. F: Mass spectrometry analysis of metabolites in oligomycin-treated cells. Left panel: schematic of analyzed metabolites in glycolysis and TCA cycle. Right panels: box plots of relative metabolite concentrations measured by mass spectrometry. Red font and boxes show metabolites that were significantly reduced after OXPHOS inhibition. Error bars represent the standard deviation for 6 replicate cultures assayed in parallel. G: Estimated ATP production by glycolysis and OXPHOS in MCF10A cell line under the indicated conditions. Measurements of oxygen consumption rate (OCR) and extracellular acidification rate (table, right) were made using a Seahorse bioanalyzer (table, right); some measurements were previously reported (Hung et al., 2017). These values were used to calculate ATP production rates (bar graph, left) using the procedure described in (Mookerjee et al., 2017). Error bars represent the standard deviations of four replicates. Percentages indicate the fraction of total ATP production by OXPHOS (red) and glycolysis (blue) within each condition.

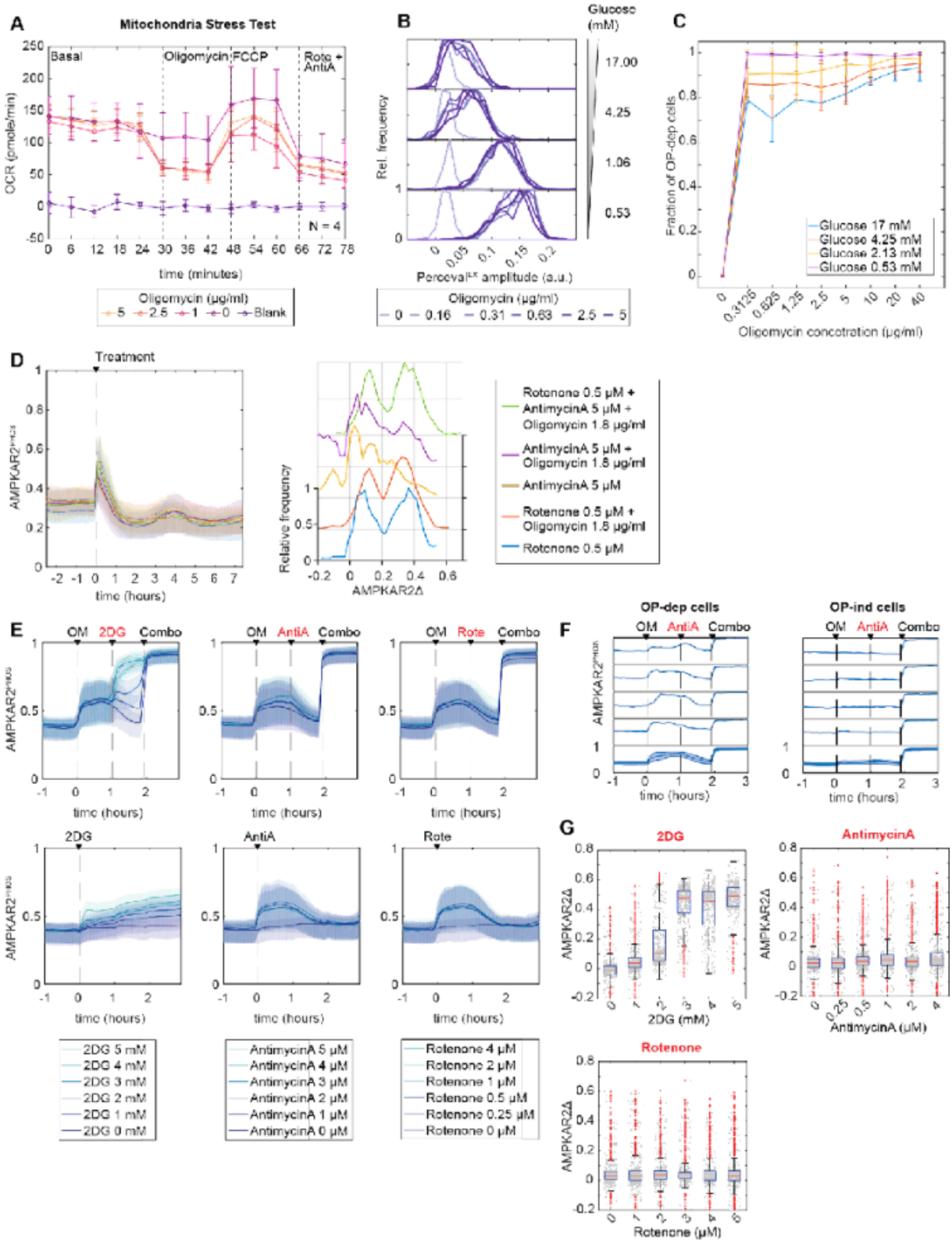
A
Mitochondria Stress Test
Basal
Oligomycin
FCCP
Rote + AntiA
OCR (pmole/min)
time (minutes)
N = 4
Oligomycin (µg/ml)
5
2.5
1
0
Blank
B
Glucose (mM)
17.00
4.25
2.13
0.53
Rel. frequency
Perceval^LX amplitude (a.u.)
Oligomycin (µg/ml)
0
0.16
0.31
0.63
2.5
5
C
Fraction of OP-dep cells
Glucose 17 mM
Glucose 4.25 mM
Glucose 2.13 mM
Glucose 0.53 mM
Oligomycin concotration (µg/ml)
D
Treatment
AMPKAR2^nuc
time (hours)
Relative frequency
AMPKAR2Δ
Rotenone 0.5 µM + AntimycinA 5 µM + Oligomycin 1.8 µg/ml
AntimycinA 5 µM + Oligomycin 1.8 µg/ml
AntimycinA 5 µM
Rotenone 0.5 µM + Oligomycin 1.8 µg/ml
Rotenone 0.5 µM
E
OM
2DG
Combo
AntiA
Rote
AMPKAR2^nuc
time (hours)
2DG 5 mM
2DG 4 mM
2DG 3 mM
2DG 2 mM
2DG 1 mM
2DG 0 mM
AntimycinA 5 µM
AntimycinA 4 µM
AntimycinA 3 µM
AntimycinA 2 µM
AntimycinA 1 µM
AntimycinA 0 µM
Rotenone 4 µM
Rotenone 2 µM
Rotenone 1 µM
Rotenone 0.5 µM
Rotenone 0.25 µM
Rotenone 0 µM
F
OP-dep cells
OP-ind cells
OM
AntiA
Combo
AMPKAR2^nuc
time (hours)
G
2DG
AntimycinA
Rotenone
AMPKAR2Δ
2DG (mM)
AntimycinA (µM)
Rotenone (µM)

Supplemental Figure S3.3, Related to Figure 3.3

A: Oxygen consumption rate of MCF10A-AMPKAR2 cell line measured by Seahorse XF assay. Cells were treated with oligomycin as indicated, followed by 5 µM FCCP and a combination of 2.5 µM rotenone and 2.5 µM antimycin A to completely inhibit cellular respiration. 'Blank' indicates measurement from a well without any cells. N=4. B: Perceval^{EX} response to different concentrations of oligomycin, as indicated, at different glucose concentrations. Note that the distribution of responses depends primarily on glucose concentration, rather than oligomycin concentration. N=2. C: Fraction of OP-dep cells observed when treated with varying doses of oligomycin at indicated glucose concentrations. Concentrations of oligomycin >0.16 µg/ml are sufficient to increase ADP/ATP ratio in 100% of cells in <4mM glucose (S3.3.B), which indicates that the drug is fully active in all cells at this concentration. However, the same oligomycin concentrations fail to induce 100% OP-dep cells in the presence of >4mM glucose, arguing that the resistance of cells is due not to a failure of the drug to achieve target inhibition, but instead to metabolic differences between cells that manifest at higher glucose levels. N=2. D: AMPKAR2^{PHOS} responses for simultaneous treatment with multiple OXPHOS inhibitors. Left panel: population average of AMPKAR2^{PHOS} response to OXPHOS inhibitor combinations as indicated. Right panel: AMPKAR2Δ distribution after treatment with the indicated OXPHOS inhibitor combinations. Note that OP-ind cells persist even under treatment with multiple OXPHOS inhibitors. It is unlikely that these drugs share a common resistance mechanism that could simultaneously prevent all of them from blocking OXPHOS. N=2. E: AMPKAR2^{PHOS} responses for sequential treatment with metabolic inhibitors. Upper panels: population average of AMPKAR2^{PHOS} response when cells were first treated with 1.8 µg/ml oligomycin, followed by a second challenge one hour later (red font) with 2-deoxyglucose (2DG), antimycin A, or rotenone at the indicated concentration. In the last step cells were treated with combination of 20 mM 2DG, 10 µM antimycin A and 5 µM rotenone (Combo) to maximize AMPKAR2^{PHOS} activation. Bottom panels - population averages of AMPKAR2^{PHOS} response to 2DG, antimycin A or rotenone alone at indicated concentrations. N=2. F: Example single-cell AMPKAR2^{PHOS} measurements from the experiments shown in Fig S4E. Note that AMPKAR2^{PHOS} in OP-ind cells remains unchanged after the second challenge with 5 µM antimycin A. Population average and interquartile range are shown in the bottom subplot. G: AMPKAR2Δ distributions in OP-ind cells for the second challenge as described in Fig S4E.

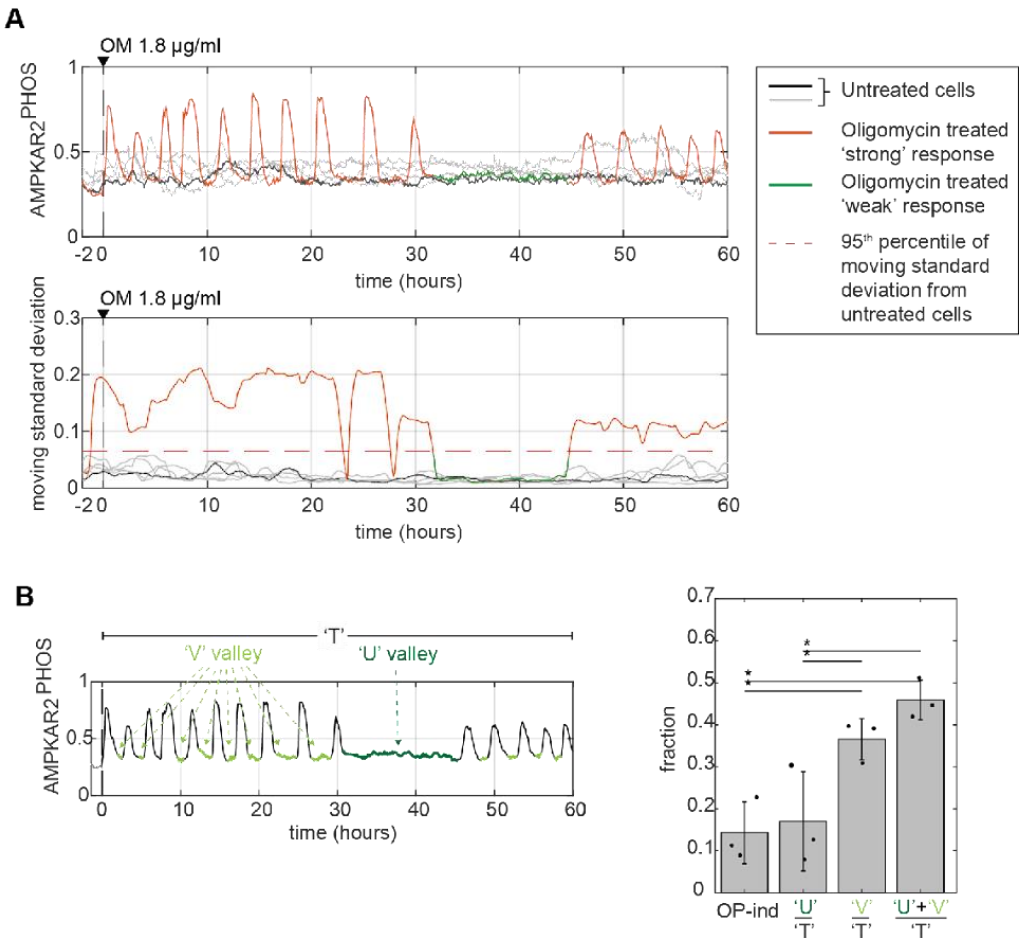

Supplemental Figure S3.4, Related to Figure 3.4

A: Identification of OP-ind-like cell states in single-cell time courses of AMPK activity. Moving standard deviation with 3-hour sliding window (moving SD) was applied to AMPKAR2^{PHOS} traces. The 95th percentile of moving SD from untreated cells (black and gray lines) was chosen as a cut-off for the 'strong' AMPK response; any part of AMPKAR2^{PHOS} trace falling below the cut-off value for longer than 3 hours was identified as a 'weak' AMPK response period (green lines). B: Analysis of the frequency of OP-ind cells relative to the dynamics of AMPK activity. Our objective was to determine whether the OP-ind responses observed on the initial treatment with OXPHOS inhibitors correspond to the regularly occurring decreases in AMPKAR2^{PHOS} ("V" valleys), the prolonged regions without AMPK activity peaks ("U" valleys), or both. In a population of cells treated with oligomycin for a prolonged period of time, we calculated the fraction of time spent in "V" valleys, "U" valleys, or the sum of both, and compared these values to the frequency of OP-ind cells occurring at initial treatment. The frequency of OP-ind cells is most closely matched by the duration of "U" valleys, while "V" valleys account for a much larger amount of time. This comparison is consistent with the interpretation that "U" valleys represent a pre-existing cell state that manifests as OP-ind cells upon challenge with an OXPHOS inhibitor. In contrast, "V" valleys are more likely to be a kinetic component of the AMPK response triggered only after OXPHOS inhibition has been initiated.

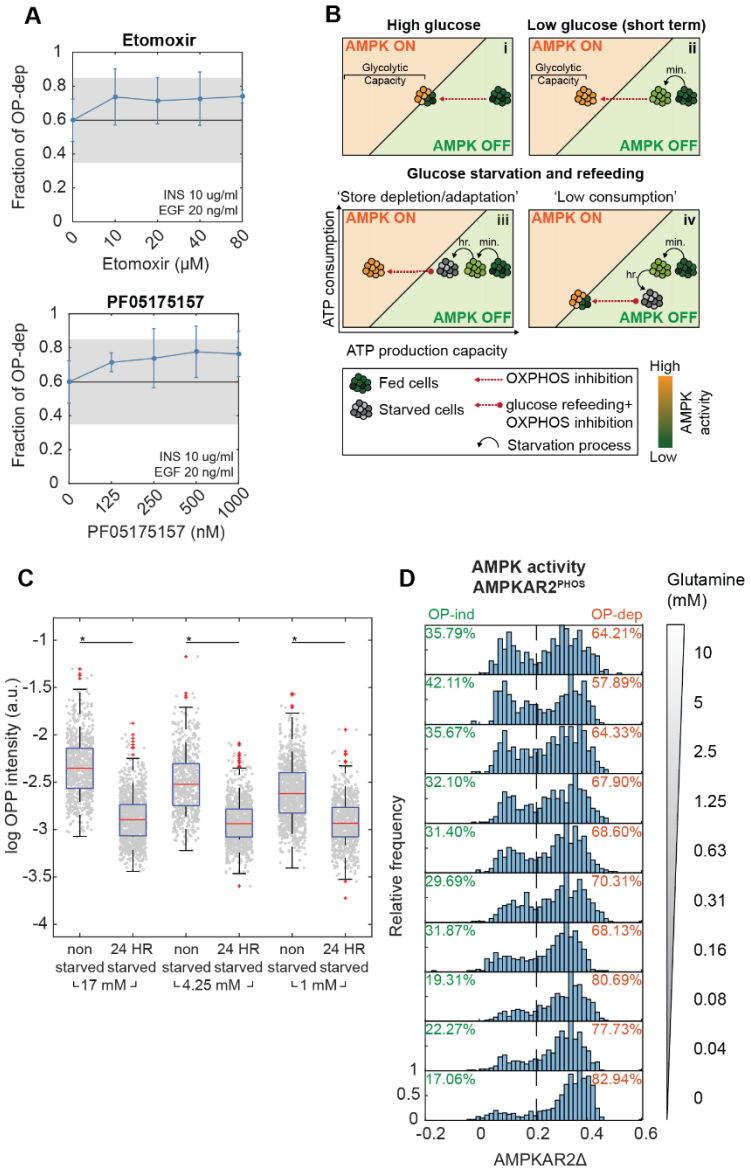

Supplemental Figure S3.5, Related to Figure 3.5

A: Lack of significant changes in OP-dep responses after inhibition of fatty acid oxidation or synthesis. Lines show the fraction of OP-dep responses to treatment with oligomycin in the presence of etomoxir (carnitine palmitoyl transferase inhibitor) or PF05175157 (acetyl-CoA carboxylase inhibitor). The horizontal black line indicates the fraction of OP-dep cells under control treatment (DMSO); points falling outside the gray region are considered significant by t-test. N=2. B: Inferred cellular metabolic states as a function of ATP production (horizontal axes) relative to ATP consumption (vertical axes). The diagonal line in each panel represents the amount of ATP production capacity that is needed to meet a given level of ATP consumption without perturbing energy charge and triggering AMPK activity. Under high glucose (i), cells have excess ATP production capacity, but OXPHOS inhibition treatment reduces ATP production

acutely. Some cells retain sufficient glycolytic capacity to meet the demands of consumption, averting AMPK activation. Under low glucose (ii), glycolytic capacity is immediately reduced and all cells fail to satisfy ATP demands following OXPHOS inhibition, and thus fall in the OP-dep region. (iii-iv) Hypotheses for metabolic adaptation to long-term glucose starvation. In (iii), starvation may cause cells to deplete metabolite stores or may change their gene expression profile to reduce glycolytic capacity; upon re-supply of glucose followed immediately by OXPHOS inhibitor treatment, such cells would score as OP-dep. Alternatively (iv), glucose-starved cells may reduce their ATP consumption by downregulating energy-consuming processes; upon glucose resupply and OXPHOS inhibitor treatment, these cells would need less ATP production capacity to meet their demands and would score as OP-ind. C: Reduction of protein synthesis rate in glucose-starved cells. Data points show the intensity of OPP labeling in cells that are either non–starved or starved of glucose for 24 hours. The glucose concentrations shown indicate the level of glucose used to culture the cells for 1 day prior to the starvation period and, for the non-starved cells, during the final 24 hours. Stars indicate p-value < 0.05 by t-test comparison. N=2. D: Increase in OP-ind responses in the presence of glutamine. Histogram shows distributions of AMPKAR2Δ after oligomycin treatment in imaging medium 1 containing 17 mM glucose and glutamine at the indicated concentrations. N=2.

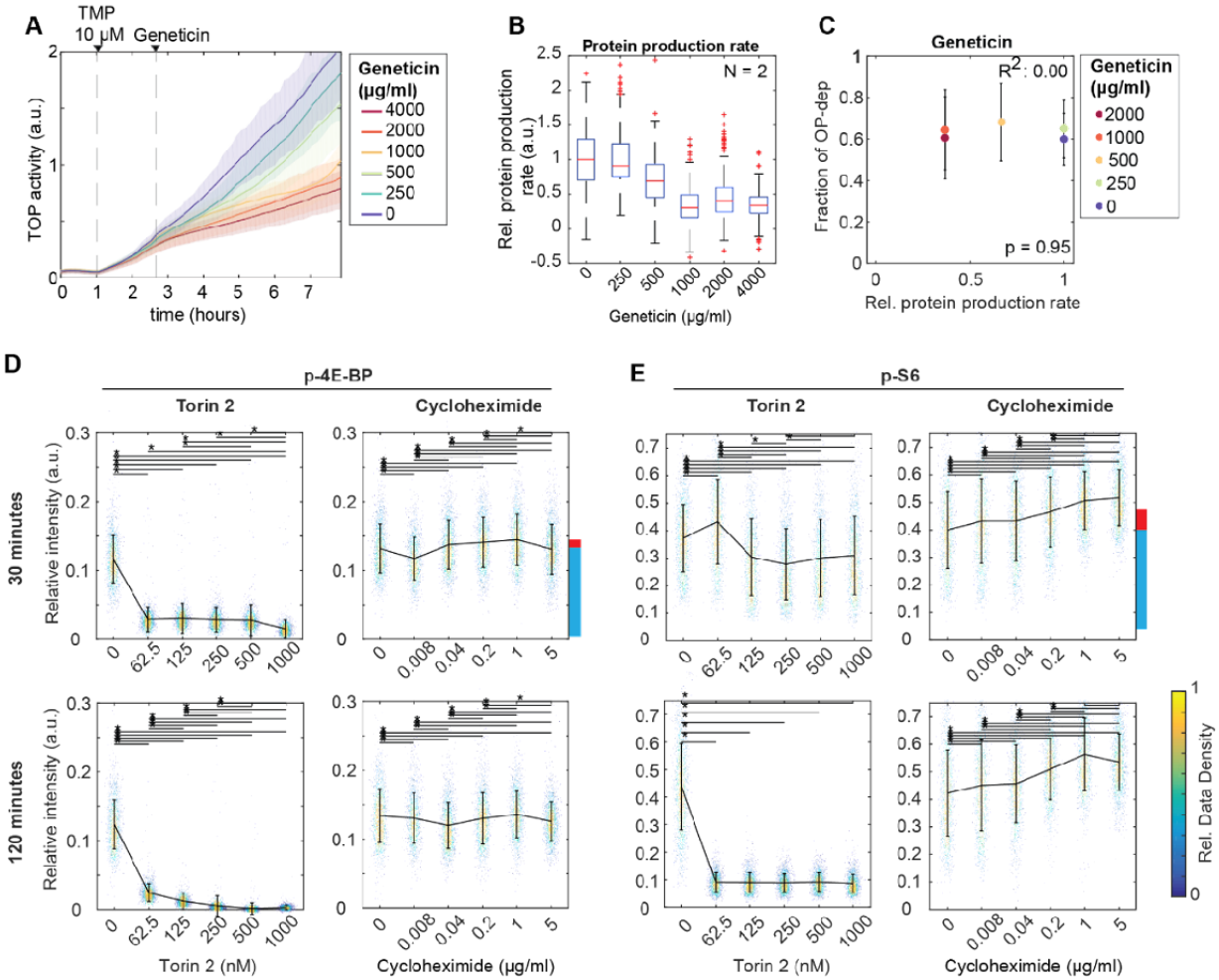

Supplemental Figure S3.6, Related to Figure 3.6

A,B: Quantification of protein synthesis rate modulation by the translation inhibitor geneticin. Plot in (A) indicates mean H2B-TOP-YFP-DD intensity for a concentration series of geneticin treatments. Shaded areas show interquartile ranges. (B) shows quantification of relative protein production rates for each concentration. Each box represents the distribution of 400 cells. N=2. C: Relationship of average protein production rate to the fraction of OP-dep cells under geneticin treatment. Protein rates measured in (A-B) are shown plotted against the corresponding OP-dep responses. While there is little decrease observed in OP-dep cells, this plot is consistent with the results obtained using CHX in Fig. 3.6.D, because geneticin treatment does not reduce protein synthesis rate as potently as CHX. However, we do note that geneticin concentrations >500 ug/ml, which suppress the protein synthesis rate moderately, are capable of terminating ongoing AMPK pulses as shown in Fig. 3.6.E, suggesting that AMPK activity is more sensitive to acute changes in protein synthesis rate than pre-existing levels. D and E: Modest stimulation of mTORC1 activity by protein synthesis inhibition. The activation of mTORC1 downstream targets were quantified by immunofluorescence for phospho-4E-BP1 (D) and phospho-S6 (E) after cells were treated with CHX at indicated dose for 30 minutes (upper panels) or 2 hours (lower panels). Treatment of cells with the mTOR inhibitor Torin2 is used to evaluate the baseline immunofluorescence level in the absence of mTORC1 activity. To compare the CHX mediated induction of mTORC1 activity to the pre-existing level of mTORC1 activity, the red bars shown to the side of the plots indicate the difference in staining observed in the absence and presence of CHX treatment at 30 minutes at the minimal dose needed to efficiently block AMPK activity (0.2 ng/ml, Fig. 3.6.E,F), while the blue bars indicate the difference in staining between untreated cells and the fully suppressed level achieved by mTORC1 inhibition for 2 hours. We find that the CHX-mediated induction of mTORC1 activity is approximately 10-20% greater than pre-existing activity, which suggests that activation of this pathway, and any subsequent modulation of glycolysis, is unlikely to account for the rapid effects of CHX on oligomycin-induced AMPK activity (Fig. 3.6.E,F). Data points show individual cell staining intensity, with mean and standard deviation shown in line plot. Stars show statistical significance with p-value < 0.05 by ANOVA test with Tukey's post hoc analysis.

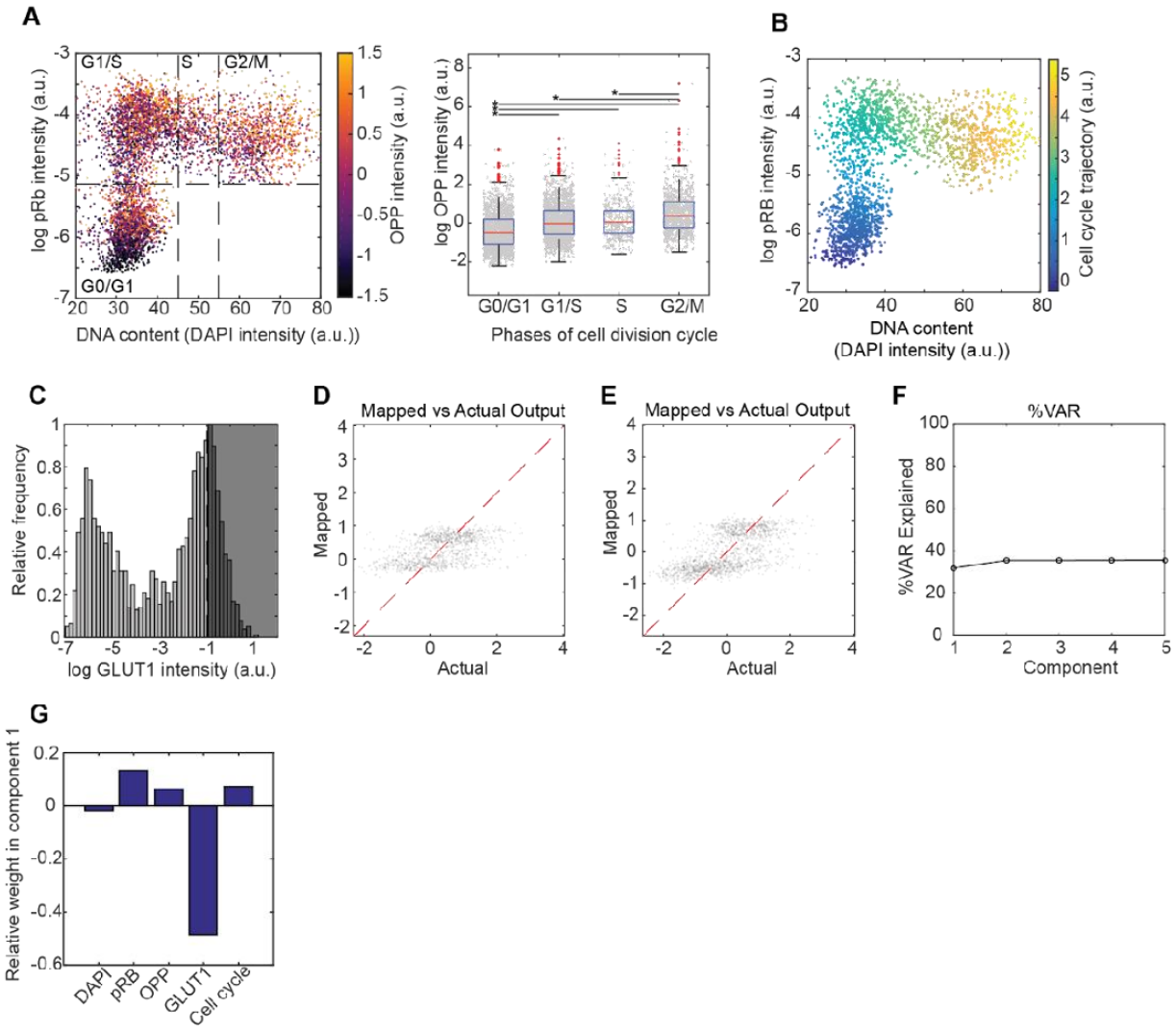

Supplemental Figure S7, Related to Figure 7

A: Left panel - scatter plot of single cell measurements of DNA content and phospho-Rb, colored by OPP labeling intensity. Cell division cycle annotations are shown as in Fig. 3.6.A. Right panel – boxplot of single cell OPP labeling intensity at each phase of the cell division cycle. Stars show statistical significance with p-value < 0.05 by ANOVA with Tukey's post hoc analysis. Gray dots show single cell data points. N=3. B: Scatter plot of single cell measurement of DNA content and phospho-Rb, colored by cell cycle trajectory as calculated using the Wanderlust algorithm. See STAR Methods for details. N=3. C: Histogram of single cell GLUT1 expression distribution as measured by NLS-mCherry intensity. The highest levels of overexpression (gray shaded area) were excluded from PLSR modelling in Figures 3.7.G, H, and I and S3.7.D, to prevent highly overexpressing cells from dominating the model. All cells are used for PLSR modelling in Figure S3.7.E,F, and G. D: Single-cell predictions of AMPKAR2Δ by PLSR plotted against measured AMPKAR2Δ, for the full model shown in Figs 3.7.G (red line) and 7H (red bar). Dashed line represents perfect prediction of the data by the model. Data used were not truncated. E,F,G: PLSR modeling of AMPKAR2Δ using all cells, without excluding high GLUT1-expressors. PLSR modeling was performed as in Fig. 3.7 but using all expression levels of GLUT1-mCherry. Results are qualitatively similar to the model with overexpressors excluded, but show a higher contribution

of GLUT1-mCherry intensity, as expected. (D) Comparison of single-cell predictions to measured AMPKAR2Δ values. (E) Variance explained by the model. (F) Contribution of each measurement to the first component of the model.

3.11. Reference

Ahn, E., Kumar, P., Mukha, D., Tzur, A., and Shlomi, T. (2017). Temporal fluxomics reveals oscillations in TCA cycle flux throughout the mammalian cell cycle. Mol Syst Biol *13*, 953.

Altschuler, S.J., and Wu, L.F. (2010). Cellular heterogeneity: do differences make a difference? Cell *141*, 559-563.

Anisimov, V.N. (2010). Metformin for aging and cancer prevention. Aging (Albany NY) *2*, 760-774.

Ashton, T.M., McKenna, W.G., Kunz-Schughart, L.A., and Higgins, G.S. (2018). Oxidative Phosphorylation as an Emerging Target in Cancer Therapy. Clin Cancer Res *24*, 2482-2490.

Bass, J., and Takahashi, J.S. (2010). Circadian integration of metabolism and energetics. Science *330*, 1349-1354.

Bendall, S.C., Davis, K.L., Amir el, A.D., Tadmor, M.D., Simonds, E.F., Chen, T.J., Shenfeld, D.K., Nolan, G.P., and Pe'er, D. (2014). Single-cell trajectory detection uncovers progression and regulatory coordination in human B cell development. Cell *157*, 714-725.

Berg, J., Hung, Y.P., and Yellen, G. (2009). A genetically encoded fluorescent reporter of ATP:ADP ratio. Nat Methods *6*, 161-166.

Buttgereit, F., and Brand, M.D. (1995). A hierarchy of ATP-consuming processes in mammalian cells. Biochem J *312 (Pt 1)*, 163-167.

Cai, L., and Tu, B.P. (2012). Driving the cell cycle through metabolism. Annu Rev Cell Dev Biol *28*, 59-87.

Cavanaugh, J.E. (1997). Unifying the derivations for the Akaike and corrected Akaike information criteria. Statistics & Probability Letters *33*, 201-208.

Cokorinos, E.C., Delmore, J., Reyes, A.R., Albuquerque, B., Kjobsted, R., Jorgensen, N.O., Tran, J.L., Jatkar, A., Cialdea, K., Esquejo, R.M.*, et al.* (2017). Activation of Skeletal Muscle AMPK Promotes Glucose Disposal and Glucose Lowering in Non-human Primates and Mice. Cell Metab *25*, 1147-1159 e1110.

Debnath, J., Muthuswamy, S.K., and Brugge, J.S. (2003). Morphogenesis and oncogenesis of MCF-10A mammary epithelial acini grown in three-dimensional basement membrane cultures. Methods *30*, 256-268.

Depaoli, M.R., Karsten, F., Madreiter-Sokolowski, C.T., Klec, C., Gottschalk, B., Bischof, H., Eroglu, E., Waldeck-Weiermair, M., Simmen, T., Graier, W.F.*, et al.* (2018). Real-Time Imaging of Mitochondrial ATP Dynamics Reveals the Metabolic Setting of Single Cells. Cell Rep *25*, 501-512 e503.

Dos Santos, C.C., Gopal, B., and Verma, S. (2018). Metformin: An Old Dog with a New Trick? Cell Metab *28*, 334-336.

Dussmann, H., Perez-Alvarez, S., Anilkumar, U., Papkovsky, D.B., and Prehn, J.H. (2017). Single-cell time-lapse imaging of intracellular O2 in response to metabolic inhibition and mitochondrial cytochrome-c release. Cell Death Dis *8*, e2853.

Elliott, S.G., and McLaughlin, C.S. (1978). Rate of macromolecular synthesis through the cell cycle of the yeast Saccharomyces cerevisiae. Proc Natl Acad Sci U S A *75*, 4384-4388.

Fan, J., Kamphorst, J.J., Mathew, R., Chung, M.K., White, E., Shlomi, T., and Rabinowitz, J.D. (2013). Glutamine-driven oxidative phosphorylation is a major ATP source in transformed mammalian cells in both normoxia and hypoxia. Mol Syst Biol *9*, 712.

Fendt, S.-M., Bell, E.L., Keibler, M.A., Olenchock, B.A., Mayers, J.R., Wasylenko, T.M., Vokes, N.I., Guarente, L., Vander Heiden, M.G., and Stephanopoulos, G. (2013). Reductive glutamine metabolism is a function of the α-ketoglutarate to citrate ratio in cells. Nat Commun *4*, 2236.

Fiehn, O. (2016). Metabolomics by Gas Chromatography-Mass Spectrometry: Combined Targeted and Untargeted Profiling. Curr Protoc Mol Biol *114*, 30.34.31-30.34.32.

Fiehn, O., Wohlgemuth, G., and Sholz, M. (2005). Setup and annotation of metabolomic experiments by integrating biological and mass spectrometric metadata. Dils *LNBI 3615*, 224-239.

Gillies, T.E., Pargett, M., Minguet, M., Davies, A.E., and Albeck, J.G. (2017). Linear Integration of ERK Activity Predominates over Persistence Detection in Fra-1 Regulation. Cell Syst *5*, 549-563 e545.

Gillies, T.E., Pargett, M., Silva, J.M., Teragawa, C.K., McCormick, F., and Albeck, J.G. (2020). Oncogenic mutant RAS signaling activity is rescaled by the ERK/MAPK pathway. Mol Syst Biol *16*, e9518.

Gowans, G.J., Hawley, S.A., Ross, F.A., and Hardie, D.G. (2013). AMP is a true physiological regulator of AMP-activated protein kinase by both allosteric activation and enhancing net phosphorylation. Cell Metab *18*, 556-566.

Griss, T., Vincent, E.E., Egnatchik, R., Chen, J., Ma, E.H., Faubert, B., Viollet, B., DeBerardinis, R.J., and Jones, R.G. (2015). Metformin Antagonizes Cancer Cell Proliferation by Suppressing Mitochondrial-Dependent Biosynthesis. PLoS Biol *13*, e1002309.

Gui, D.Y., Sullivan, L.B., Luengo, A., Hosios, A.M., Bush, L.N., Gitego, N., Davidson, S.M., Freinkman, E., Thomas, C.J., and Vander Heiden, M.G. (2016). Environment Dictates

Dependence on Mitochondrial Complex I for NAD+ and Aspartate Production and Determines Cancer Cell Sensitivity to Metformin. Cell Metab *24*, 716-727.

Gwinn, D.M., Shackelford, D.B., Egan, D.F., Mihaylova, M.M., Mery, A., Vasquez, D.S., Turk, B.E., and Shaw, R.J. (2008). AMPK phosphorylation of raptor mediates a metabolic checkpoint. Mol Cell *30*, 214-226.

Hackett, S.R., Zanotelli, V.R.T., Xu, W., Goya, J., Park, J.O., Perlman, D.H., Gibney, P.A., Botstein, D., Storey, J.D., and Rabinowitz, J.D. (2016). Systems-level analysis of mechanisms regulating yeast metabolic flux. Science *354*.

Han, K., Jaimovich, A., Dey, G., Ruggero, D., Meyuhas, O., Sonenberg, N., and Meyer, T. (2014). Parallel measurement of dynamic changes in translation rates in single cells. Nat Methods *11*, 86-93.

Hao, W., Chang, C.P., Tsao, C.C., and Xu, J. (2010). Oligomycin-induced bioenergetic adaptation in cancer cells with heterogeneous bioenergetic organization. J Biol Chem *285*, 12647-12654.

Hardie, D.G. (2014). AMPK—Sensing Energy while Talking to Other Signaling Pathways. Cell Metab *20*, 939-952.

Hardie, D.G., and Hawley, S.A. (2001). AMP-activated protein kinase: the energy charge hypothesis revisited. Bioessays *23*, 1112-1119.

Hardie, D.G., Ross, F.A., and Hawley, S.A. (2012). AMPK: a nutrient and energy sensor that maintains energy homeostasis. Nat Rev Mol Cell Biol *13*, 251-262.

Hardie, D.G., Salt, I.P., Hawley, S.A., and Davies, S.P. (1999). AMP-activated protein kinase: an ultrasensitive system for monitoring cellular energy charge. Biochem J *338 (Pt 3)*, 717-722.

Hartmann, F.J., Mrdjen, D., McCaffrey, E., Glass, D.R., Greenwald, N.F., Bharadwaj, A., Khair, Z., Verberk, S.G.S., Baranski, A., Baskar, R.*, et al.* (2020). Single-cell metabolic profiling of human cytotoxic T cells. Nat Biotechnol.

Hawley, S.A., Pan, D.A., Mustard, K.J., Ross, L., Bain, J., Edelman, A.M., Frenguelli, B.G., and Hardie, D.G. (2005). Calmodulin-dependent protein kinase kinase-beta is an alternative upstream kinase for AMP-activated protein kinase. Cell Metab *2*, 9-19.

Hensley, C.T., Faubert, B., Yuan, Q., Lev-Cohain, N., Jin, E., Kim, J., Jiang, L., Ko, B., Skelton, R., Loudat, L.*, et al.* (2016). Metabolic Heterogeneity in Human Lung Tumors. Cell *164*, 681-694.

Howell, J.J., Hellberg, K., Turner, M., Talbott, G., Kolar, M.J., Ross, D.S., Hoxhaj, G., Saghatelian, A., Shaw, R.J., and Manning, B.D. (2017). Metformin Inhibits Hepatic mTORC1 Signaling via Dose-Dependent Mechanisms Involving AMPK and the TSC Complex. Cell Metab *25*, 463-471.

Hung, Y.P., Teragawa, C., Kosaisawe, N., Gillies, T.E., Pargett, M., Minguet, M., Distor, K., Rocha-Gregg, B.L., Coloff, J.L., Keibler, M.A.*, et al.* (2017). Akt regulation of glycolysis mediates bioenergetic stability in epithelial cells. Elife *6*.

Imamura, H., Nhat, K.P.H., Togawa, H., Saito, K., Iino, R., Kato-Yamada, Y., Nagai, T., and Noji, H. (2009). Visualization of ATP levels inside single living cells with fluorescence resonance energy transfer-based genetically encoded indicators. Proc Natl Acad Sci U S A *106*, 15651-15656.

Inoki, K., Zhu, T., and Guan, K.L. (2003). TSC2 mediates cellular energy response to control cell growth and survival. Cell *115*, 577-590.

Janes, K.A., Wang, C.-C., Holmberg, K.J., Cabral, K., and Brugge, J.S. (2010). Identifying single-cell molecular programs by stochastic

profiling. Nat Methods *7*, 311-317.

Jang, C., Chen, L., and Rabinowitz, J.D. (2018). Metabolomics and Isotope Tracing. Cell *173*, 822-837.

Jaqaman, K., Loerke, D., Mettlen, M., Kuwata, H., Grinstein, S., Schmid, S.L., and Danuser, G. (2008). Robust single-particle tracking in live-cell time-lapse sequences. Nat Methods *5*, 695-702.

Kalender, A., Selvaraj, A., Kim, S.Y., Gulati, P., Brule, S., Viollet, B., Kemp, B.E., Bardeesy, N., Dennis, P., Schlager, J.J.*, et al.* (2010). Metformin, independent of AMPK, inhibits mTORC1 in a rag GTPase-dependent manner. Cell Metab *11*, 390-401.

Kim, H.S., Kim, M.J., Kim, E.J., Yang, Y., Lee, M.S., and Lim, J.S. (2012). Berberine-induced AMPK activation inhibits the metastatic potential of melanoma cells via reduction of ERK activity and COX-2 protein expression. Biochem Pharmacol *83*, 385-394.

Konagaya, Y., Terai, K., Hirao, Y., Takakura, K., Imajo, M., Kamioka, Y., Sasaoka, N., Kakizuka, A., Sumiyama, K., Asano, T.*, et al.* (2017). A Highly Sensitive FRET Biosensor for AMPK Exhibits Heterogeneous AMPK Responses among Cells and Organs. Cell Rep *21*, 2628-2638.

Li, L., Friedrichsen, H.J., Andrews, S., Picaud, S., Volpon, L., Ngeow, K., Berridge, G., Fischer, R., Borden, K.L.B., Filippakopoulos, P.*, et al.* (2018). A TFEB nuclear export signal integrates amino acid supply and glucose availability. Nat Commun *9*, 2685.

Lin, J.-R., Fallahi-Sichani, M., and Sorger, P.K. (2015). Highly multiplexed imaging of single cells using a high-throughput cyclic immunofluorescence method. Nat Commun *6*.

Lin, S.-C., and Hardie, D.G. (2017). AMPK: Sensing Glucose as well as Cellular Energy Status. Cell Metab.

Lunt, S.Y., and Vander Heiden, M.G. (2011). Aerobic glycolysis: meeting the metabolic requirements of cell proliferation. Annu Rev Cell Dev Biol *27*, 441-464.

Molina, J.R., Sun, Y., Protopopova, M., Gera, S., Bandi, M., Bristow, C., McAfoos, T., Morlacchi, P., Ackroyd, J., Agip, A.-N.A., *et al.* (2018). An inhibitor of oxidative phosphorylation exploits cancer vulnerability. Nat Med.

Mookerjee, S.A., Gerencser, A.A., Nicholls, D.G., and Brand, M.D. (2017). Quantifying intracellular rates of glycolytic and oxidative ATP production and consumption using extracellular flux measurements. J Biol Chem *292*, 7189-7207.

Myers, R.W., Guan, H.P., Ehrhart, J., Petrov, A., Prahalada, S., Tozzo, E., Yang, X., Kurtz, M.M., Trujillo, M., Gonzalez Trotter, D., *et al.* (2017). Systemic pan-AMPK activator MK-8722 improves glucose homeostasis but induces cardiac hypertrophy. Science *357*, 507-511.

O'Neill, H.M., Maarbjerg, S.J., Crane, J.D., Jeppesen, J., Jørgensen, S.B., Schertzer, J.D., Shyroka, O., Kiens, B., van Denderen, B.J., Tarnopolsky, M.A., *et al.* (2011). AMP-activated protein kinase (AMPK) beta1beta2 muscle null mice reveal an essential role for AMPK in maintaining mitochondrial content and glucose uptake during exercise. Proc Natl Acad Sci U S A *108*, 16092-16097.

Oakhill, J.S., Steel, R., Chen, Z.P., Scott, J.W., Ling, N., Tam, S., and Kemp, B.E. (2011). AMPK is a direct adenylate charge-regulated protein kinase. Science *332*, 1433-1435.

Orth, J.D., Thiele, I., and Palsson, B.O. (2010). What is flux balance analysis? Nat Biotechnol *28*, 245-248.

Pargett, M., and Albeck, J.G. (2018). Live-Cell Imaging and Analysis with Multiple Genetically Encoded Reporters. Curr Protoc Cell Biol *78*, 4.36.31-34.36.19.

Pargett, M., Gillies, T.E., Teragawa, C.K., Sparta, B., and Albeck, J.G. (2017). Single-Cell Imaging of ERK Signaling Using Fluorescent Biosensors. Methods Mol Biol *1636*, 35-59.

Quirós, P.M., Prado, M.A., Zamboni, N., D'Amico, D., Williams, R.W., Finley, D., Gygi, S.P., and Auwerx, J. (2017). Multi-omics analysis identifies ATF4 as a key regulator of the mitochondrial stress response in mammals. J Cell Biol *216*, 2027-2045.

Regot, S., Hughey, J.J., Bajar, B.T., Carrasco, S., and Covert, M.W. (2014). High-sensitivity measurements of multiple kinase activities in live single cells. Cell *157*, 1724-1734.

Ruas, J.S., Siqueira-Santos, E.S., Rodrigues-Silva, E., and Castilho, R.F. (2018). High glycolytic activity of tumor cells leads to underestimation of electron transport system capacity when mitochondrial ATP synthase is inhibited. Sci Rep *8*, 17383.

Santos, D.A., Shi, L., Tu, B.P., and Weissman, J.S. (2019). Cycloheximide can distort measurements of mRNA levels and translation efficiency. Nucleic Acids Res *47*, 4974-4985.

Settembre, C., Zoncu, R., Medina, D.L., Vetrini, F., Erdin, S., Erdin, S., Huynh, T., Ferron, M., Karsenty, G., Vellard, M.C.*, et al.* (2012). A lysosome-to-nucleus signalling mechanism senses and regulates the lysosome via mTOR and TFEB. EMBO J *31*, 1095-1108.

Shen, C.H., Yuan, P., Perez-Lorenzo, R., Zhang, Y., Lee, S.X., Ou, Y., Asara, J.M., Cantley, L.C., and Zheng, B. (2013). Phosphorylation of BRAF by AMPK impairs BRAF-KSR1 association and cell proliferation. Mol Cell *52*, 161-172.

Shi, Y., Lim, S.K., Liang, Q., Iyer, S.V., Wang, H.Y., Wang, Z., Xie, X., Sun, D., Chen, Y.J., Tabar, V.*, et al.* (2019). Gboxin is an oxidative phosphorylation inhibitor that targets glioblastoma. Nature *567*, 341-346.

Simões, R.V., Serganova, I.S., Kruchevsky, N., Leftin, A., Shestov, A.A., Thaler, H.T., Sukenick, G., Locasale, J.W., Blasberg, R.G., Koutcher, J.A.*, et al.* (2015). Metabolic plasticity of metastatic breast cancer cells: adaptation to changes in the microenvironment. Neoplasia *17*, 671-684.

Sparta, B., Pargett, M., Minguet, M., Distor, K., Bell, G., and Albeck, J.G. (2015). Receptor Level Mechanisms Are Required for Epidermal Growth Factor (EGF)-stimulated Extracellular Signal-regulated Kinase (ERK) Activity Pulses. J Biol Chem *290*, 24784-24792.

Spencer, S.L., Gaudet, S., Albeck, J.G., Burke, J.M., and Sorger, P.K. (2009). Non-genetic origins of cell-to-cell variability in TRAIL-induced apoptosis. Nature *459*, 428-432.

Stoker, M.L., Newport, E., Hulit, J.C., West, A.P., and Morten, K.J. (2019). Impact of pharmacological agents on mitochondrial function: a growing opportunity? Biochem Soc Trans *47*, 1757-1772.

Strasen, J., Sarma, U., Jentsch, M., Bohn, S., Sheng, C., Horbelt, D., Knaus, P., Legewie, S., and Loewer, A. (2018). Cell-specific responses to the cytokine TGFβ are determined by variability in protein levels. Mol Syst Biol *14*, e7733.

Suzuki, T., Bridges, D., Nakada, D., Skiniotis, G., Morrison, S.J., Lin, J.D., Saltiel, A.R., and Inoki, K. (2013). Inhibition of AMPK catabolic action by GSK3. Mol Cell *50*, 407-419.

Takanaga, H., Chaudhuri, B., and Frommer, W.B. (2008). GLUT1 and GLUT9 as major contributors to glucose influx in HepG2 cells identified by a high sensitivity intramolecular FRET glucose sensor. Biochimica et Biophysica Acta (BBA) - Biomembranes *1778*, 1091-1099.

Tantama, M., Martinez-Francois, J.R., Mongeon, R., and Yellen, G. (2013). Imaging energy status in live cells with a fluorescent biosensor of the intracellular ATP-to-ADP ratio. Nat Commun *4*, 2550.

Tasdogan, A., Faubert, B., Ramesh, V., Ubellacker, J.M., Shen, B., Solmonson, A., Murphy, M.M., Gu, Z., Gu, W., Martin, M.*, et al.* (2020). Metabolic heterogeneity confers differences in melanoma metastatic potential. Nature *577*, 115-120.

Tsou, P., Zheng, B., Hsu, C.H., Sasaki, A.T., and Cantley, L.C. (2011). A fluorescent reporter of AMPK activity and cellular energy stress. Cell Metab *13*, 476-486.

Tu, B.P., Mohler, R.E., Liu, J.C., Dombek, K.M., Young, E.T., Synovec, R.E., and McKnight, S.L. (2007). Cyclic changes in metabolic state during the life of a yeast cell. Proc Natl Acad Sci U S A *104*, 16886-16891.

Vander Heiden, M.G., and DeBerardinis, R.J. (2017). Understanding the Intersections between Metabolism and Cancer Biology. Cell *168*, 657-669.

Vashisht Gopal, Y.N., Gammon, S., Prasad, R., Knighton, B., Pisaneschi, F., Roszik, J., Feng, N., Johnson, S., Pramanik, S., Sudderth, J.*, et al.* (2019). A Novel Mitochondrial Inhibitor Blocks MAPK Pathway and Overcomes MAPK Inhibitor Resistance in Melanoma. Clin Cancer Res *25*, 6429-6442.

Vincent, L., and Soille, P. (1991). Watersheds in digital spaces: an efficient algorithm based on immersion simulations. IEEE Transactions on Pattern Analysis and Machine Intelligence *13*, 583-598.

Viollet, B., and Foretz, M. (2016). Animal Models to Study AMPK. Exp Suppl *107*, 441-469.

Wu, L., Zhou, B., Oshiro-Rapley, N., Li, M., Paulo, J.A., Webster, C.M., Mou, F., Kacergis, M.C., Talkowski, M.E., Carr, C.E.*, et al.* (2016). An Ancient, Unified Mechanism for Metformin Growth Inhibition in C. elegans and Cancer. Cell *167*, 1705-1718.e1713.

Xiao, B., Sanders, M.J., Underwood, E., Heath, R., Mayer, F.V., Carmena, D., Jing, C., Walker, P.A., Eccleston, J.F., Haire, L.F.*, et al.* (2011). Structure of mammalian AMPK and its regulation by ADP. Nature *472*, 230-233.

Xiao, Z., Dai, Z., and Locasale, J.W. (2019). Metabolic landscape of the tumor microenvironment at single cell resolution. Nat Commun *10*, 3763.

Yusa, K., Zhou, L., Li, M.A., Bradley, A., and Craig, N.L. (2011). A hyperactive piggyBac transposase for mammalian applications. Proceedings of the National Academy of Sciences *108*, 1531-1536.

Zhang, C.-S., Hawley, S.A., Zong, Y., Li, M., Wang, Z., Gray, A., Ma, T., Cui, J., Feng, J.-W., Zhu, M.*, et al.* (2017). Fructose-1,6-bisphosphate and aldolase mediate glucose sensing by AMPK. Nature *548*, 112-116.

Chapter 4

Metabolic constraints result in altered growth signaling pattern

4.1. Abstract

Mammalian cell growth requires coordination between growth cues and intracellular nutrient availability. The ERK-AKT-AMPK signaling axis has emerged as a core pathway that modulates both growth signal and cellular metabolism status. ERK and AKT signaling show highly dynamic activation-deactivation kinetics, which helps to determine cell cycle entry and metabolic activity. AMPK is an intracellular energy-sensing kinase, which senses the ratio of AMP, ADP, and ATP. AMPK is activated when ADP/AMP increases relative to ATP and signals changes in metabolic activity to increase ATP production and decrease ATP consumption. The ERK, AKT, and AMPK pathways interact through both direct phosphorylation of each others' components and through indirect regulation via changes in metabolite abundance. However, very little is known about how these cross-interactions result in changes in signaling patterns and how each pattern encodes cell fate decisions. In this study, we simultaneously measured ERK, AKT, and AMPK activity at the single-cell level. We showed that AMPK exerts multiple modes of ERK inhibition. We also showed that AKT is more likely to regulate ERK via metabolic alteration rather than direct phosphorylation. Lastly, we provide a framework for multivariate time series data exploration. Our result emphasizes the importance of metabolism in determining cell growth signaling pathway activity.

4.2. Introduction

Mammalian cell growth requires both extracellular cues and an abundance of intracellular nutrients (Mason and Rathmell, 2011; Zhu and Thompson, 2019). Cell signaling processes respond to extracellular cues, such as cell density and growth factors, to appropriately regulate cellular behaviors such as cell cycle progression and protein synthesis (Kholodenko, 2006). On the other hand, cell metabolism involves the cellular uptake of high-energy molecules such as

glucose and the breakdown of chemical bonds to generate ATP, a cellular energy currency. Cell metabolism provides chemical building blocks for biosynthetic processes such as cell proliferation and gene expression. Therefore, under mitogenic conditions, cells must coordinate both growth signal and metabolism to allow proliferation.

In fact, there are multiple studies that show this growth signal and metabolic coordination. Growth signaling kinases, such as ERK and PI3K/AKT, play a significant role in metabolic reprogramming. ERK overactivation in pancreatic tumors increases glucose uptake by 30% (Ying et al., 2012). ERBB2 overexpression, which also activates ERK, increases glycolytic flux through pyruvate dehydrogenase (PDH), by reducing PDH inhibitory kinase (PDK4) expression (Grassian et al., 2011). RAS activation also induces transcription of glycolytic flux regulating enzymes, such as Glucose transporter (GLUT1), Hexokinase (HK2), Phosphofructokinase (PFKFB3), and Monocarboxylate transporter (MCT1) (Tanner et al., 2018). ERK also indirectly controls cell metabolism through the PI3K/AKT axis and AMPK pathways. For example, ERK phosphorylates GAB1, a PI3K docking protein, which disrupts PI3K recruitment to the insulin receptor on the cell membrane, thus attenuating insulin-dependent AKT activation (Yu et al., 2002). ERK crosstalks with AMPK by phosphorylating the essential AMPK activator, liver kinase B1 (LKB1). This phosphorylation results in inhibition of both LKB1 and AMPK function (Kawashima et al., 2015). The PI3K/AKT cascade, another important cell growth signal, which is activated by the insulin receptor and other receptor tyrosine kinases, also possesses metabolic control activity. The PI3K/AKT axis regulates glucose uptake through glucose transporter (GLUT) surface expression (Manning and Toker, 2017). Key metabolic enzymes such as phosphofructokinase and pyruvate kinase are regulated through phosphorylation by PI3K/AKT (Manning and Toker, 2017). PI3K also indirectly regulates aldolase through actin modification (Hu et al., 2016). In addition, AKT regulates mTOR kinase activity, which controls the uptake and utilization of amino acids for

protein synthesis as well as the supply of intermediates for the Krebs cycle (Hoxhaj and Manning, 2020).

Cells also sense intracellular metabolite concentrations and their fluxes, which can exert control over signal transduction through multiple mechanisms. First, sensors such as AMPK sense ADP/AMP levels and adjust their kinase activity accordingly (Hardie et al., 2016). AMPK exerts it control over cell growth signals by directly phosphorylating RAF, and thus suppressing the ERK cascade (Shen et al., 2013). AKT, which regulates glycolytic function, also cross-inhibits the ERK cascade through RAF phosphorylation (Manning and Toker, 2017). The second mode of metabolic-signaling crosstalk is through direct modification of molecules by metabolites. For example, tyrosine kinase receptor, such as EGFR, requires glycosylation to be expressed on cell membrane. Glucose starvation severely diminishes ERK activity (Wellen et al., 2010). Fructose-1-6-bisphosphate also directly binds to Sos1, a RAS guanine exchange factor (GEF), which results in ERK activation (Peeters et al., 2017). Thirdly, kinases such as mTOR Complex 1 (mTORC1) integrates both growth signaling and nutrient status to facilitate cell growth. mTORC1 regulates protein translation through multiple downstream targets, such as ribosomal-S6-kinase (S6K) and eukaryotic translation initiation factor 4E (eIF4E). mTORC1 sense intracellular amino acid concentration, such as leucine (Wolfson et al., 2015) and arginine (Rebsamen et al., 2015; Saxton et al., 2016), through dedicated pathways. Apart from anabolic activity, mTORC1 can increase the catabolic state by upregulating glycolysis and autophagy (Liu and Sabatini, 2020). mTORC1 integrates glycolytic information by directly binding with hexokinase-II, which results in inhibition of autophagy (Roberts et al., 2014). These studies highlight the importance of coordination between cell signaling and cell metabolism in cell fate decisions.

The main obstacle to understanding the coordination of cell signals and cell metabolism lies in the fact that the concepts and measurements of cell signals and cell metabolism are starkly different. First, cell signaling is viewed as a quasi-steady-state process, for example, kinase

function is often considered ‘ON’ or ‘OFF’ as a level of phosphorylation status. Cell signaling measurement relies on ‘steady state’ estimation, such as protein abundance and phosphorylation status, as metrics of protein function. On the other hand, cell metabolism is a kinetic process, which we view as a ‘flow’ of biochemical molecules through ‘pipes’ of enzymatic processes. In order to reconcile these two fundamental concepts, we need to measure both cell signaling activity and metabolic state in a time-sensitive manner.

At the single-cell level, multiple studies have shown that cell signaling is highly dynamic and heterogeneous from cell to cell (Albeck et al., 2013; Aoki et al., 2013; Regot et al., 2014; Sampattavanich et al., 2018). As shown in the preceding chapter, cell metabolism also shares these characteristics. Using AMPK as a marker of metabolic state, we demonstrated that mammalian cells change their reliance on oxidative phosphorylation over time (OXPHOS), and OXPHOS dependency is determined in part by the instantaneous anabolic-catabolic balance, which is in turn affected by insulin-mediated signaling (Kosaisawe et al., 2021). By using genetically encoded fluorescent biosensors, these studies provide a tool for simultaneous cell signaling and metabolism measurement.

Genetically-encoded fluorescent biosensors allow a high temporal resolution measurement of both signaling and metabolic states of the cells. With existing translocation-based (KTR) biosensors (Regot et al., 2014), we can measure ERK and AKT (Maryu et al., 2016) function simultaneously. We can also measure AMPK kinase activity as an indicator of cellular metabolic status using the AMPKAR2 FRET sensor (Hung et al., 2017; Tsou et al., 2011). Because KTR biosensors can be linked to fluorescent proteins with minimal spectral overlap, we can co-express and simultaneously measure these signals in the same cell. The result of this approach is a high dimensional time-dataset that contains high-temporal resolution data of both pathway activity of each observing pathway and interactions between measuring pathways.

Real-time measurement of kinase activities presents multiple challenges. First, characterizing of a real-time multi-dimensional signal is not straightforward. Single-cell measurement is heterogeneous from cell to cell by nature, and it is difficult to state whether these heterogeneous signals are driven by the same underlying mechanics or not. Secondly, signals in complex systems can exhibit interactions behaviors that are delayed and non-linear. Thus it is not obvious to the observer. Even though deterministic modeling can be employed to identify some of these interactions, model parameter estimation from the sparse measurement of such a vast system will always lead to non-unique solutions, which result in an inaccurate mechanistic interpretation of the systems. In this study, we will first focus on multidimensional time-series characterization

The common approach to time series analysis is to 'featurize' time series behavior, such as amplitude, means, and frequency, and to correlate those features with the phenotype of interest, such as gene expression or cell growth (Benary et al., 2020; Foreman and Wollman, 2020; Gillies et al., 2017). Another approach is to perform time series clustering, using time series euclidean distance or dynamic time warping distance (DTW) (Ryu et al., 2016; Strasen et al., 2018), to group and align time series data together. However, these approaches are not applicable to multi-variate time series since they all lack metrics to describe inter-variate dependency. The latest framework to explore single-cell multi-variate time-series dataset is CODEX (Jacques et al., 2021), which combines time-series feature representation through a convolutional neural network (CNN) and supervised classification. However, this approach relies on knowledge about classes of data *a priori* for data representation, which limits our ability to explore the variation within the predefined classes of data . Thus to efficiently explore multi-variate time series data, first, we need a tool that can capture time series patterns and their interdependency. Secondly, we need an approach to cluster time-series in an unsupervised manner.

Autoencoder is one of the most generic methods to featurize multi-variate time series data. Autoencoder is an unsupervised neural network that learns to encode the representation of original time series data and reconstruct the original data from that encoded representation (Goodfellow et al., 2016). The combination of an autoencoder and a CNN provides a framework to extract 'features' of high-dimensional time series patterns in a bias-free manner (Aghabozorgi et al., 2015). In fact, the autoencoder approach has been applied in multiple time-series dataset settings; for example, it is used to identify abnormal sleeping patterns from real-world respirogram data and animal posture from accelerometer data (Ali et al., 2019). In theory, autoencoder is applicable to detect patterns in our dataset as well.

After time-series featurization by autoencoder, we can use clustering techniques to group similar time series together. However, the main challenges for unsupervised classification are high-dimensionality and clustering result optimization. Almost all clustering algorithms rely on the euclidean distance definition. However, in high-dimensional space, Euclidean distance is meaningless since the distances of all datapoints approach the same value (Hinneburg et al., 2000). Furthermore, there are currently no objective criteria to determine when unsupervised classification is 'complete,' which makes clustering results highly subjective. To analyze our dataset, we developed a framework for unsupervised classification based on Louvain community detection (Blondel et al., 2008) for data classification. This approach avoids using Euclidean distance definitions of similarity. We also propose a method to objectively define a stopping point for unsupervised classification, relying on the assumption that the clustering resolution is only limited only by noise in measurement (Stacey et al., 2020).

In this study, we used live-cell measurements to simultaneously measure the ERK and AKT growth signaling pathways and cell energetic status as represented by AMPK activity under metabolic stress conditions. We found that ERK responses to growth factors vary under direct AMPK activation, with at least two separate response patterns that cannot be explained by the

current signaling pathway topology. Different modes of AMPK activation also result in different distributions of ERK response patterns. Furthermore, the effect of AKT inhibition can be compensated by ERK pathway activation over a long period of time. Lastly, we provide a novel framework for unsupervised classification of multivariate time series. These findings highlight the significance of growth signaling and cell metabolism integration to determine kinase activity such as ERK. It also allows for the identification of discrepancies between actual behavior and known signaling connections, which could be used for further refinement of the topology of signaling network maps.

4.3. Results

4.3.1. Construction of multi-cistronic expression systems to express multiple fluorescence reporters in one transfection

Metabolism is one of the most fundamental cellular functions; it is integrated with all other cellular processes, including cell growth and proliferation, cell differentiation, and ultimately cell death. In fact, cell metabolism and cell signaling are intimately connected and co-regulate one another (Figure 4.1.A). We also know from multiple studies that growth signals such as ERK and PI3K-AKT axis are extremely dynamic (Albeck et al., 2013; Aoki et al., 2013; Regot et al., 2014; Sampattavanich et al., 2018). This leaves us with a key question of the role that metabolic conditions play in determining the dynamic signaling response to growth factor stimulation.

To answer this question, we need to simultaneously measure both cellular metabolic status and growth signals at the single-cell level. With the development of fluorescent biosensors in the past decade, we can now use a FRET-based AMPK sensor, AMPKAR2, to measure AMPK activity and at the same time track ERK and AKT activity using the translocation reporters ERKTR and AKT-TR, respectively (Figure 4.1.D). However, there are a few drawbacks of using fluorescent biosensors to study cell signaling. First, multiplexing is limited by spectral overlap to 4-5 fluorescent proteins per cell. Secondly, cell line construction usually requires multiple

transfections to express multiple reporters in the cell, which can introduce significant but difficult to assess genomic damage to the cell of interest. To minimize such damage, we utilized a multi-cistronic approach using self-cleaving peptides P2A and T2A to insert multiple reporters into the genome in one transfection event (Figure 4.1.B). I have shown using multiple multi-cistronic constructs that the expression of three activity reporters containing four fluorophores can be achieved (Figure 4.1.C).

However, one challenge of the P2A expression system is that P2A cleavage might not be complete. The key consideration here is that translocation reporter activity might be affected by incompletely cleaved proteins. For example, AMPKAR2 reporter contains a nuclear export sequence which might affect the AKT-KTR readout (cytosolic to nuclear ratio) if AMPKAR2 and AKT-KTR are not entirely cleaved. To validate that the function of these triple reporter cassettes, I showed that the AMPKAR2 reporter still exhibits behavior similar to previous reports when cells are treated with a glycolytic inhibitor, 2DG, and an electron transport chain inhibitor, oligomycin (Figure 4.1.E-F) (Hung et al., 2017; Kosaisawe et al., 2021). Next, I showed that ERKTR reporter translocates when cells are treated with the canonical ERK activator EGF and MEK inhibitor, PD0325901, as previously shown (Figure 4.1.G-H) (Regot et al., 2014). Finally, we also showed that the AKT-KTR reporter translocates to the nucleus as expected when cells are treated with an AKT inhibitor, MK-2206, and to the cytoplasm when cells are treated with EGF (Figure 4.1.I-J) (Maryu et al., 2016). In summary, we showed that a multi-cistronic fluorescent biosensor system is successfully expressed in MCF10A cell line, and that sensor function is preserved, as shown in earlier studies.

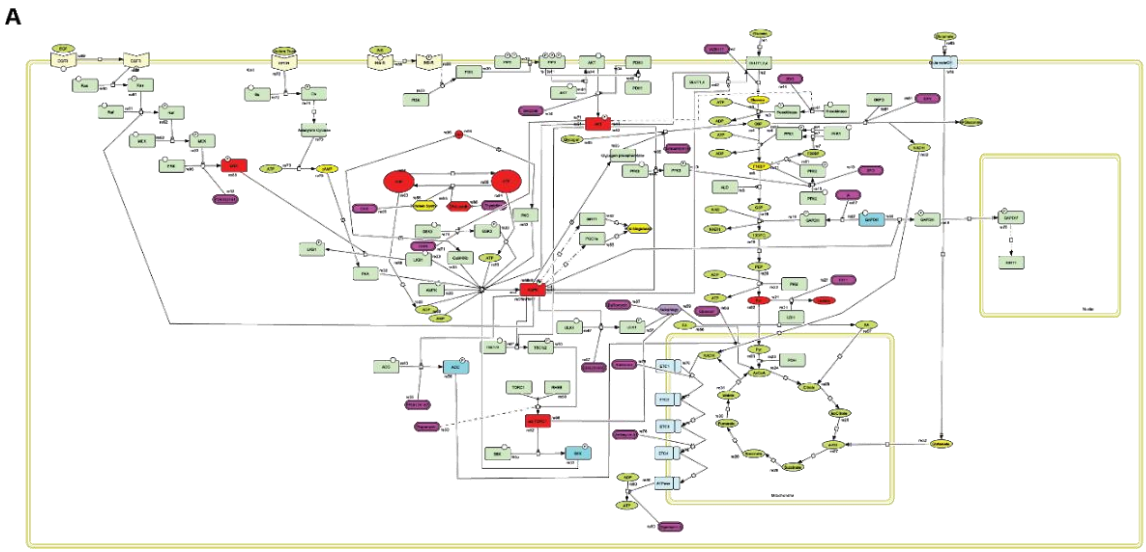
A

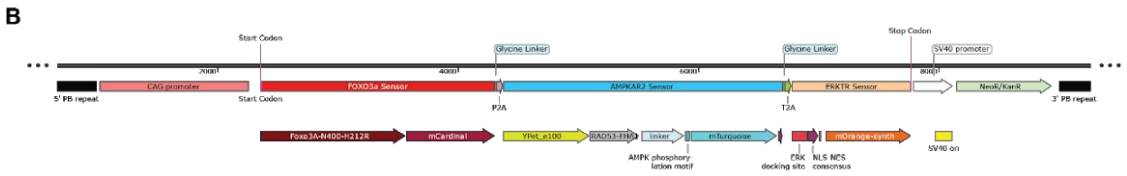
B
Start Codon
Glycine Linker
Glycine Linker
Stop Codon
SV40 promoter
5' PB repeat
CAG promoter
Start Codon
FOXO3a Sensor
P2A
AMPKAR2 Sensor
T2A
ERKTR Sensor
NeoR/KanR
3' PB repeat
Foxo3A-N400-H212R
mCardinal
YPet_e100
linker
mTurquoise
mOrange-synth
SV40 on
AMPK phosphory lation motif
ERK docking site
NLS NES consensus

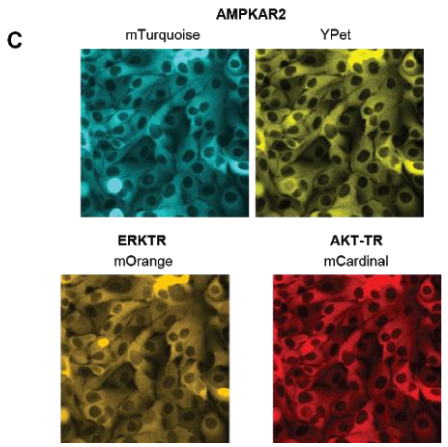
C
AMPKAR2
mTurquoise
YPet
ERKTR
mOrange
AKT-TR
mCardinal

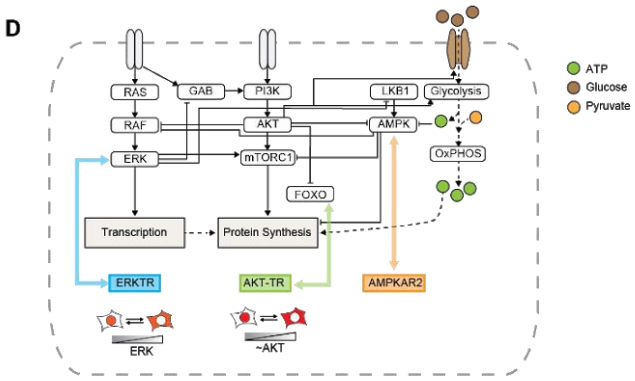
D
RAS
GAB
PI3K
LKB1
Glycolysis
RAF
AKT
AMPK
ERK
mTORC1
OxPHOS
FOXO
Transcription
Protein Synthesis
ERKTR
AKT-TR
AMPKAR2
ERK
~AKT
ATP
Glucose
Pyruvate

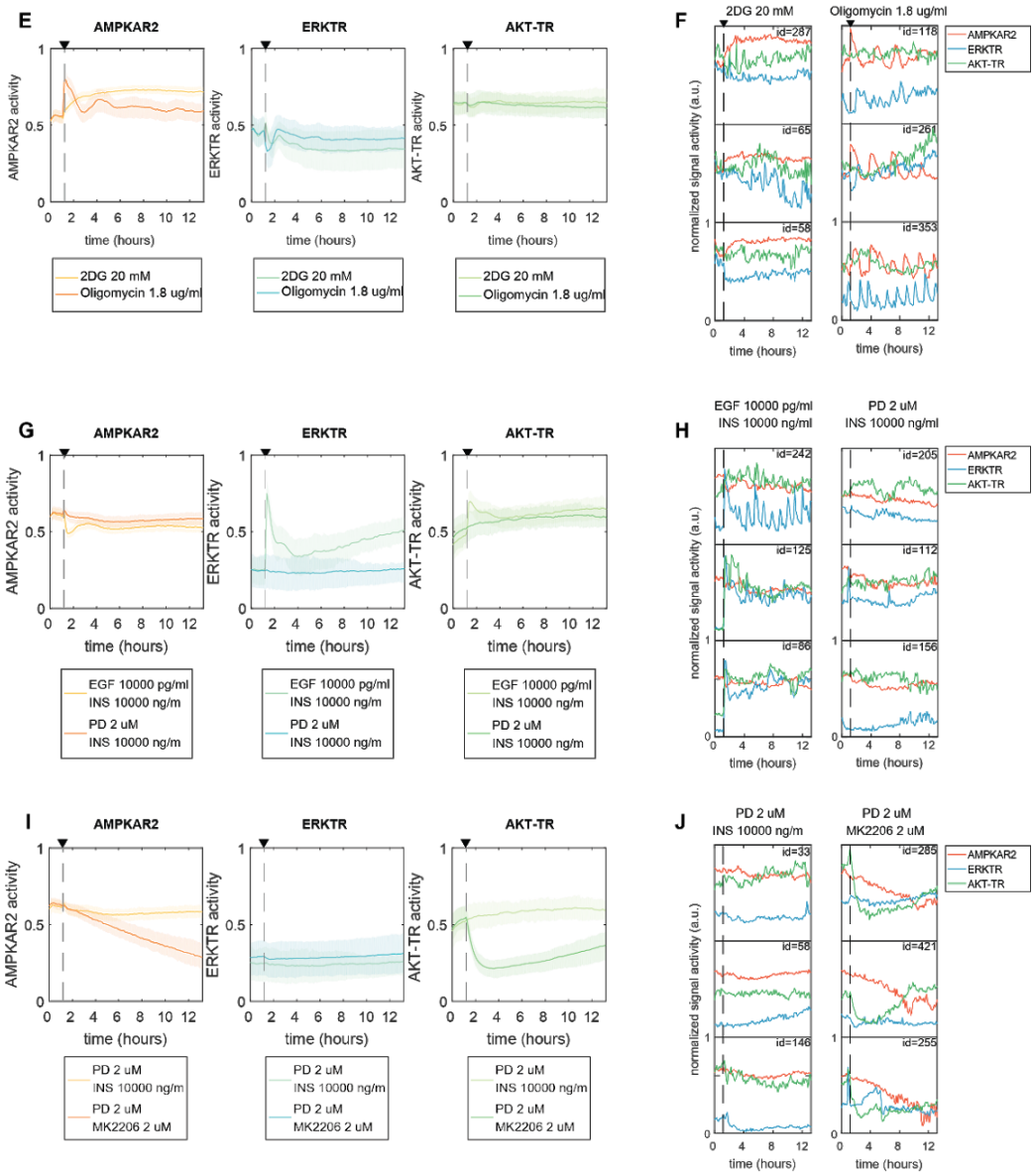

Figure 4.1 : Construction of multi-cistronic expression systems to express multiple fluorescence reporters in one transfection

A : Metabolic-cell growth signaling map adapted from KEGG (Kanehisa and Goto, 2000). Receptor tyrosine kinase are colorcoded in pale yellow. Kinase and other signaling proteins are encoded in green. Protein and metabolite that can be measured at single cell level are encoded in red. Perturbators of singaling protein or metabolic enzymes are colorcoded in purple. B.Schematic representation of triple reporter AKT-TR_AMPKAR2_ERKTR reporter systems, consisting of AKT-TR::mCardinal, AMPKAR2 and ERKTR::mOrange. They are connected by self-cleaving P2A and T2A peptides, which allow then to be expressed seperately. Right before self-cleaving peptide, glycine linkers were inserted to enhance protein cleavage. Pink lines denote start and stop codon. C. Example of MCF10A cell lines expressing AKTR-TR, AMPKAR2 and ERKTR reporter, using epifluoresence microscope. D. Simplified schematic of metabolic-cell growht signaling map, with signaling node that can be measured by indicated sensors. E-J. (E,G,I) Population average and interquartile range of corresponding reporters reponse to treatment as

indicated. (F,H,J) Sample of single-cell measurement of corresponding sensors. Triangle and dashed line indicate time when perturbation was added.

4.3.2. Temporal response of ERK-AMPK-AKT axis to growth factor is heterogeneous

To probe how metabolic conditions alter dynamic growth signals, we use MCF10A as our model since they are sensitive to growth factor manipulation. These cells require both EGF and insulin for maximal proliferation and enter quiescence when these factors are withdrawn (Worster et al., 2012; Yamanouchi et al., 1996). We stably expressed the triple reporter combination of ERKTR, AMPKAR2, and AKT-TR in MCF10A. In our experimental setup, we pre-starved cells of all growth factors and serum for 4 hours prior to the experiment to replicate low mitogenic conditions of normal tissue, and we further adjusted glucose to 5 mM to make experimental conditions more similar to physiologic glucose level. Next, we perturbed metabolic status by chemical perturbation for one hour, followed by treatment of EGF. Then we captured signaling dynamics of ERKTR, AMPKAR2, and AKT-TR for 12 hours (Figure 4.2.A). In this dataset, we mainly perturbed metabolic state through glycolysis manipulation, nutrient supplementation, and AMPK and AKT manipulation (Figure 4.2.B). In total, we have over 200 metabolic and growth conditions in our dataset and more than 300,000 single-cell traces of triple-reporter data.

One of the main challenges in understanding signaling and metabolic function is single-cell heterogeneity. For example, simple treatment with EGF 10000 pg/ml to MCF10A can generate heterogeneous ERK signaling patterns (Figure 4.2.C). Typically, it is observed that EGF treatment increases ERK activity, and to a lesser degree AKT activity, while suppressing AMPK activity (Hung et al., 2017; Worster et al., 2012). However, as shown in Figure 4.2.C, we can visually observe that there are multiple patterns of ERK, AKT, and AMPK responses to EGF. First, EGF induces sustained ERK and AKT activation and minimal AMPK suppression (Figure 4.2.C.-Top row). In another instance, EGF initially induces moderate ERK and AKT activation but with a significant initial drop in AMPK activity, followed by pulses of ERK activity with a period of about one hour (Figure 4.2.C.-Second row from the top). Thirdly, EGF can induce a large initial pulse

that lasts for about 3 hours, followed by pulses of ERK activity (Figure 4.2.C-Third row from the top). Lastly, EGF can induce only a small initial ERK pulse, followed by extended inactivity (Figure 4.2.C-Bottom row). While none of these observations are inconsistent with the current understanding of the ERK-AKT-AMPK signaling network, the current map fails to predict the heterogeneous nature of these activity dynamics. Furthermore, these data also indicate that even with one perturbation, cells have more than one response mode. All in all, these observations motivate us to build an unsupervised clustering tool to group similar time series together for data exploration.

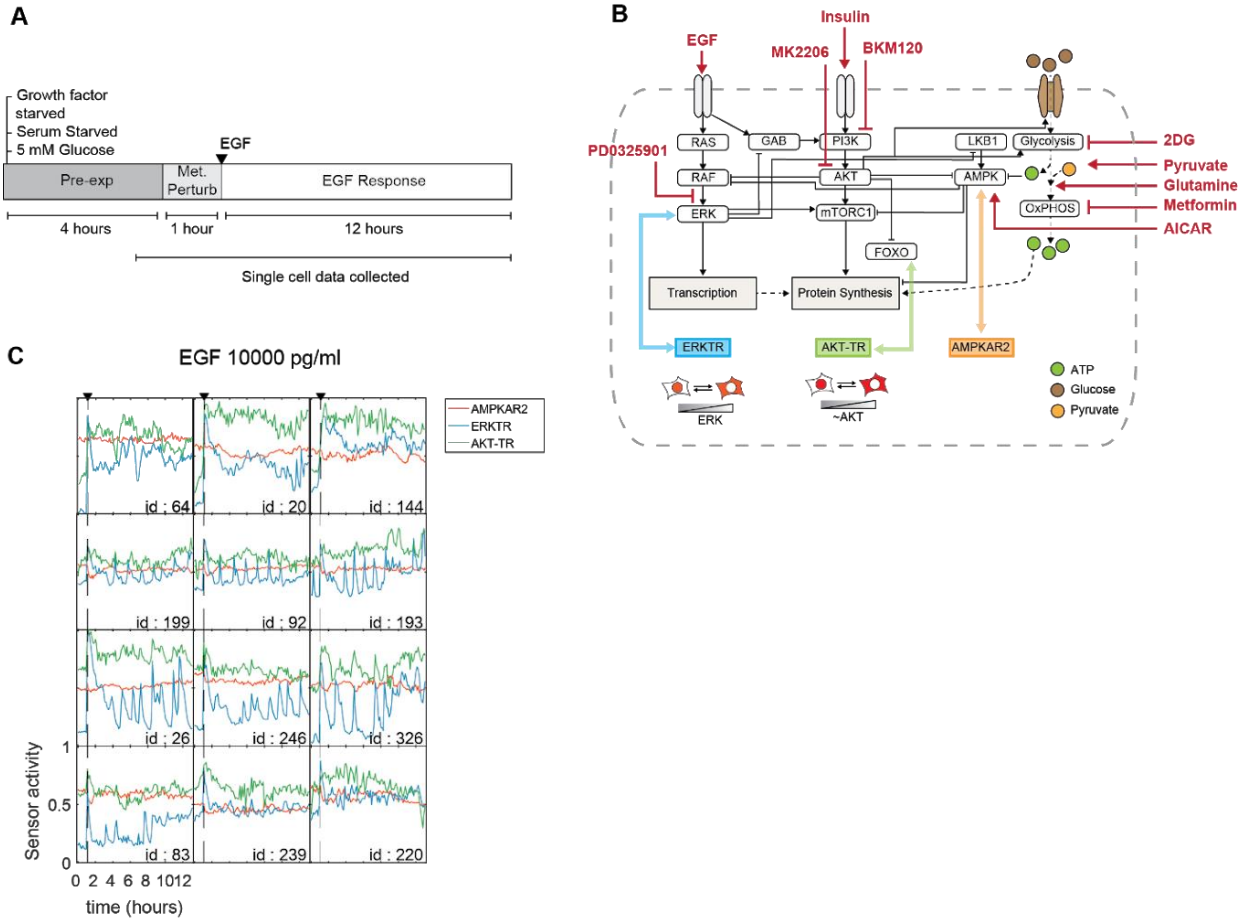

Figure 4.2. : Temporal response of ERK-AMPK-AKT axis to growth factor is heterogeneous

A. Schematic representation of experimental setup. (Pre-exp : Pre experiment; Met. Pertub. : Metabolic perturbation.). B. Simplified schematic of metabolic-cell growht signaling map, with signaling node that can be measured by indicated sensors. Metabolic perturbations used in the

dataset are shown in red. C. Example of single-cell measurement when cells are treated with EGF 10000 pg/ml. Dashed line indicates time of treatment.

4.3.3. Unsupervised time-series clustering using autoencoder and Louvain community detection to explore multidimensional time-series data

Time series data comprise time-ordered sequences of measurements. Unlike other types of data, each instance of measurement in a time series dataset is not independent of the others. This renders statistical analyses that rely on an assumption of independence less effective on time series. Intuitively, instead of treating each data point in a time series as an independent variable, we would like to consider the full-length time series as a manifestation of one or more underlying dynamical systems. To complicate our analysis further, unlike univariate time series analysis, each variable of a multivariate time series might depend on the values of the other time series. In other words, for multivariate time series analysis, metrics that capture intervariable dependency are required for an accurate description of the data.

To get around this problem, we used a machine learning (ML) architecture called a convolutional autoencoder to collect features of both multidimensional time-series patterns. In short, the convolutional autoencoder takes the original N-dimensional time series, builds a compact representational vector space, and then recreates the original time series data. The autoencoder then minimizes the error between the reconstructed time series and the original time series. The final result of autoencoder consists of K-dimensional latent vectors that are descriptive of N-dimensional time series. Theoretically, the latent vectors are orthogonal to each other (Goodfellow et al., 2016). We can then use this vector space to perform unsupervised clustering for data exploration (Figure 4.3.A).

We can find the optimal K dimension for the latent space by minimizing error in the whole dataset against the K parameters. By plotting whole dataset residuals against the size of K, we can heuristically estimate the optimal size of latent space using the elbow method (Figure 4.3.B).

For our current dataset, the optimal dimension for latent space is 50. We can show that the convolutional autoencoder faithfully recreates our original time series data (Figure 4.3.C.).

Clustering in higher dimensional space is a non-trivial problem for two reasons. First, in higher dimensional space, Euclidean distance is meaningless, which means that Euclidean-based clustering methods such as K-means are inapplicable in such space (Xia et al., 2015). Second, while clustering can be performed in a lower-dimensional projection of higher-dimensional space, we risk over-partitioning the dataset, which would result in an over-clustered solution (Cooley et al., 2019).

To avoid these problems, we converted a higher dimensional space into a graph, using the k-nearest neighbor approach. Though this approach still relies on the notion of Euclidean distance as a metric for proximity, it avoids the requirement of the user's explicit declaration of a distance that is considered 'close' (Hinneburg et al., 2000). Once data are converted into an adjacency matrix, we can use Louvain community detection (Blondel et al., 2008) to detect time-series clusters. The reason that we prefer Louvain community detection over other algorithms is because of fast implementation in Python through scikit-network. However, the main challenge of Louvain community detection is the selection of the resolution parameter, which has to be determined a priori. Another challenge to unsupervised clustering is that there is no objective optimization for a 'good' clustering result. Furthermore, real biological measurements are contaminated with measurement noise which further jeopardizes accurate classification.

Thus, the goals of our classification are first to identify an 'objective' function for the optimal resolution parameter in Louvain clustering, which in effect will determine the number of clusters in the final clustering solution, and second, to find a metric to estimate the confidence for each clustering result. To achieve this goal, we took an approach described earlier (Stacey et al., 2020). Generally, we directly add noise into feature space over M iterations and perform clustering on that perturbed dataset over different Louvain resolution parameters. We can estimate the

robustness of the clustering result by evaluating the reproducibility of clusters after noise injection in M iterations, and we called this score *repJ* (Figure 4.3.D.). After a set cluster robustness score is achieved, we then evaluate the clustering result over an array of Louvain resolution parameters, heuristically choosing the resolution by elbow method (Figure 4.3.E.). For this dataset, the optimal resolution parameter is 2.5.

After featurization and clustering, we can visualize the data by projecting the latent vector onto a 2-dimensional UMAP (McInnes et al., 2018) space. We can also overlay the confidence of clustering that belongs to the cluster for each data point (Figure 4.3.F). In total, we were able to identify 26 clusters in our dataset. Examples of each cluster were provided (Figure S4.1). We also provide the pipeline for analysis in python and graphic user interface, *tsc_gui*, for data exploration in MATLAB as well.

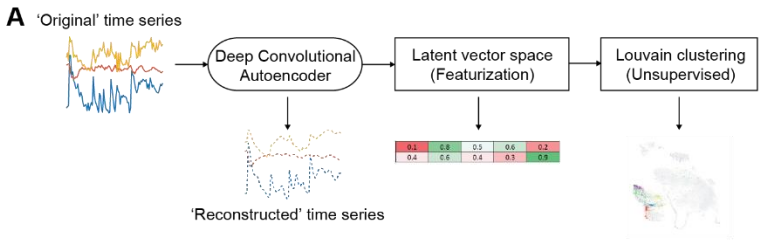
A
'Original' time series
Deep Convolutional Autoencoder
Latent vector space (Featurization)
Louvain clustering (Unsupervised)
'Reconstructed' time series

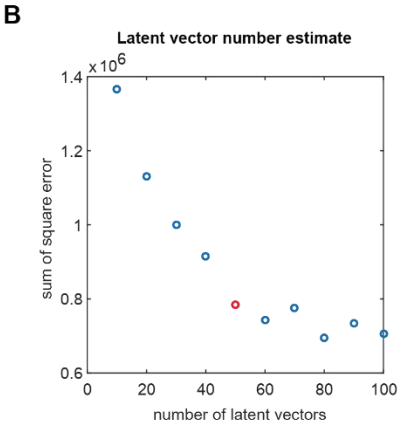
B
Latent vector number estimate
x 10^6
sum of square error
number of latent vectors

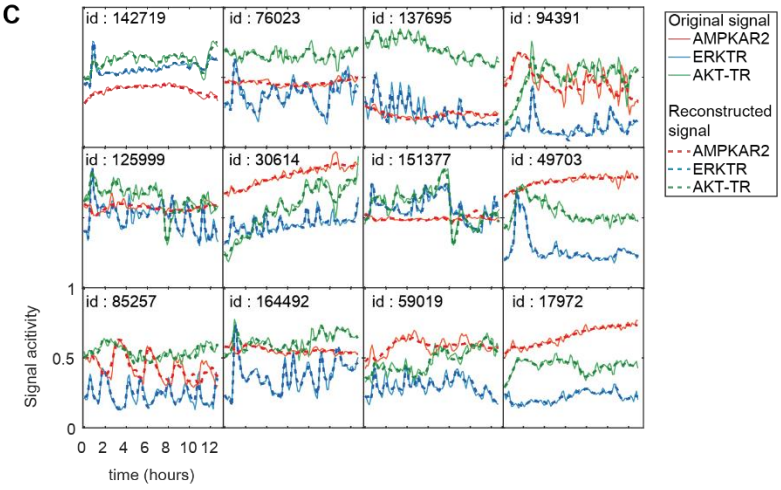
C
id : 142719
id : 76023
id : 137695
id : 94391
id : 125999
id : 30614
id : 151377
id : 49703
id : 85257
id : 164492
id : 59019
id : 17972
Signal activity
time (hours)
Original signal
AMPKAR2
ERKTR
AKT-TR
Reconstructed signal
AMPKAR2
ERKTR
AKT-TR

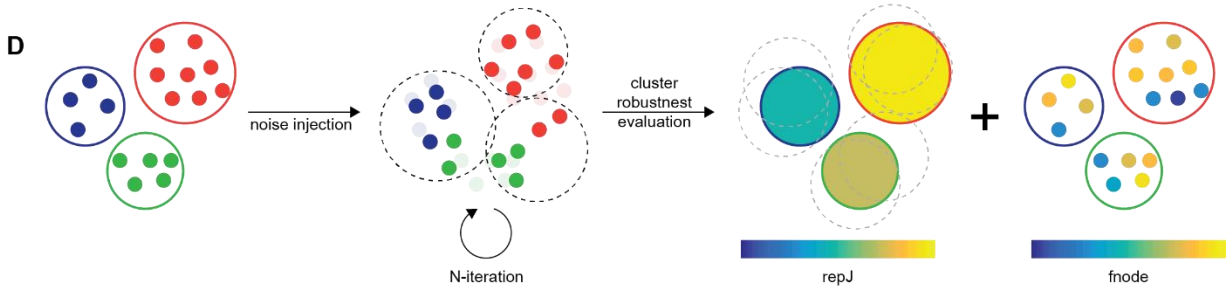
D
noise injection
N-iteration
cluster robustnest evaluation
repJ
fnode

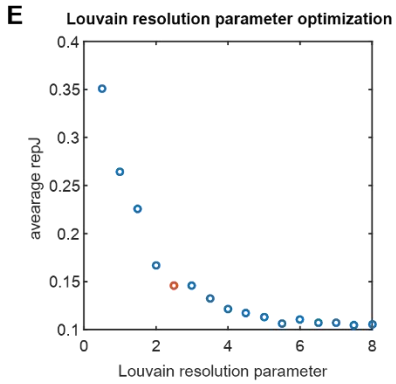
E
Louvain resolution parameter optimization
avearage repJ
Louvain resolution parameter

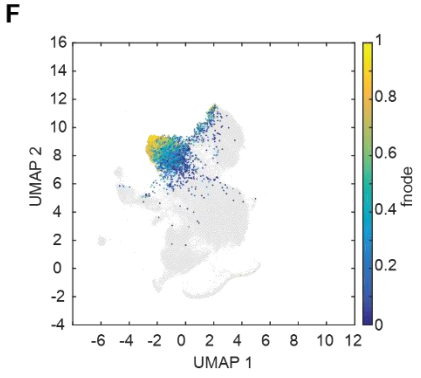
F
UMAP 2
UMAP 1
fnode

Figure 4.3. : Unsupervised time-series clustering using autoencoder and Louvain community detection to explore multidimensional time-series data

A. Schematic representation of the workflow for multi-dimensional time series analysis. B. Estimation of the size of latent vector space in autoencoder. The orange point indicates the most optimal number of latent vector space, using the elbow method. C. Sample of single-cell measurement. The dashed line represents the reconstructed time series from autoencoder. D. Schematic representation of cluster robustness estimation. Cluster reproducibility score (repJ) is the average overlap with the best match cluster across noise injection iterations. Node reproducibility score (fnode) is the frequency the datapoint appears in the best match noise-injected cluster divided by the number of iteration. E. Estimation of Louvain resolution parameter, where optimization objective is to find the resolution parameter that start to reach a saturated average repJ, using elbow method. Average repJ is the average of cluster repJ of clustering result from each resolution parameter. F. 2D UMAP projection of our dataset overlay with fnode score for each data point that belongs to the selected cluster.

4.3.4. Direct AMPK activation result in multiple modes of ERK inhibition

After clustering was performed on the data, we first explored a very simple set of experiments, where we directly activated AMPK by treating cells with AICAR, followed by ERK activation through EGF treatment (Figure 4.4.A). Theoretically, this should result in inhibition of ERK activation through RAF inhibition. However, from our data, we observe that there are at least two different forms of ERK inhibition. First, about 50% of the cell population shows initial ERK activation, followed by a long and slow decay of ERK activity over a period of 12 hours, represented by cluster 7 (Figure 4.4.B). Another 10% of the cell population shows an initial pulse of ERK activity that lasts for about 1 hour but is followed by complete inhibition of ERK until the end of the experiment, represented by cluster 5 (Figure 4.4.B). In comparison, cells that were not subjected to metabolic inhibition (Figure 4.4.C) were represented by clusters 3 and 6, which have more ‘pulsy’ ERK activity over time. Though we cannot explain mechanistically how AMPK activation results in these response patterns of ERK, this result suggests that cellular networks can have more than one dynamic response to simple metabolic stress such as direct AMPK activation.

Next, we explored whether different types of AMPK response will result in the same mode of ERK inhibition or not. We activated AMPK in two different modes. First, we used AICAR as a direct activator of AMPK, as described earlier. Secondly, we used a glycolytic inhibitor, 2-deoxyglucose (2DG) to activate AMPK indirectly. These two perturbations resulted in sustained AMPK activation, and theoretically, should result in similar ERK inhibition since AMPK is the only known direct connection between metabolic stress and the ERK pathway (Shen et al., 2013).

However, our results suggest otherwise. First, 2DG treatment results in almost all cells responding to EGF with a small initial ERK pulse followed by sustained ERK inhibition, represented by cluster 5 (Figure 4.4.D). This response is unlike AICAR, under which most of the cells exhibit an initial ERK response follow by the slow decay of ERK activity. We suspect that these differences might come from the different degrees of AMPK activation achieved by the different compounds; however AMPK activation by AICAR is higher than that of 2DG, which cannot explain why 2DG inhibits ERK signal more strongly than AICAR (Figure 4.4.E). This result suggests that glycolysis inhibition might inhibit ERK activity through an AMPK-independent pathway.

In summary, these results suggest that even though AMPK activities are similar, different forms of metabolic inhibition might have an AMPK independent method of ERK inhibition.

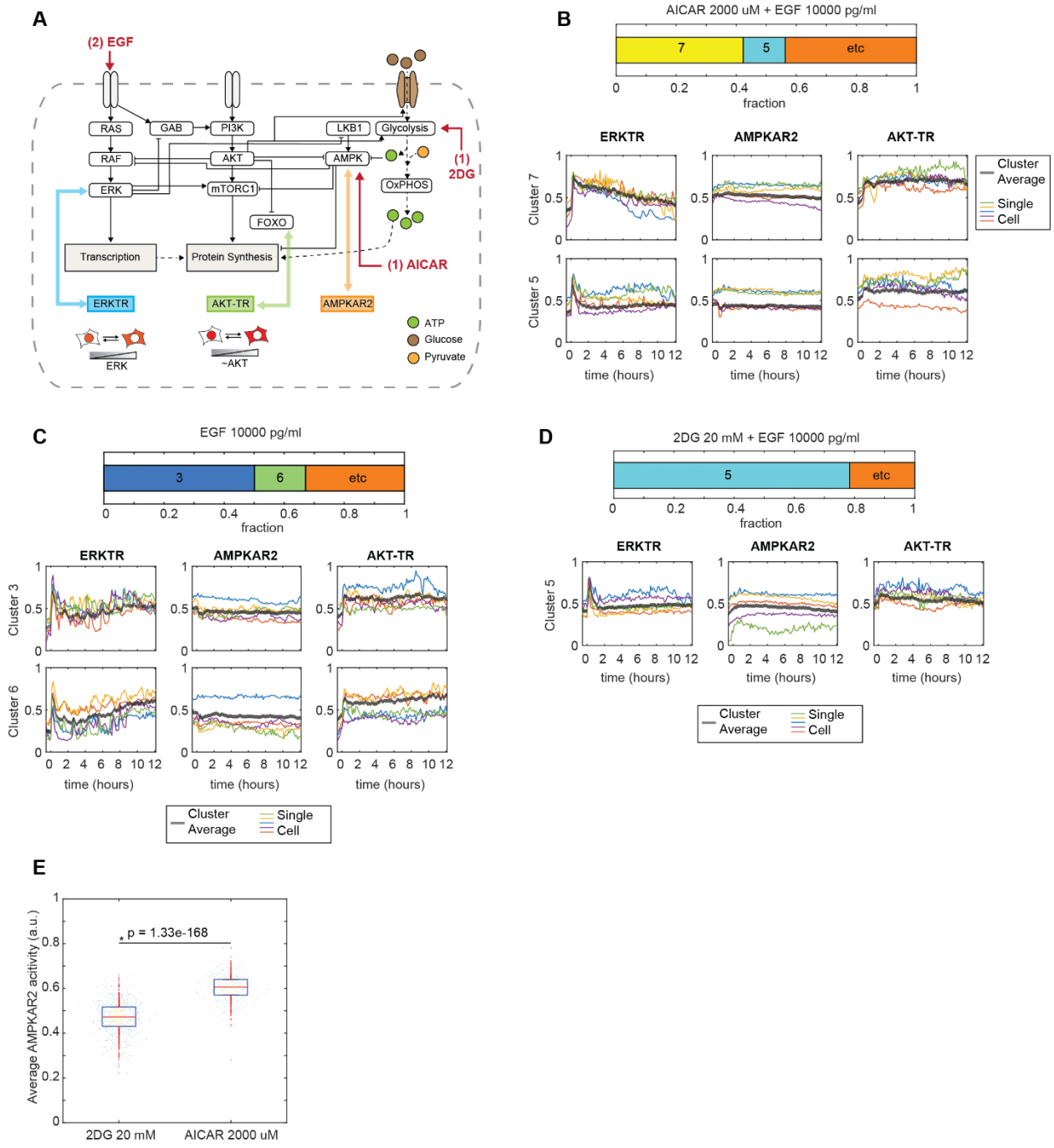

Figure 4.4 : Direct AMPK activation result in multiple modes of ERK inhibition

A.Schematic representation of metabolic-cell growht signaling map, with signaling node that can be measured by indicated sensors. Perturbations are shown in red with the order of treatment. B – C. Upper panel : cluster distribution of cells treated as indicated. Lower panels : representative

time series data for each of identified cluster. E. AMPKAR2 level caomparisong between cells treated with AICAR and 2DG at indicated concentration.

4.3.5. AKT inhibition results in transient ERK inhibition through indirect interaction

Next, we expanded our study further into AKT signals. It is thought that AKT can directly inhibit ERK through inhibitory phosphorylation of RAF (Figure 4A, Dark Blue lines) (Manning and Toker, 2017). However, activation of AKT also results in upregulation of glycolytic activity through GLUT1 surface expression and direct activation of hexokinase, among other effects (Figure 4A, Pink lines) (Manning and Toker, 2017). This situation creates a conundrum, in which if AKT inhibition can result in ERK suppression because of AMPK activation through glycolytic inhibition or in ERK activation because of the release of RAF from inhibition. To explore this space, we used the pan-PI3K inhibitor BKM120 and the allosteric AKT inhibitor MK2206, along with the activator insulin, to perturb the PI3K-AKT axis.

First, we observed that insulin does not significantly change the ERK response to EGF compared to cells not pretreated with insulin because in both cases, a majority of cells are in cluster 3. However, among cells that are pre-treated with insulin, about 20% have a much higher ERK baseline activity prior to EGF treatment, characterized by cluster 11. We also observe that cells in cluster 11 have much lower AKT responses compared to cells in cluster 3. This finding suggests that AKT activation does not significantly change ERK activation by EGF.

Next, we investigate how AKT inhibition affects ERK response to EGF by treating cells with BKM120 and MK2206. We observed that MK2206 exerts a stronger inhibition of AKT activity, as shown by AKT-KTR baseline prior to EGF treatment in cluster 6 compared to cluster 3. When comparing ERK responses between cells treated with AKT inhibitors and untreated cells, we observed that 70% of the AKT-inhibited cells have a strong initial ERK response that lasted about two hours, followed by a slow rise of ERK activity that eventually reached the peak ERK response

after about 12 hours, as identified by cluster 6. On the other hand, the majority of untreated cells belonged to cluster 3, which is characterized by an initial ERK pulse, followed by constant ERK activity after. However, there is no difference in AMPK activity detected between cluster 3 and cluster 6, which implies that the different ERK response is not dependent on AMPK activity. These two findings suggest that AKT activation does not directly inhibit ERK activity. Furthermore, when AKT is inhibited ERK activity is also diminished in the short term. But this inhibition is not sustained over the long term, as ERK activity continues to rise over a period of 12 hours.

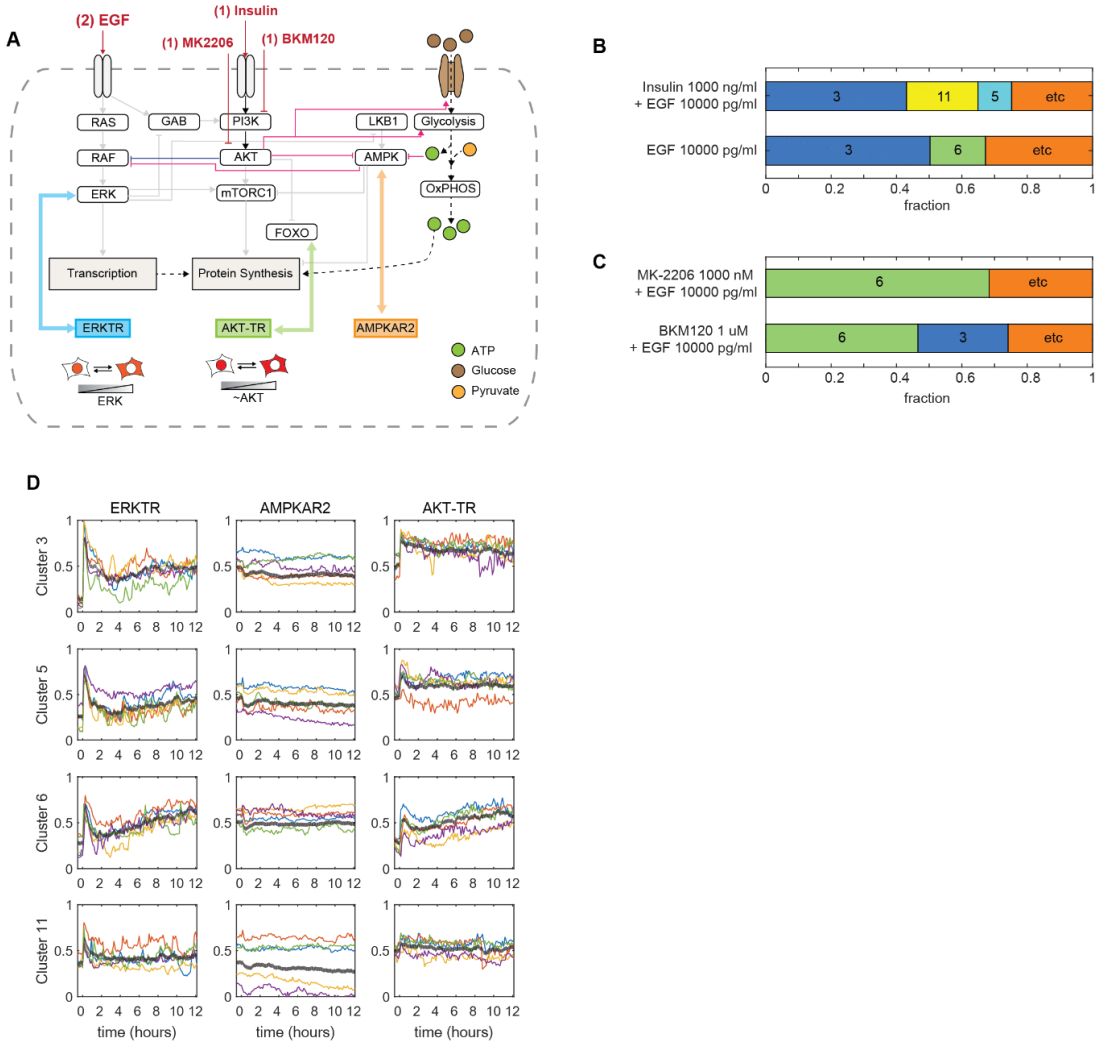

Figure 4.5 : AKT inhibition results in transient ERK inhibition through indirect interaction.

A.Schematic of the metabolic-cell growth signaling, with signaling nodes that can be measured by indicated sensors. Perturbations are shown in red with the order of treatment. B. Cluster distribution of cells treated as indicated. C. Representative time-series data for each identified cluster.

4.5. Discussion

In this study, we showed that multi-sensor expression could be achieved by using a single open reading frame with self-cleaving peptides. Thus, we can minimize genomic scars from the multiple transfection steps that are needed in single reporter expression systems. Furthermore, the multi-cassette approach yields highly expressed sensors that can be imaged at relatively high frequency and which are spectrally well-separated enough that independent measurement of individual pathways is achievable.

Though time-series dimension reduction and clustering is still a field of active research, autoencoder has become one of the most popular ‘featurization’ algorithms. The major drawback of autoencoder is that the optimization is done in L2-norm space, which implies that the features that drive time series must be able to be represented in L2-norm space as well. In other words, Autoendoer does not guarantee that its latent representation would capture the true underlying processes that drive the time series behavior. However, we are not using autoencoder as a tool for hypothesis validation; rather, we have used it as a tool for data description. Time-series clustering has also proved to be a highly active field of study. Our approach is to use the latent spaces created by autoencoder as features of time series. Then, we assume that these feature spaces are in L2-norm space so that we can create nearest neighbor graphs and use Louvain community detection to detect clusters of similar time series. This method is different from previous approaches for a few reasons. First, we avoid projecting latent feature space into a non-linear lower dimension, thus avoiding the risk of hyper-clustering. Secondly, since the Louvain clustering algorithm only needs adjacency matrix representations of graphs, it allows large dataset

clustering on desktop computers and takes a fraction of time compared to other algorithms. However, like all unsupervised clustering, the clustering result is sensitive to scaling and the number of clusters selected. In order to objectively define the best clustering result, we used an approach that was recently developed (Stacey et al., 2020). The key idea is to add noise to the original clustering space over a number of iterations; if the clustering result is 'good,' that cluster will persist across multiple noise injections. Though this method has never been used as an objective optimization function for unsupervised clustering, we think that it is a very logical approach as long as the noise injection is close to the real measurement noise.

One of the interesting experimental results of our study is that AMPK activation by AICAR results in a fast initial ERK response to EGF stimulation. However, unlike in full growth medium conditions, ERK exhibits a slow decay of activity over a period of 12 hours, rather than a fast decay of initial ERK pulses followed by periodic ERK activation later on. We don't know if this truly indicates higher ERK activity over the period of 12 hours or if it is an artifact of our sensor since we did not measure any other ERK downstream targets, such as FRA-1 or EGR-1 gene expression. We speculate that this behavior might arise from the fact that the AMPK inhibitory phosphorylation site on c-RAF is Serine-621, which is also required to be phosphorylated for Ras-mediated ERK activation. This result suggests that there might be other sites of AMPK inhibition within the ERK pathway or that the c-RAF serine-621 site has multiple functions. It is not surprising that AMPK activation by 2DG exhibits stronger ERK inhibition, as we speculate that ERK inhibition effect might also be AMPK independent, for example, due to EGF-receptor glycosylation and its surface expression (Wellen et al., 2010). Our findings provide a counterpoint to previous signaling research, in which focus has been placed on direct signaling integration mechanisms (such as AKT-RAF phosphorylation) rather than cell-wide effects due to integrated changes in cell metabolism. It is notable that in the literature, many of the functions ascribed to AKT

phosphorylation of specific targets have not used adequate controls to rule out the general effects of increasing glycolysis.

Our study also paves the way to characterize and better describe signaling network topology through real-time multi-signal observation. Using techniques like time series clustering, we can operate under the assumption that cells have limited modes of response to any perturbation. We can thus fit mathematical models to 'characteristic' cluster representatives instead of fitting data at the single-cell level, which can be unstable and resource-intensive.

4.6. Methods

4.6.1. Cell culture and media

Routine cell culture for human mammary epithelial cells, MCF10A clone 5E (Janes et al., 2010) were performed as previously described (Debnath et al., 2003). MCF10A was grown in 'DMEM/F12 growth medium' (see Media table). Primary stocks from the original clonal derivation (MCF10A-5E) was used in all experiments. Cells were routinely split when they are ~80% confluent.

In live microscopy experiments, we used a custom formulation, termed 'imaging base-DMEM/F12', which consists of DMEM/F12 lacking glucose, glutamine, riboflavin, folic acid, and phenol red (Life Technologies or UC Davis Veterinary Medicine Biological Media Service) which allows adjustment of available nutrients and avoids fluorescence background. 'Imaging medium' was used for all experiments (see Media composition). Before imaging, cells were washed twice with their respective media and then cultured in imaging experiment media at least 4 hours prior to imaging, unless indicated otherwise. The cell to media ratio was maintained at 150-200 cells/µl for all experiments.

4.6.2. Media composition

DMEM/F12 growth media

Component	Vendor	Catalog number	Final Concentration
DMEM/F2	Gibco	11320-033	-
Horse Serum	Invitrogen	16050-122	5%
EGF	Peprotech	AF-100-15	20 ng/ml
Hydrocortisone	Sigma	H0888	0.5 mg/ml
Cholera toxin	Sigma	C8052	100 ng/ml
Insulin	Sigma	I9278	10 ug/ml

Imaging medium

Component	Vendor	Catalog number	Final Concentration
Imaging base-DMEM/F12	Gibco	Custom; equivalent to Gibco 11320-033 lacking glucose, glutamine, pyruvate, riboflavin, folic acid, and phenol red	-
D-glucose	Fisher	D16	5 mM
BSA	Invitrogen	16050-122	0.1% w/v
Hydrocortisone	Sigma	H0888	0.5 mg/ml
Cholera toxin	Sigma	C8052	100 ng/ml
Penicillin-Streptomycin	Gibco	15140122	100 U/ml

4.6.3. Reporter construction

The reporters AMPKAR2 (Hung et al., 2017b; Kosaisawe et al., 2021), AKT-TR (Maryu et al., 2016; Sampattavanich et al., 2018), and ERKTR (Regot et al., 2014) sequences were previously described. We used a commercial synthesis service to build AKT-

TR_AMPKAR2_ERKTR construct and cloned it into a vector compatible with piggyBac transposase-mediated delivery (Yusa et al., 2011) to minimize recombination between all fluorophores. All plasmids were confirmed by sequencing.

4.6.4. Reporter Delivery

Cell lines stably expressing biosensors were generated by retroviral transduction or transfection with the PiggyBac transposase system. PiggyBac plasmids were delivered by electroporation (Neon Electroporation systems, Thermo Scientific). The ratio between piggyBac plasmid and HypBase was 8:1 μg. After transfection or transduction, cells were selected with geneticin (300 μg/ml); single-cell clones were made by flow cytometry sorting, maximize the fluorophore expression in all four channels. We isolated multiple stable clones with homogenous expression; data reported in this study reflect representative behaviors that were consistent across clones for each reporter line. All reporter cell lines were confirmed to be mycoplasma-negative by PCR; results were validated by third-party testing of selected lines (ATCC).

4.6.5. Live-cell fluorescence microscopy

Time-lapse wide-field microscopy was performed as described previously (Hung et al., 2017b; Pargett et al., 2017). Briefly, 10000 cells were spotted one day prior to imaging in glass-bottom 96-well plates (Cellvis P96-1.5H-N, Mountain View, CA) pretreated with type I collagen (Gibco A10483-01) to promote cell adherence. For experiments with drug addition, cells were placed in an imaging medium until the addition of the drug. For drugs dissolved in DMSO, the final DMSO concentration was <0.1%. Cells were maintained in 95% air and 5% CO_2 at 37℃ in an environmental chamber. Images were collected with a Nikon (Tokyo, Japan) 20/0.75 NA Plan Apo objective on a Nikon Eclipse Ti inverted microscope, equipped with a Lumencor SOLA or Lumencor SPECTRA X light engine. Fluorescence filters used in the experiment are: DAPI (custom ET395/25x - ET460/50m - T425lpxr, Chroma), CFP (49001, Chroma), YFP (49003,

Chroma), Cherry (41043, Chroma), mOrange (49014, Chroma) and Cy5 (49006, Chroma). For AMPKAR2 biosensors, CFP and YFP filters were used to acquire images. Images were acquired using Andor Zyla 5.5 scMOS camera every 8 minutes with 2x2 binning. Exposure times for each channel were 25-50 ms for DAPI; 150 – 250 ms for CFP; 150 – 250 ms for YFP; 150-250 ms for mOrange; 300 – 500 ms for Cherry and 300 – 500 ms for Cy5.

4.6. QUANTIFICATION AND STATISTICAL ANALYSIS

4.6.1. Image processing

After background subtraction and flat field correction, image data were processed to segment and average pixels within each identified cell's nucleus and cytoplasm, using a custom procedure written for MATLAB (Pargett et al., 2017), with modifications in the cytosolic identification protocol as described below. Image data were stored in ND2 files generated by NIS Elements and accessed using the Bio-Formats MATLAB toolbox. Individual cells were tracked over time using uTrack 2.0 (Jaqaman et al., 2008). Cytoplasmic masks were created by watershed method using cytosolic YFP to identify the cytosolic boundary. The cytosolic area is further restricted to the area within 5 pixels of the nuclear border. The resulting single-cell time series traces were filtered for quality by a minimum length of trace and maximum number of contiguous missing or corrupt data points.

4.6.2. Sensor calibration and normalization

For the AMPKAR2 reporter, AMPKAR2 phosphorylation status was calculated using the protocol described (Kosaisawe et al., 2021). Briefly, linearized AMPKAR2 FRET efficiency was calculated as shown in our previous work (Gillies et al., 2020). Then AMPKAR2 phosphorylation status was estimated based on this equation

$$AMPKAR2^{PHOS} = 2.74[AMPKAR2_{FRET\ ratio}\ ] - 0.59$$

For ERKTR and AKT-TR, data from each experiment were normalized to maximal and minimal responses possible for each sensor. For maximal ERKTR and AKTTR response, we treat cells with a combination of EGF 10000 pg/ml and insulin 10000 ng/ml, respectively. For minimal ERKTR and AKTTR response we treated cells with a combination of PD0325901 1 mM and MK-22006 1 mM, respectively.

4.6.3. Time series analysis

Pre-Processing

All time-series were first normalized as described in the previous section. Then each time series were mean subtracted before passing into deep convolutional autoencoder (DCAE). All time-series in the analyzed dataset have the same number of time steps and time intervals.

Deep Convolutional Autoencoder (DCAE)

The main purpose of DCAE is to reduce the dimension of time series and create a non-linear representation of time series (Ali et al., 2019). DCAE in this study was built in Python 3.7, using TensorFlow API (Version 2.4). The architecture of DCAE is similar to a previous study (Ali et al., 2019) and is shown in Data Analysis Table 1. DCAE is composed of 3 parts: encoding, latent representation, and decoding. The shape of the input depends on the number of time steps and the dimensions of time series that are fed into the model. In the encoding part, there are three 2D-convolution layers so that the model can learn local representation in both time and order of time series. Then parameters from convolutional layers are flattened and passed to fully connected layer so that the model can learn about long-term time effects. In the latent representation layer, output from the fully connected layer is compressed to the size that the user has defined. Then, these latent vectors are decoded through three 2D-convolution layers and reshaping to return the reconstructed time-series that has the same shape as the input time series. The loss function used in DCAE is mean squared error (MSE), and the optimization is through minimizing MSE of reconstructed time series and original time series. The Adam

optimizer was used. All models were trained to minimize MSE with an L2 regularization weighted at 1e-10.

The size of latent vector space can be optimized by running the DCAE model through different sizes of latent vector space. The optimal number of latent vectors can be estimated when the total model error reaches a salient point, as identified by the elbow plot (Figure 4.3.B.).

Data Analysis Table 1

Layers	Shape	Filter size	Number of Kernels	Number of Unit	Activation
Input	TTS x DTS				
2D Convolution	40 x (2,2)	2x2	40		Relu
2D Convolution	20 x (2,2)	2x2	20		Relu
2D Convolution	10 x (2,2)	2x2	10		Relu
Flatten					
Dense				100	Relu
Dense				**N**	**Linear**
Dense				100	Relu
Reshape	10 x (2,2)				
2D Convolution	10 x (2,2)	2x2	10		Relu
2D Convolution	20 x (2,2)	2x2	20		Relu
2D Convolution	40 x (2,2)	2x2	40		Relu
Output	TTS x DTS				Linear

TTS - time step of time series
DTS - dimension of time series
N – size of latent vectors; user defined

Training and validation

Eighty percent of the dataset was randomly selected to use for training, and the remaining 20% of the dataset was used for model validation. Stopping criteria was set when ‘loss’ does not change for three epochs.

UMAP projection

UMAP projection of latent representation was performed with Python implementation of UMAP (UMAP).

Unsupervised clustering using Louvain community detection

For unsupervised clustering, we first convert latent vector representation of time series from DCAE into K-nearest neighbor graph (K = 5) using Faiss API in python. The adjacency matrix was then fed into the Python implementation of Louvain community detection in SciKit-Network (version 0.24).

Unsupervised classification by Louvain community detection has two challenges. First, Louvain resolution parameter selection has to be determined *a priori*, which will affect the size of the final clustering outcome. Secondly, for all unsupervised clustering, there is no objective optimization function for a 'good' clustering result.

To this end, we took a cluster perturbation approach described earlier in the text. The process can be described as follows

1. We performed Louvain clustering on the original dataset, using the following range of Louvain resolution parameters (Resolution : [0, 0.5, 1, 1.5, 2, 2.5, 3, 3.5, 4, 4.5, 5, 5.5, 6, 6.5, 7, 7.5, 8]).
2. Uniform normal distribution noise at 10% of original data. We iterated this process 10 times. We call the noise-added data the 'perturbed dataset'. The type and degree of noise are chosen as suggested in Stacey et al.
3. Louvain clustering was performed on each perturbed dataset, using a range of resolution parameter described in (1).
4. Once we have clustering results from the original and perturbed datasets, we have to determine the similarity of these datasets. We used the Jaccard index (J_i), which is the number of nodes in common between two clusters divided by total number of unique nodes in the two clusters (see equation below).

$$J_i = max_j \left(\frac{overlap(cluster1_i, cluster2_j)}{union(cluster1_i, cluster2_j)} \right)$$

Where cluster 1 is the perturbed cluster set; cluster 2 is the original cluster set; $cluster1_i$ and $cluster2_j$ are single clusters from those sets.

The matched clusters from perturbed and original datasets are identfied by clusters that maximize J_i. Then for each cluster identified in the original dataset, it contains in total N numbers of J_i, where N is the number of noise addition iteration. We can estimate the reproducibility of each cluster by calculating the average J_i (repJ) for each cluster.

$$repJ = \frac{\sum_{i=1}^{N} J_i}{N}$$

5. To choose the right resolution parameter, we then calculate the average repJ for each resolution level and identify the optimal resolution parameter by elbow method (Figure 4.3.E.).
6. Once the right level of resolution parameter is obtained, we discard any cluster that has repJ below the cutoff of 0.1 (set arbitrarily).

4.6.4. Distributions and statistical tests

Statistical tests, including ANOVA, t-tests, and Pearson's correlations, were performed using standard functions in MATLAB. Box and whisker plots show the median value (red line), interquartile range (box), range (whiskers), and outliers (plus symbols).

4.7. Supplementary Materials

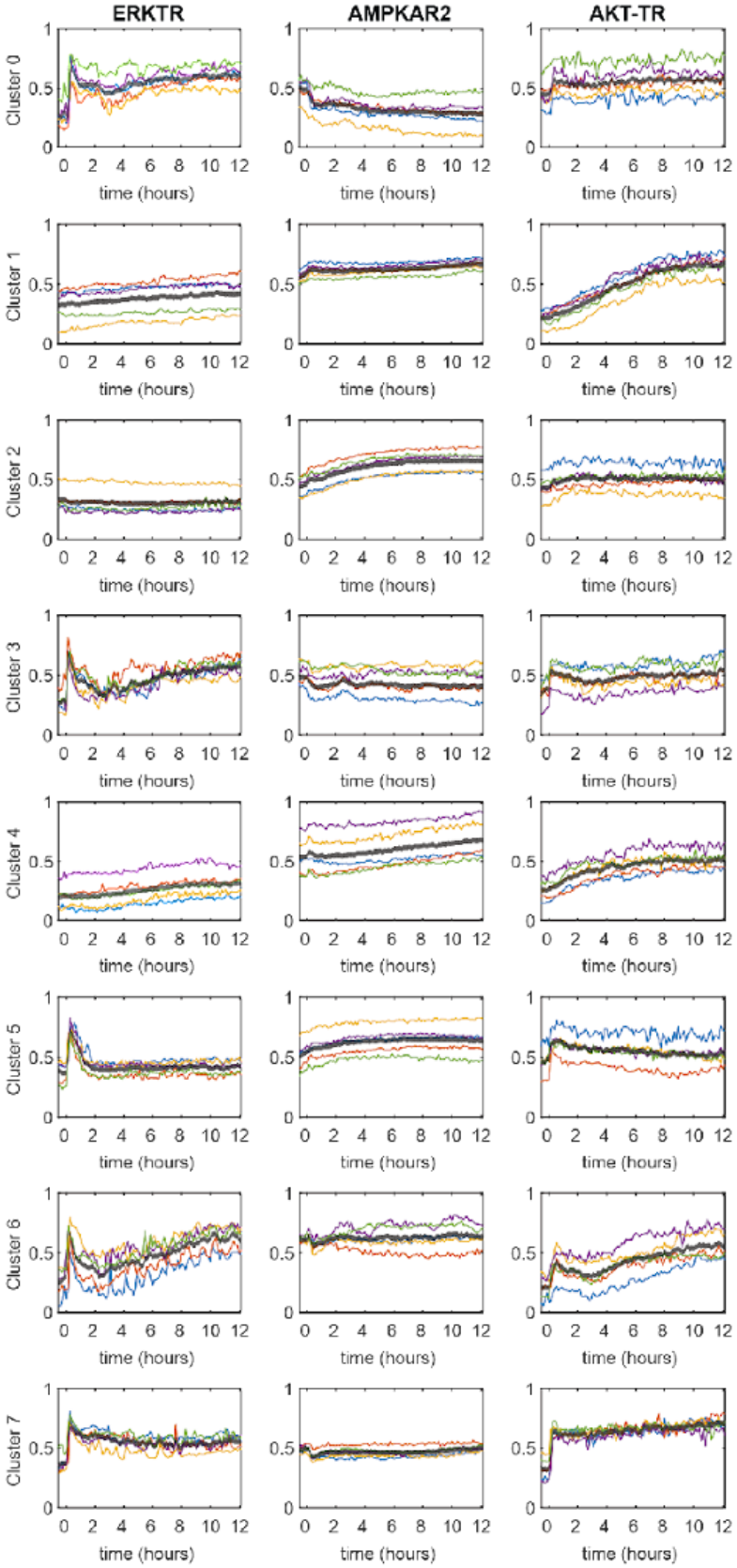

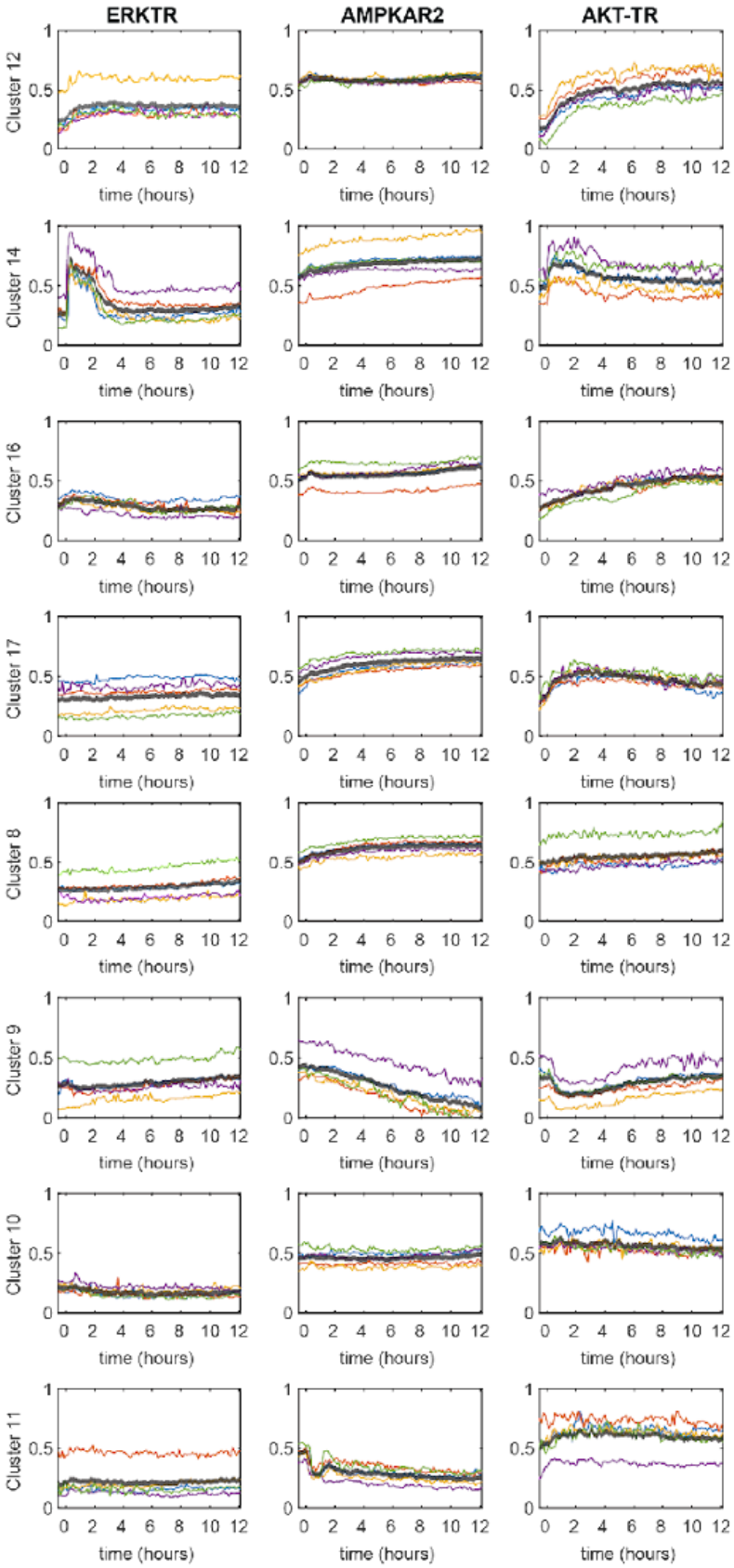
ERKTR
AMPKAR2
AKT-TR
Cluster 12
Cluster 14
Cluster 16
Cluster 17
Cluster 8
Cluster 9
Cluster 10
Cluster 11
time (hours)
0 2 4 6 8 10 12
0 0.5 1

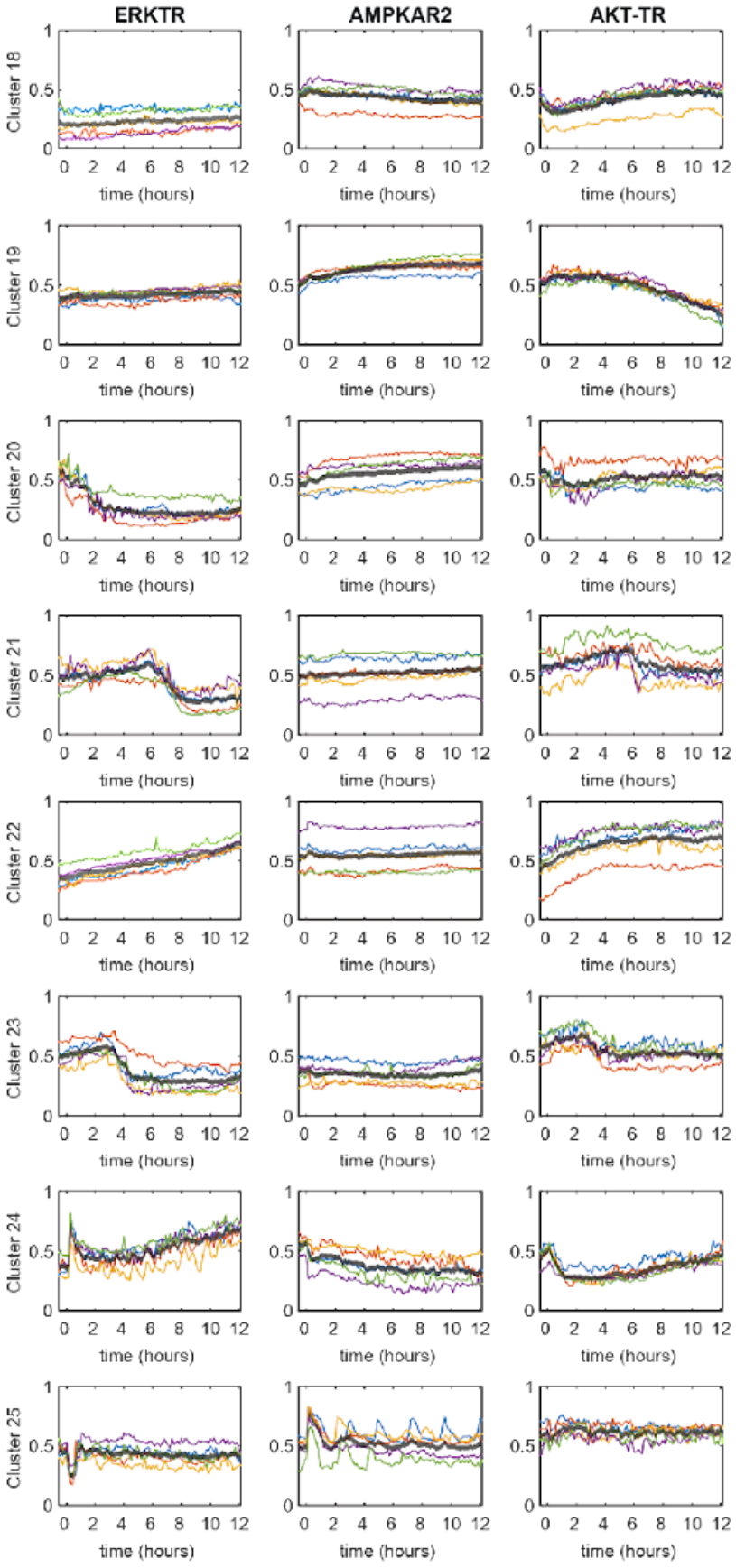
ERKTR
AMPKAR2
AKT-TR
Cluster 18
Cluster 19
Cluster 20
Cluster 21
Cluster 22
Cluster 23
Cluster 24
Cluster 25
time (hours)

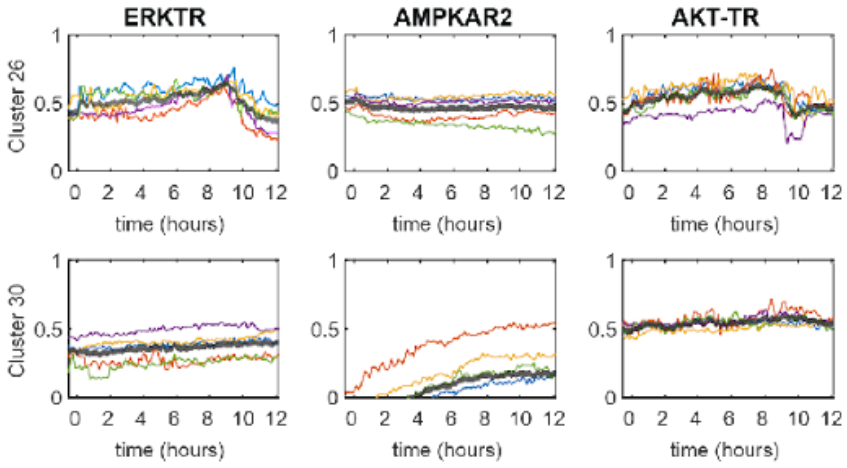

Figure S4.1. : Example of all clusters identified in current dataset

Each row of panels, represents an example of time series that belongs to corresponding cluster, indicate y-axis label. Thick black lines, represent average time series behavior corresponding to the type of signals and clusters as indicated. Color lines are single cell time series examples of each clusters and signals.

4.8. Reference

Aghabozorgi, S., Seyed Shirkhorshidi, A., and Ying Wah, T. (2015). Time-series clustering - A decade review. Inf. Syst. *53*, 16–38.

Albeck, J.G., Mills, G.B., and Brugge, J.S. (2013). Frequency-modulated pulses of ERK activity transmit quantitative proliferation signals. Mol Cell *49*, 249–261.

Ali, M., Jones, M.W., Xie, X., and Williams, M. (2019). TimeCluster: dimension reduction applied to temporal data for visual analytics. Vis. Comput. *35*, 1013–1026.

Aoki, K., Kumagai, Y., Sakurai, A., Komatsu, N., Fujita, Y., Shionyu, C., and Matsuda, M. (2013). Stochastic ERK activation induced by noise and cell-to-cell propagation regulates cell density-dependent proliferation. Mol. Cell *52*, 529–540.

Benary, M., Bohn, S., Lüthen, M., Nolis, I.K., Blüthgen, N., and Loewer, A. (2020). Disentangling Pro-mitotic Signaling during Cell Cycle Progression using Time-Resolved Single-Cell Imaging.

Cell Rep. *31*.

Blondel, V.D., Guillaume, J.L., Lambiotte, R., and Lefebvre, E. (2008). Fast unfolding of communities in large networks. J. Stat. Mech. Theory Exp. *2008*, 0–12.

Cooley, S.M., Hamilton, T., Deeds, E.J., and Ray, J.C.J. (2019). A novel metric reveals previously unrecognized distortion in dimensionality reduction of scRNA-Seq data. BioRxiv 689851.

Debnath, J., Muthuswamy, S.K., and Brugge, J.S. (2003). Morphogenesis and oncogenesis of MCF-10A mammary epithelial acini grown in three-dimensional basement membrane cultures. Methods *30*, 256–268.

Foreman, R., and Wollman, R. (2020). Mammalian gene expression variability is explained by underlying cell state. Mol. Syst. Biol. *16*, 1–13.

Gillies, T.E., Pargett, M., Minguet, M., Davies, A.E., and Albeck, J.G. (2017). Linear Integration of ERK Activity Predominates over Persistence Detection in Fra-1 Regulation. Cell Syst. *5*, 549-563.e5.

Gillies, T.E., Pargett, M., Silva, J.M., Teragawa, C.K., McCormick, F., and Albeck, J.G. (2020). Oncogenic mutant RAS signaling activity is rescaled by the ERK/MAPK pathway. Mol. Syst. Biol. *16*, e9518.

Goodfellow, I., Benigo, Y., and Courville Aaron (2016). Deep Learning (Adaptive Computation and Machine Learning series): Ian Goodfellow, Yoshua Bengio, Aaron Courville: 9780262035613: Amazon.com: Books. MIT Press.

Grassian, A.R., Metallo, C.M., Coloff, J.L., Stephanopoulos, G., and Brugge, J.S. (2011). Erk regulation of pyruvate dehydrogenase flux through PDK4modulates cell proliferation. Genes Dev. *25*, 1716–1733.

Hardie, D.G., Schaffer, B.E., and Brunet, A. (2016). AMPK: An Energy-Sensing Pathway with

Multiple Inputs andOutputs. Trends Cell Biol. *26*, 190–201.

Hinneburg, A., Aggarwal, C.C., and Keim, D.A. (2000). What is the nearest neighbor in high dimensional spaces? Proc. 26th Int. Conf. Very Large Data Bases, VLDB'00 506–515.

Hoxhaj, G., and Manning, B.D. (2020). The PI3K–AKT network at the interface of oncogenic signalling and cancer metabolism. Nat. Rev. Cancer *20*, 74–88.

Hu, H., Juvekar, A., Lyssiotis, C.A., Lien, E.C., Albeck, J.G., Oh, D., Varma, G., Hung, Y.P., Ullas, S., Lauring, J., et al. (2016). Phosphoinositide 3-Kinase Regulates Glycolysis through Mobilization of Aldolase from the Actin Cytoskeleton. Cell *164*, 433–446.

Hung, Y.P., Teragawa, C., Kosaisawe, N., Gillies, T.E., Pargett, M., Minguet, M., Distor, K., Rocha-Gregg, B.L., Coloff, J.L., Keibler, M.A., et al. (2017). Akt regulation of glycolysis mediates bioenergetic stability in epithelial cells. Elife *6*.

Jacques, M., Dobrzyński, M., Gagliardi, P.A., Sznitman, R., and Pertz, O. (2021). CODEX, a neural network approach to explore signaling dynamics landscapes. Mol. Syst. Biol. *17*, 1–14.

Janes, K.A., Wang, C.-C., Holmberg, K.J., Cabral, K., and Brugge, J.S. (2010). Identifying single-cell molecular programs by stochasticprofiling. Nat. Methods *7*, 311–317.

Jaqaman, K., Loerke, D., Mettlen, M., Kuwata, H., Grinstein, S., Schmid, S.L., and Danuser, G. (2008). Robust single-particle tracking in live-cell time-lapse sequences. Nat. Methods *5*, 695–702.

Kholodenko, B.N. (2006). Cell-signalling dynamics in time and space. Nat. Rev. Mol. Cell Biol. *7*, 165–176.

Kosaisawe, N., Sparta, B., Pargett, M., Teragawa, C.K., and Albeck, J.G. (2021). Transient phases of OXPHOS inhibitor resistance reveal underlying metabolic heterogeneity in single cells. Cell Metab. *33*, 649-665.e8.

Liu, G.Y., and Sabatini, D.M. (2020). mTOR at the nexus of nutrition, growth, ageing and disease. Nat. Rev. Mol. Cell Biol. *21*, 183–203.

Manning, B.D., and Toker, A. (2017). AKT/PKB Signaling: Navigating the Network. Cell *169*, 381–405.

Maryu, G., Matsuda, M., and Aoki, K. (2016). Multiplexed Fluorescence Imaging of ERK and Akt Activities and Cell-cycle Progression. Cell Struct. Funct. *41*, 81–92.

Mason, E.F., and Rathmell, J.C. (2011). Cell metabolism: an essential link between cell growth and apoptosis. Biochim. Biophys. Acta *1813*, 645–654.

McInnes, L., Healy, J., and Melville, J. (2018). UMAP: Uniform Manifold Approximation and Projection for Dimension Reduction.

Pargett, M., Gillies, T.E., Teragawa, C.K., Sparta, B., and Albeck, J.G. (2017). Single-Cell Imaging of ERK Signaling Using Fluorescent Biosensors. (Humana Press, New York, NY), pp. 35–59.

Peeters, K., Van Leemputte, F., Fischer, B., Bonini, B.M., Quezada, H., Tsytlonok, M., Haesen, D., Vanthienen, W., Bernardes, N., Gonzalez-Blas, C.B., et al. (2017). Fructose-1,6-bisphosphate couples glycolytic flux to activation of Ras. Nat. Commun. *8*.

Rebsamen, M., Pochini, L., Stasyk, T., De Araújo, M.E.G., Galluccio, M., Kandasamy, R.K., Snijder, B., Fauster, A., Rudashevskaya, E.L., Bruckner, M., et al. (2015). SLC38A9 is a component of the lysosomal amino acid sensing machinery that controls mTORC1. Nature *519*, 477–481.

Regot, S., Hughey, J.J., Bajar, B.T., Carrasco, S., and Covert, M.W. (2014). High-sensitivity measurements of multiple kinase activities in live single cells. Cell *157*, 1724–1734.

Roberts, D.J., Tan-Sah, V.P., Ding, E.Y., Smith, J.M., and Miyamoto, S. (2014). Hexokinase-II Positively Regulates Glucose Starvation-Induced Autophagy through TORC1 Inhibition. Mol. Cell

53, 521–533.

Ryu, H., Chung, M., Dobrzyński, M., Fey, D., Blum, Y., Sik Lee, S., Peter Matthiasand Kholodenko, B.N., Li Jeon, N., and Pertz, O. (2016). Frequency modulation of ERK activation dynamics rewires cellfate. Mol. Syst. Biol. *12*, 866.

Sampattavanich, S., Steiert, B., Kramer, B.A., Gyori, B.M., Albeck, J.G., and Sorger, P.K. (2018). Encoding Growth Factor Identity in the Temporal Dynamics of FOXO3 under the Combinatorial Control of ERK and AKT Kinases. Cell Syst. *6*, 664-678.e9.

Saxton, R.A., Chantranupong, L., Knockenhauer, K.E., Schwartz, T.U., and Sabatini, D.M. (2016). Mechanism of arginine sensing by CASTOR1 upstream of mTORC1. Nature *536*, 229–233.

Shen, C.-H., Yuan, P., Perez-Lorenzo, R., Zhang, Y., Lee, S.X., Ou, Y., Asara John Mand Cantley, L.C., and Zheng, B. (2013). Phosphorylation of BRAF by AMPK Impairs BRAF-KSR1Association and Cell Proliferation. Mol. Cell *52*, 161–172.

Stacey, R.G., Skinnider, M.A., and Foster, L.J. (2020). On the Robustness of Graph-Based Clustering to Random Network Alterations. Mol. Cell. Proteomics *20*, 100002.

Strasen, J., Sarma, U., Jentsch, M., Bohn, S., Sheng, C., Horbelt, D., Knaus, P., Legewie, S., and Loewer, A. (2018). Cell-specific responses to the cytokine TGFβ aredetermined by variability in protein levels. Mol. Syst. Biol. *14*, e7733.

Tanner, L.B., Goglia, A.G., Wei, M.H., Sehgal, T., Parsons, L.R., Park, J.O., White, E., Toettcher, J.E., and Rabinowitz, J.D. (2018). Four Key Steps Control Glycolytic Flux in Mammalian Cells. Cell Syst *7*, 49-62.e8.

Wolfson, R.L., Chantranupong, L., Saxton, R.A., Shen, K., Scaria, S.M., Cantor, J.R., and Sabatini, D.M. (2015). Sestrin2 is a leucine sensor for the mTORC1 pathway. Science (80-.). *351*, 43–48.

Worster, D.T., Schmelzle, T., Solimini, N.L., Lightcap, E.S., Millard, B., Mills, G.B., Brugge, J.S., and Albeck, J.G. (2012). Akt and ERK control the proliferative response of mammary epithelial cells to the growth factors IGF-1 and EGF through the cell cycle inhibitor p57Kip2. Sci. Signal. *5*, ra19.

Xia, S., Xiong, Z., Luo, Y., WeiXu, and Zhang, G. (2015). Effectiveness of the Euclidean distance in high dimensional spaces. Optik (Stuttg). *126*, 5614–5619.

Yamanouchi, T., Ogata, N., Tagaya, T., Kawasaki, T., Sekino, N., Funato, H., Akaoka, I., and Miyashita, H. (1996). Clinical usefulness of serum 1,5-anhydroglucitol in monitoring glycaemic control. Lancet *347*, 1514–1518.

Ying, H., Kimmelman, A.C., Lyssiotis, C.A., Hua, S., Chu, G.C., Fletcher-Sananikone, E., Locasale, J.W., Son, J., Zhang, H., Coloff, J.L., et al. (2012). Oncogenic Kras Maintains Pancreatic Tumors through Regulation of Anabolic Glucose Metabolism. Cell *149*, 656–670.

Yusa, K., Zhou, L., Li, M.A., Bradley, A., and Craig, N.L. (2011). A hyperactive piggyBac transposase for mammalian applications. Proc. Natl. Acad. Sci. *108*, 1531–1536.

Zhu, J., and Thompson, C.B. (2019). Metabolic regulation of cell growth and proliferation. Nat. Rev. Mol. Cell Biol. *20*, 436–450.

Chapter 5

Conclusions and future work

5.1. Abstract

This dissertation addressed the presence of heterogeneous metabolic and signaling functions among individual cells in mammalian cell lines. This heterogeneity is driven by underlying variation in cellular processes, including cell cycle, protein synthesis rate, and glycolytic rate. For example, heterogeneity in OXPHOS function governs how cells respond to growth signaling cues. We also showed that metabolic stress, which we model with chemical inhibitors, plays a significant role in how cells respond to growth factors, such as EGF. The majority of this work utilized live-cell imaging techniques to probe dynamic intracellular signaling activities. We developed a new plasmid and a clustering technique to explore high-dimensional time series data. The following chapters contain a summary of the work done, conclusions, and future directions.

5.2. Summary of Works

Chapter 3 details a novel method to probe functional metabolism at a single cell level, using the fluorescent protein-based biosensor AMPKAR2. AMPK is a crucial responder to metabolic stress, specifically the elevation of ADP/AMP to ATP ratio, and thus AMPK acts as an internal ‘fuel guage’ of the cell (Hardie, 2014; Hardie et al., 2012). By measuring AMPK activity in live cells, we observe a primary parameter of cellular metabolism. We were particularly interested in OXPHOS activity at a single cell level because of its importance in physiology. Previous work in yeast showed that yeast metabolism alternates between glycolysis- and OXPHOS-dependent phases (Cai and Tu, 2012; Tu et al., 2005). Recently, OXPHOS has become a sought-after target for cancer therapy. Multiple OXPHOS inhibitors are early clinical trials, for example, IACS-010759 (Molina et al., 2018) and Gboxin (Shi et al., 2019), as candidates for cancer therapy. We thus

hypothesized that mammalian cells might vary in their OXPHOS activity, both among cell types and individual cells.

Our strategy to probe OXPHOS activity at the single-cell level was to directly perturb electron transport chain (ETC) function with chemical compounds and measure AMPK activity in real-time. Effectively, this approach queries whether OXPHOS is required for efficient ATP production in each cell. First, we found that in the MCF10A cell line, when Oligomycin inhibits the ETC, an ATPase inhibitor, there are two distinct subpopulations of cells. The first subpopulation is cells that show immediate AMPK activation, termed OXPHOS-dependent cells (OP-dep). The second group is cells in which AMPK is not responsive to ETC inhibition, termed OXPHOS independent cells (OP-ind). This phenomenon is found in multiple cell lines of both cancerous and non-cancerous origin. We also found that cells that survive under OXPHOS inhibition undergo cycles between OP-dep and OP-ind states every two hours for more than three days. Under OXPHOS-inhibited conditions, this metabolic cycle also dictates when growth signaling proteins, such as ERK and mTORC1, can become active. We further showed that these short-term cycles are part of a longer metabolic cycle that takes about 36 hours to switch between OXPHOS dependent and independent states. To identify the driving factors that dictate the state of OXPHOS dependency, we measured the cell division cycle, glycolytic activity, and protein translation at the single-cell level. We showed that in the OP-dep state, cells tend to be in the G1 phase of the cell division cycle, have lower glycolytic activity, and synthesize proteins at a higher rate. On the other hand, the OP-ind state is best characterized by cells in the G2/M phase of the cell division cycle, with higher glycolytic activity and a lower protein production rate.

Altogether, this work shows that mammalian cell metabolism is cyclical and heterogeneous within isogenic cell populations. Metabolic heterogeneity appears to be critical to the function of key cell growth pathways. Lastly, OXPHOS heterogeneity could influence the therapeutic efficacy of OXPHOS inhibitors in cancer therapy.

Chapter 4 expands on the idea of metabolic regulation of growth signaling pathways by directly measuring ERK, AKT, and AMPK function at a single cell level using fluorescent biosensors. In terms of technical advancement, we first created a novel sensor expression system that can deliver up to three reporters in one transfection. This technique minimizes the unwanted effects of multiple transfections. We then confirmed that each sensor (ERKTR, AMPKAR2 and AKT-TR) expressed by this method performs appropriately. We also developed an unsupervised clustering algorithm for multivariate time series data based on autoencoder and Louvain community detection algorithms. More importantly, we developed an 'objective' optimization function for the number of clusters in unsupervised clustering and further determined the quality of clustering results.

In terms of biological advancement, we probed how the ERK-AKT signaling network integrates metabolic information from AMPK in real-time. First, our results showed that direct AMPK inhibition of ERK pathway has at least two distinct modes of action, as identified by two classes of ERK response pattern under active AMPK, in which about 50% of cells in the population have an initial strong ERK response followed by slow decay of ERK activity over 12 hours. The other mode of action is characterized by a weak initial ERK response to EGF that lasts for about 1 hour, followed by complete inhibition. These findings reveal the limitations of purely topological conceptions of cell signaling, demonstrating that connections between signaling molecules do not uniquely specify a pathway's function. We further compared two distinct modes of AMPK activation, one by direct AMPK activation, the other through glycolytic inhibition with 2-DG. We found that 2-DG has only one mode of action on the ERK pathway and provides much more potent ERK inhibition, characterized by weak initial ERK response of EGF followed by complete inhibition. This result signifies that AMPK might not be the critical communicating hub between cell metabolism and cell signaling.

Our results further clarify the multifaceted impact of AKT on ERK activity. On the one hand, AKT can directly inhibit ERK activity by inhibitory phosphorylation of RAF (Manning and Toker, 2017). On the other hand, AKT can increase glycolytic activity, which results in suppressed AMPK function. These two functions of AKT contradict each other, and the functional outcome of this conflict can be resolved by simultaneous measurement of ERK, AKT, and AMPK at the single-cell level. First, we found that direct AKT activation does not diminish ERK activity; rather, it helps sustain ERK activity after the initial response. Secondly, AKT inhibition results in lower ERK baseline activity. Though AKT inhibition does not affect the initial ERK response to EGF, it results in a slow rise of ERK activity over 12 hours. This response pattern does not match with that of direct AMPK activation, which suggests that, in fact, AMPK might not play a direct role in the AKT-mediated ERK response. Altogether, this work provides a framework for systemic analysis of multivariate single-cell dynamic activity data. It also provides evidence for advancing the concept of signaling network function beyond simple topological “connection” maps, and toward its functional behaviors.

5.3. Conclusion

Our work emphasizes that cell metabolism is heterogeneous and highly dynamic in individual cells. Typically, cell metabolism studies rely on bulk measurement and ‘profiling’ of metabolic states. We provided a novel technique to measure ‘functional’ cellular metabolism, rather than metabolic ‘profiles,’ with single-cell level resolution. We identified two distinct metabolic states in mammalian cells, OXPHOS dependent and OXPHOS independent, that can only be observed through single-cell measurement. We also show that OXPHOS dependency states are cyclical and govern the function of growth signaling pathways, thus putting cell metabolism at the forefront of understanding cell signaling. This ‘functional’ metabolic heterogeneity is not regulated by any single gene but rather by an ensemble of cellular states, including cell division cycle, glycolytic activity, and protein synthesis activity at any particular time.

Finally, OXPHOS heterogeneity presents a possible route for cancer therapeutic resistance to OXPHOS inhibition strategy.

Cells must coordinate both growth signaling and intracellular metabolic status to maintain homeostasis between nutrient processing (catabolic) and biosynthetic (anabolic) activities. Characterizing how cell metabolism alters growth signaling is central to understanding this homeostasis. Simultaneous live-cell measurement of growth signals, ERK and AKT, and a metabolic signal, AMPK, is the key to observe these interactions in real-time. First, AMPK has at least two modes of interaction with ERK signals. (1) AMPK fully inhibit ERK activity over a long time up to 12 hours. (2) AMPK could also slowly inhibit ERK activity after initial ERK activation. Secondly, even though multiple metabolic stresses activate AMPK, these stresses do not necessarily inhibit ERK through an AMPK-dependent mode. Thus, pose a question of a cancer treatment strategy that depends on AMPK activity. Lastly, AKT inhibition results in ERK pathway downregulation and diminished response to EGF. However, this suppressed ERK activity is transient and can be compensated over 12 hours. Though we do not know the mechanism that AKT suppresses ERK, we know that it is AMPK-independent. Our study did not provide a mechanistic explanation for these observations, but it provides data to refine the topological map of cell signaling by confining the possibility space of signal interaction behavior.

5.4. Future Work

The future works proposed here are designed to probe further into the cellular metabolic heterogeneity and how cell metabolism information is integrated into cell growth signaling. In the first part, we aim to further identify other ‘types’ of cellular metabolic heterogeneity and factors that diminish or increase metabolic heterogeneity. We also want to explore the phenotypic effects of heterogeneous responses of OXPHOS inhibition, such as cell division. In the latter part, we wish to create a more comprehensive cell signaling mechanistic model that includes metabolic

state as a deterministic factor. We also want to explore the phenotypic result of different response classes to growth factors under the same metabolic stress.

5.4.1. Deeper dive into single-cell metabolic heterogeneity

In chapter 3, we provided the first evidence that cellular OXPHOS activity is heterogeneous. However, there remain both technical and biological challenges for single-cell metabolism studies.First, presently we measure cellular metabolic status by measuring AMPK activity. This implies that organisms of interest must possess intact AMPK activation machinery. Furthermore, data from the AMPKAR2 sensor could be challenging to interpret. AMPKAR2 is a kinase sensor that could cross-react with other kinases inside the cell, thus interfering with AMPKAR2 readout. One solution is to develop a more sensitive 'metabolites' sensor, specifically ADP or ATP sensor, which does not exist at the moment. Even though in chapter 3, we adopt Ateam1.03, an ATP sensor, and PercevalHR, an ADP/ATP ratio sensor, we could not calibrate and convert the FRET ratio of these sensors to an absolute unit of concentration or ratio, which poses the question of what these sensors are measuring precisely.

Another critical question that we could not explain is how AMPKAR2 could have quasi-periodic behavior upon OXPHOS inhibition. One possible explanation could be that cells can only maintain glycolytic flux cyclically , or for limited periods of time. To test this idea, we need to either (1) directly measure ATP production rate from glycolysis or (2) measure metabolites from the rate-limiting steps of glycolysis,such as fructose-1-6-bisphosphate (F16BP). In fact, there exists an F16BP FRET biosensor (Merrins et al., 2013). However, this sensor is an intermolecular FRET sensor that has a very slow off-rate of around 15-30 minutes, which means that it cannot measure a fast change in metabolite concentration. We will need to design a new F16BP sensor that can respond to concentration change within seconds to capture changes in glycolysis; one possibility is to change the design to intramolecular FRET.

We also want to find a connection between OXPHOS heterogeneity and cell phenotypes, such as resistance to chemotherapies, activation of inflammatory pathways, or cell death. This generally means that we need to first probe the cell OXPHOS status with ETC inhibitor, followed by inhibitor removal, and then measure the cell phenotype of interest after ETC inhibitor removal. However, all existing OXPHOS inhibitors irreversibly bind to ETC targets and cannot be washed out. We need to identify a new reversible ETC inhibitor so that we can further probe the biological effects and correlates of OXPHOS heterogeneity.

Lastly, we also do not know if OXPHOS heterogeneity exists outside of *in vitro* cell culture conditions. We could develop transgenic mice that express AMPKAR2 FRET biosensor and ask how AMPKAR2 responds to OXPHOS inhibition at the organismal level.

5.4.2. Building a new cell signaling model that includes cell metabolism as a player

In chapter 4, we provided systemic evidence that metabolic conditions could influence growth signal behavior. Though we identified multiple signaling patterns, we did not link the signaling behavior with cell phenotype. One could simply measure gene expression through single-cell transcriptome studies or immunofluorescence to determine the transcription effect of such signaling behavior. We also point out that current cell signaling topology could not explain the dynamical behavior of ERK, AKT, and AMPK together. One direction is to use our clustering result to build a mechanistic model that encompasses signaling patterns over time and thus refine the current signaling topology, which will result in a more accurate prediction of cellular response to signaling behavior. This study also opens the possibility to identify signal interactions as a key regulator of cell behavior instead of signaling pattern alone. All in all, accurate description of how cell signaling interacts is also critical to pharmacological interventions of human disease.

5.5. References

Cai, L., and Tu, B.P. (2012). Driving the cell cycle through metabolism. Annu. Rev. Cell Dev. Biol. *28*, 59–87.

Hardie, D.G. (2014). AMP-activated protein kinase: A key regulator of energy balance with many roles in human disease. J. Intern. Med. *276*, 543–559.

Hardie, D.G., Ross, F. a, and Hawley, S. a (2012). AMPK: a nutrient and energy sensor that maintains energy homeostasis. Nat. Rev. Mol. Cell Biol. *13*, 251–262.

Manning, B.D., and Toker, A. (2017). AKT/PKB Signaling: Navigating the Network. Cell *169*, 381–405.

Merrins, M.J., Van Dyke, A.R., Mapp, A.K., Rizzo, M.A., and Satin, L.S. (2013). Direct measurements of oscillatory glycolysis in pancreatic islet ??-cells using novel fluorescence resonance energy transfer (FRET) biosensors for pyruvate kinase M2 activity. J. Biol. Chem. *288*, 33312–33322.

Molina, J.R., Sun, Y., Protopopova, M., Gera, S., Bandi, M., Bristow, C., McAfoos, T., Morlacchi, P., Ackroyd, J., Agip, A.-N.A., et al. (2018). An inhibitor of oxidative phosphorylation exploits cancer vulnerability. Nat. Med. *24*, 1036–1046.

Shi, Y., Lim, S.K., Liang, Q., Iyer, S. V, Wang, H.-Y., Wang, Z., Xie, X., Sun, D., Chen, Y.-J., Tabar, V., et al. (2019). Gboxin is an oxidative phosphorylation inhibitor that targets glioblastoma. Nature *567*, 341–346.

Tu, B.P., Kudlicki, A., Rowicka, M., and McKnight, S.L. (2005). Logic of the yeast metabolic cycle: temporal compartmentalization of cellular processes. Science *310*, 1152–1158.